IMPROVEMENTS ON AN ADHESIOMETER DESIGN THAT IMITATES HIGH STRESS/TEMPERATURE CONDITIONS TYPICAL OF MACHINING

IMPROVEMENTS ON AN ADHESIOMETER DESIGN THAT IMITATES HIGH STRESS/TEMPERATURE CONDITIONS TYPICAL OF MACHINING

By

MAXIMILIANO HERNAN MELLA MIRANDA, Mech. Eng

A Thesis Submitted to the School of Graduate Studies in Partial Fulfilment of the Requirements for the Degree Master of Applied Science

McMaster University, Hamilton, Ontario, Canada

MASTER OF APPLIED SCIENCE (2020) McMaster University

(MECHANICAL ENGINEERING) Hamilton, Ontario, Canada

TITLE:	IMPROVEMENTS ON AN ADHESIOMETER DESIGN THAT IMITATES HIGH STRESS/TEMPERATURE CONDITIONS TYPICAL OF MACHINING
AUTHOR:	Maximiliano Hernan Mella-Miranda. B. Eng., Mechanical Engineering
SUPERVISOR:	Dr. Stephen C. Veldhuis Department of Mechanical Engineering McMaster University
NUMBER OF PAGES:	xiv, 116

ABSTRACT

The objective of this work was to develop a new method for establishing the coefficient of friction for the machining conditions found on the rake face of a cutting tool. Critical aspects include the high pressures and high temperatures in the cutting zone. Using the base of an existing High-load High Temperature tribometer an adaptation referred to as a double-sided pin was implemented. The objectives were two-fold to improve the repeatability of the measurements and reduce the setup time by simplifying the alignment problems experienced on the previously used system.

The concept of the new setup is to press a double-end spherical pin made of the tool material between two flat surfaces made of workpiece material and rotating it using a string connected to a slider module. The normal load applied, the friction force needed to rotate the pin together with the temperature provided by a welder are then gathered and with the measurements of the imprints the coefficient of friction under specific loads can be established.

This work also studied the impact on the tests of pin radius and roughness of the pin surface in order to stablish the measurement limitations and conditions for a successful test.

Roughness of the pin had a significant impact on coefficient of friction results. Pins with roughness values around Ra = 0.5 demonstrated half the values of coefficient of friction than pins with Ra = 0.05. This was due the wear and the penetration of the pin into the workpiece sample material. The increase in pin dimensions facilitated testing on softer materials like AISI 1045. It was found to avoid seizure conditions but could not achieve pressures typical of machining difficult to cut materials like Ti-6Al-4V. The increase in pin size also helped in developing an understanding of how to measure the temperature at the contact zone between the pin and disk. Final testing showed a system repeatability of 8% was achieved with setup time reduced by approximately five times.

ACKNOWLEDGEMENTS

Firstly, I would like to express my sincere gratitude to my supervisor Dr. Stephen Veldhuis for the opportunity to work on such an innovative project as the MMRI Tribometer. His technical knowledge and way of dealing with diverse challenges in the institute is encouraging and inspirational for any young engineer working alongside him.

Secondly, I wish to declare my admiration for Dr. German Fox-Rabinovich, who with his incredible expertise guided me through this complex world of machining tribology and was always available to help me with my questions and provide advise; Dr. Jose Mario Paiva for helping me with anything I needed since my first steps in Canada in every aspect of work and life; Dr. Arif Abul for his mentoring and constant feedback of my research; for all the MMRI Staff that helped me with my machine training and for providing guidance through all my analysis.

I would like to thank to my wife Lys Carlinie Prestes for embracing the challenge of coming to another country to support me during my studies and for supporting me through this time. Also, to my parents who even miles away always seem to be present in my daily life.

Special thanks to all the friends I made in the last couple of years, that helped distract me and ensured I enjoyed every step of this journey.

I gratefully acknowledge that this research was supported by the Natural Sciences and Engineering Research Council of Canada (NSERC) under the CANRIMT Strategic Research Network Grant.

TABLE OF CONTENTS

LIST OF FIGURES

LIST OF TABLES

CHAPTER 1. INTRODUCTION

1.1. BACKGROUND AND MOTIVATION

During metal-cutting processes, a sharp tool made of a hard material, shears off a layer of a softer material to shape it into the desired geometry, dimensions and surface quality. The sheared off layer is referred to as a chip and is a waste product of this process. As it is removed it slides over the tool's rake face of the tool.

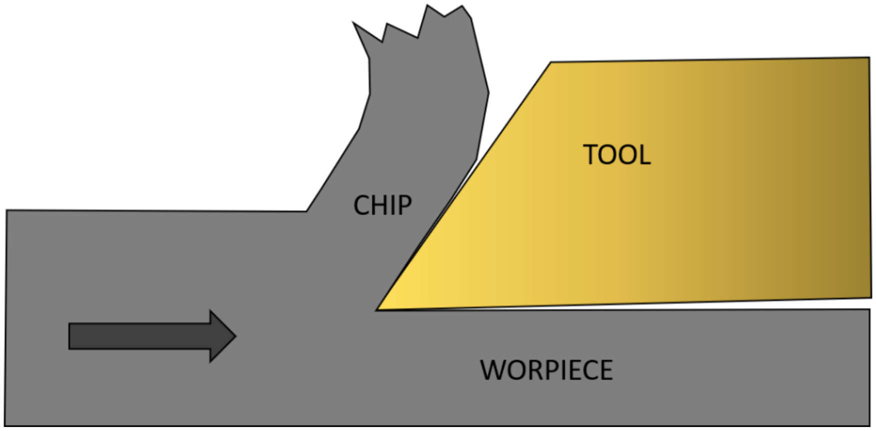

Figure 1: Workpiece and tool interaction in machining.

It is known that during this process, the surface of the tool operates under severe conditions of heavy load and high temperature. Shearing and sliding processes generate load on the surface and increase the temperature of the chip, which eventual cause the tool surface to wear. Growing market demand for manufactured goods places a high priority on improved productivity. The amount of metal removed by the tool over a period of time can serve as a measure of machining productivity. The material removal rate (MRR) relationship is given in Equation 1-1:

$$MRR = v\ f\ d \qquad \text{Equation 1-1}$$

v - cutting speed [mm/s],

f - feed [mm],

d- depth of cut [mm].

To increase this value, machining needs to be conducted at higher cutting speeds, which places severe stress on a cutting tool.

The focus of this research is to study the severe frictional conditions generated by the interaction between the surface of the tool and the workpiece in relation to the stress and temperature conditions. Developing a testing unit capable of both efficiently and accurately simulating and measuring machining variables presents a major challenge.

There are studies available in the literature which cover the design of instruments capable of simulating metal cutting conditions. The challenge is to isolate and measure the adhesion component of friction between the tool and the workpiece material under the high temperature and load associated with high performance machining. Understanding the mechanics of the tool/chip interaction may enable the implementation of a new test procedure which could reliably and efficiently measure the coefficient of friction instead of performing extensive machining process studies which consume expensive workpiece materials, tools and time.

Previous research [1]–[3] conducted over the last few years focused on the development of such devices and their practical implementation. Several tests were performed on their versions of the instrument which differed from the older studies carried out in the 80's [4]–[6]. The variation in the results obtained can be attributed to the different measurement methods, apparatus designs and procedures used to obtain the coefficient of friction data.

This research seeks to sort out these differences, understand the underlying physics behind them and evaluate the pros and cons of each method. The goal of this study is to develop a reliable new test method for simulating frictional conditions associated with high performance machining which is repeatable and easy to setup.

1.2. RESEARCH OBJECTIVES

1. Develop a new design for a double-sided pin adhesiometer.
2. Adapt the MMRI tribometer to meet the new setup requirements
3. Develop an experimental and calibration procedure for the new design.
4. Describe the the following design features in detail:
    - Doubled Side pin
    - Impact of Pin diameter
    - Effect of pin roughness on the coefficient of friction
    - Measurement conditions
    - Limitations of the tribometer
5. Conduct coefficient of friction (COF) studies on a coated sample using the newly generated adhesiometer.

CHAPTER 2. LITERATURE REVIEW

Machining involves many complex phenomena including heat transfer, material science and thermodynamics. Optimization of this process cannot be achieved by just considering one parameter. During metal cutting, the interaction between the workpiece material and the tool is conducted under extreme tribological conditions associated with high temperatures and loads. This leads to the development of adhesion, diffusion, oxidation, phase transformation and several other physical and chemical phenomena. These processes have a significant effect on cutting optimization as well as tool life, workpiece dimensional accuracy and surface integrity.

Friction during machining contributes to the heat production during the cutting process and strongly influences the deformation of surface layers of the workpiece. In many cases adhesion is the dominant frictional phenomenon during cutting, due to the high temperatures involved, the reactive newly opened surfaces and the plastic deformation of the workpiece.

Considering the importance of adhesion in metal cutting this thesis introduces an experimental setup capable of duplicating realistic conditions between the tool and the workpiece/chip in the cutting zone. This is done to selectively predict certain process characteristics common in metalworking. A custom setup is required as the tribo-system that forms as a result of tool/workpiece material interaction has unique characteristics that are hard to duplicate on their own outside of a full machining process.

Qualitative information can be gathered by collecting information on the separate properties of the materials in contact, but it is impossible to gain quantitative data specific to the underlying COF under various contact conditions in a controlled manner during machining.

The workpiece material and the tool interact under severe frictional conditions caused by high normal loads, temperatures, presence of vacuum and freshly generated surfaces. Under these conditions, the interatomic and intermolecular interactions play a decisive role in the progression of wear.

According to Kragelsky [7], it is impossible to calculate the value of the shear strength of adhesive bonds using just theoretical analysis when considering all of the factors involved in this process. Thus, experimental methods such as the one outlined in this thesis are required.

Qualitatively determining the tangential forces during machining is practically impossible for several reasons. One of these is that the variation in the normal load along the entire length of the tool, makes it difficult to selectively evaluate the direct correlation between the normal force and the shear force at all points along the tool. Another reason is the uneven distribution of temperatures across the chip/tool interaction area. Therefore, taking a direct measurement of the forces and temperatures during machining yields an average value, which does not take into account the different values of each individual contact point.

An important aspect of the sliding materials in contact, is that the tangential forces are not only dependent on the shear strength of the adhesive bonds, but also on the deformation component of friction, which will be further explained below.

In general, all flat surface features have some roughness at the microscopic scale consisting of peaks and valleys, which are known as asperities. When asperities are pressed against each other, peaks of the softer material interlock with the valleys of the harder material. This causes the relative tangential sliding of the surfaces to deform the underlying material and form a hemispherical roller in front, which then becomes sheared off. The dimensions of the roller depend on the relative penetration of the asperities' height over radius ratio and also on the shear strength of the adhesive bonds engaged at the interface [5], [7].

The deformation component within the tool and the chip can not be ignored under typical machining conditions due to the surface roughness of either of the materials. Moreover, both surfaces are not the same from the material science point of view. The polycrystalline structure of both components have heterogeneous mechanical properties that have an effect on sliding deformation.

In summary, various factors of the machining process impede direct measurement of forces, making it almost impossible to obtain an isolated reading of the tangential forces that arise from the deformation of asperities. The goal of this work is to develop test conditions under which the adhesion component of friction can be selectively evaluated. Data obtained in this way may be then used for the comparison and development of novel, friction reducing coatings. This would in turn, improve the quality of the machined parts, thereby enhancing the overall productivity of the machining process.

2.1. FRICTION

This chapter will provide an overview of the tribological processes developing on the rake surface of the tool. A brief historical outline of the models used to quantify friction will also be presented to highlight the importance of the adhesion component in highly loaded tribo-systems.

2.1.1. Historical Overview

The first systematic studies of friction date back to the 15th century and the works of Leonardo da Vinci (1452-1519). His sketches and notes feature the earliest known descriptions of the field of study that would eventually become known as tribology. From his findings, Leonardo made the following conclusions [8]: friction is proportional to the weight of the sample, it does not depend on the contact area between the surfaces and finally, the ratio of friction to weight is 1/4.

Two centuries later, Guillaume Amontons (1663-1705) re-discovered the rules of friction since Leonardo da Vinci's notes on the subject were at that time lost to the public. Amontons introduced a general description of friction summarized in 4 laws: 1) Friction is proportional to pressure. 2) It remains constant for every material combination once it is lubricated. 3) The ratio of friction to pressure is 1:3. 4) Friction does not depend on velocity and other conditions. The frictional laws of Amontons were general statements intended to aid engineers who faced practical challenges but were insufficient for describing the sophisticated friction phenomena in detail.

Decades later, an extensive experimental study conducted by Charles Augustin Coulomb (1736-1806) analyzed the influence of different sliding parameters (normal force, sliding velocity, area of contact, atmosphere) and in agreement with Amontons’s law, conclusively demonstrated that friction was independent of the sliding velocity.

In addition to the above, Coulomb was also the first to record the influence of surface asperities on the increase of friction. A set of studies by J. T. Desaguliers [7] contradicted the model proposed by Coulomb, experimentally showing that highly polished surfaces have a strong atomic bond when in contact, which results in increased friction. He thus discovered an early concept of adhesion, in which the atomic structures of two material surfaces exercise an attraction force when in close proximity to each other.

Only in the middle of the 20th century had Bowden and Tabor [9] proposed what is considered to be the basis of modern friction theory. It was established in their study that the nature of the contact between solid bodies is determined by the interaction of small asperities present in all surfaces. Asperities are defined as the roughness peaks on the surface of a specimen. Even the flattest surfaces feature an embedded roughness when assessed at the micro/nano scale, as is shown in the picture below (Figure 2).

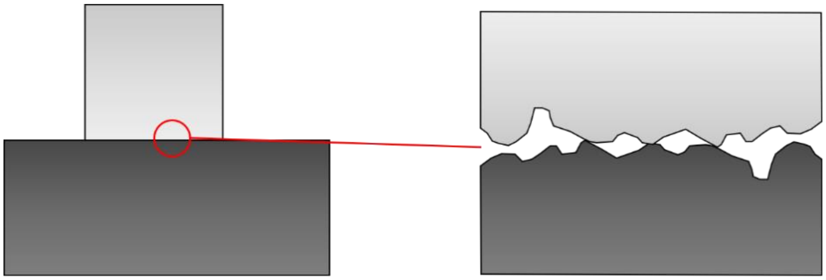

Figure 2: The roughness representation of an apparent smooth surface at the micro/nano scale

As suggested in the previous paragraph, these small asperities embedded in every surface play a huge role in the friction wear process and thereby present an important subject of geometric inquiry.

The surface roughness is characterized by the measurement of the deviations in the perpendicular direction from an ideal surface. In practical terms, if the magnitude of these deviation measurements determines the roughness or smoothness of a surface. The most common parameter for measuring surface roughness is Ra (Figure 3) which is defined as the average of the absolute height values of the deviations from an average profile, given by the Equation 2-1:

$$R_a = \frac{1}{l}\int_{x=0}^{x=1} |h|\, dx \qquad \text{Equation 2-1}$$

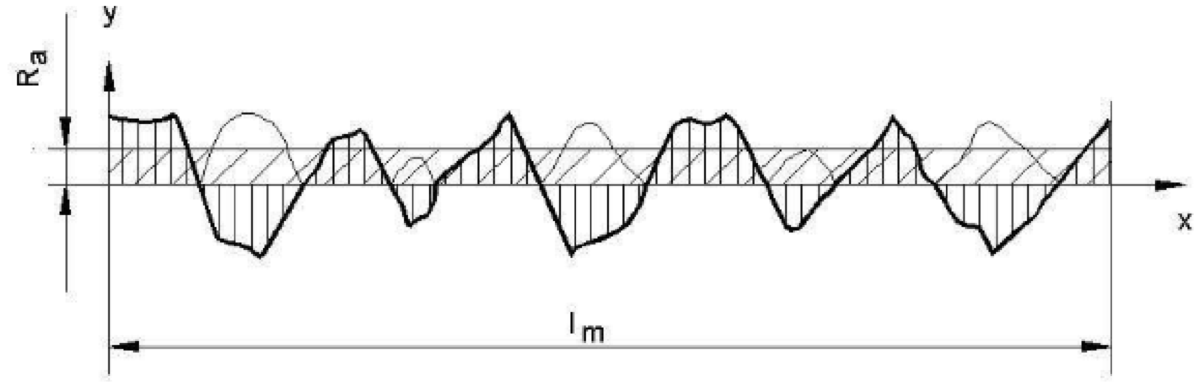

Figure 3: Surface Ra Roughness calculation.

There exist other methods for quantifying surface roughness, such as Rq and Rz. However, it is hard to completely characterize a surface by just one parameter. Even surfaces with the same roughness value can feature completely different geometric aspects. These aspects can be assessed only if specific information about the material surface can be obtained using more specialized types of measuring techniques, such as 3D images from an interferometer as well as alternative types of R surface measurements.

Since all surfaces have at least some degree of roughness, the asperities of the two surfaces in contact create junctions, as shown in Figure 4 a). In other words, the small portion of the "apparent" area (A_P) that is actually in contact, is known as the "Real" area of contact (A_R).

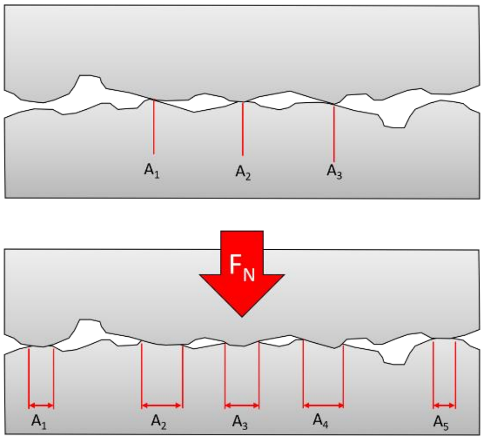

Figure 4: Increase of Real Area of contact due Normal Force

Interactions taking place between the asperities of two surfaces in contact are known as junctions. As load is applied to the surface, elastic deformation occurs within the junctions. In turn, plastic deformation increases the number of junctions as can be seen in Figure 4b), thereby also causing the Real area of contact (A_R) to grow according to Equation 2-2

$$A_R = \sum_{n=1}^{n=j} An$$ Equation 2-2

Where n is the junction number and j the total number of junctions. The number of junctions tends to increase up until the limit at which the real area of contact can withstand the normal load applied.

Rabinovich [5] describes the relationship between the Brinell hardness of a material with the normal load applied to the real area of contact in Equation 2-3. Although this inequality is valid for surfaces with a high grade polish, in most cases where the surfaces have considerable roughness, the relationship is in fact an equality. [10]

$$A_r \geq \frac{F_N}{HB}$$ Equation 2-3

A consequence of the above statement, is that the ratio between the real area of contact and the apparent area must be between 0 and 1 for all contacts, as given in Equation 2-4.

$$0 < \frac{A_r}{A_A} \leq 1 \qquad \text{Equation 2-4}$$

This ratio is small for lightly loaded contacts. As more load is applied to the system the real area tends to equal the apparent area. The material deforms as more asperities become sheared off under the load, increasing the number of contacts up to the point at which the surface becomes more or less flat. When the ratio equals one, Bowden, Tabor and Shaw [11] described the behavior of the resulting compressive stresses in terms of what they called Heavy Loaded Sliders (HLS) in contrast to Lightly Loaded Sliders (LLS). Assuming that just one spherical asperity comes into contact under a light load, the compressive stress will eventually reach a uniform value on the interface as more load is applied to the system. This value would be three times the yield strength of the softer material and equal to the yield stress just below the surface. Figure 5 can help understand the stress distribution within an asperity under load [11], [12].

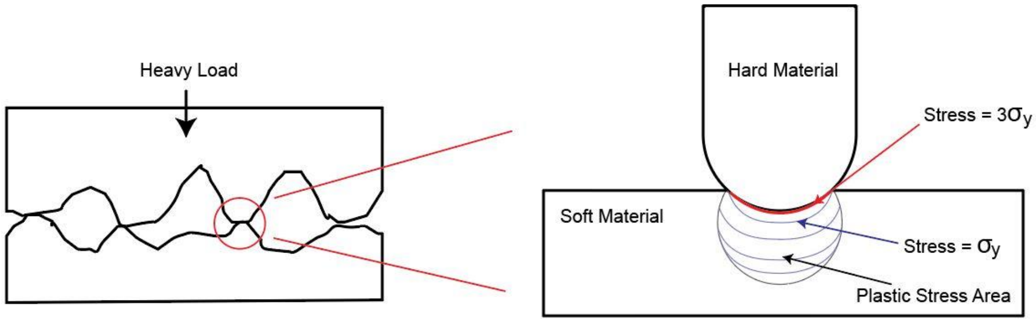

Figure 5: Stresses distribution in an indenter.

Based on the results of Bowden and Tabor [13], stress on the interface does not surpass the value of three times the yield strength of the material. Combining equations Equation 2-3 and Equation 2-4, it is possible to obtain the minimum real area of contact in Equation 2-5:

$$A_{R,min} = \frac{F_N}{HB} = \frac{F_N}{3\sigma_Y} \qquad \text{Equation 2-5}$$

Where $A_{R,min}$ is the minimum real area of contact; F_N is the normal load and σ_Y is the yield strength of the softer material.

Rearranging the above expressions yields Equation 2-6:

$$\frac{A_R}{A_A} = \frac{\sigma_Y}{3\sigma_Y} = \frac{1}{3} \qquad \text{Equation 2-6}$$

The ratio in Equation 2-6, represents the threshold at which LLS becomes HLS in terms of the area of contact. If the ratio between these areas is less than one third of the contact area, the system is considered lightly loaded, if it is above 1/3, it will be considered highly loaded up to a maximum ratio of 1, at which point plastic deformation of the bulk material occurs. This relationship will remain constant even as the load is increased.

When the ratio between A_R and A_A equals 1, the two surfaces begin to feature strong adhesion. When no relative movement at the interface is possible, this creates a velocity gradient between the interface and the internal material, which causes shearing. This internal shearing of softer material during the sliding motion is known as *seizure*. It usually occurs on the first half of the contact tool/chip contact length under high loads and is characterized by strong adhesion of the chip to the tool surface. A more elaborate description of seizure will be presented in a later chapter of this work.

As mentioned previously, all the friction phenomena occur at locations on the real area of contact. Friction depends on the effective contact area of the interacting surfaces. It is worth noting that the real contact area is much smaller than the apparent contact area, especially under lower loads and in materials with a rough finish.

To gain a better understanding of the influence that the size of the real area has on friction, Shaw [14] constructed an apparatus to measure the torque needed to rotate a steel ball that was crushed in the plane surface of a softer material. Given the magnitude of the normal load, the torque necessary to rotate the ball and the resulting imprint, could be used to determine the values of shear and normal stresses. Depending on the applied load, three different frictional behaviors were observed, Figure 6.

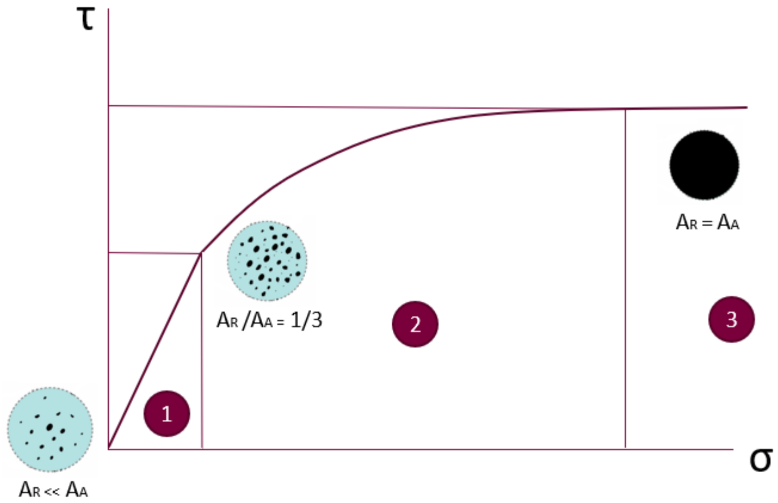

Figure 6: Relation between shear stress, normal stress and real area of contact.

In the first region, the amount of torque needed to rotate the ball linearly increased along with the load, resulting in a constant coefficient of friction in that region. a comparison can be made with the ratio of the real area to the apparent area, since in this region, the real area is much smaller than the apparent area due to low loads. In this first region, once the real area exceeds 1/3 of the apparent area, plastic deformation no longer flattens the asperities. The subsurface begins to plastically deform and shear, reducing the rate at which the real area expands in the second region. As a result, the coefficient of friction fluctuates (region 3) until the real area A_R is equal to the apparent area A_A and the shear stress stabilizes, which corresponds to the strength of the softer material. This confirms that subsurface plastic flow is dominant during sliding.

To summarize, the coefficient of friction is constant in region 1, and the ratio Ar/Aa is no more than 1/3. In region 3, A_R/A_A is equal to 1, with some bulk shearing of the softer material. Region 2 represents a transition between these two states, where bulk shearing of the soft material occurs along with sliding. As stated by Shaw [11], the state of this region provides a good indication of the overall progress of friction during machining, especially with regards to adhesion.

The dominant model currently used to characterize friction is the Merchant Molecular-Mechanical theory of friction [11]. This model regards the interlocking of asperities in conjunction with adhesion caused by the molecular interaction of the surface materials in contact.

2.1.2. Shear and External Friction

There is a difference between external friction and shear. Surface friction occurs within the contact zones of the two different bodies being rubbed against each other. Considering the amount of shear strength required to move the bodies, the determining factors of this process are the normal load applied between the samples, the mechanical properties and the surface roughness of the materials involved. In the case of shear, the shear strength acting against the moving bodies is derived from the surface characteristics of the bulk material undergoing deformation.

The main difference between external friction and shear is the source of shear strength. The former arises from the bonds between the surfaces and the latter is derived from the shear strength of the softer material [7].

The main subject of interest in this work is the character of external friction between solid bodies. To ensure that external friction occurs only in a heavily loaded system, a significant part of the tests needs to be carried out in order to maintain a weakened layer on the interface between the bodies in contact, up to the limit of the bulk material's shear strength. Several methods of weakening the surface layers in relation to the solid materials are commonly used today, such as liquid lubricants which create a gap between sliding materials, solid lubricants and multifunctional coatings [5].

Lubricants function through the adsorption of polar molecules of the lubricating compound by the metal undergoing treatment, causing it to form molecular piles. At high operating temperatures, other means of lubrication are needed, such as those employing chemical or tribochemical interactions with the material surfaces to form a low shear resistance layer in between [15].

Some authors [5], [7], [15], [16] have established a gradient rule for shear strength to address the problem of bulk deformation of the softer material. This gradient rule is based on two dimensionless characteristics of the asperities in contact. The first is the height to radius ratio of the imprints in the softer material and the second is the ratio between the shear and compressive stresses. This rule is expressed in Equation 2-7:

$$\gamma = \frac{h}{r} + \frac{\tau}{\sigma} < 0.5$$

Equation 2-7

This equation was derived from an experiment described in [7]. In this experiment, a spherical indenter representing a single asperity was put under a high load and dragged over a softer material, until a buildup of material was observed in front of the indenter. It was assumed that the material sublayer was being deformed and bulk plastic deformation was occurring. The value of 0.5 represents the threshold at which this phenomenon was observed.

2.2. MACHINING

Metal cutting or machining is a mechanical process in which a hard tool removes layers of workpiece material to produce a final part with the desired shape and dimensions. During this process, a sharp tool made from a hard material engages with a workpiece by shearing and removing small layers of its material in the form of chips.

Chip formation occurs in a region known as the primary deformation zone, which extends between the tip of the tool and the junction between the surfaces of the chip and the workpiece. Therefore, it is a considerably work hardened layer of metal that flows over the rake face of the tool. The rake face then undergoes substantial normal and frictional stresses due to the chip flow, which by itself constitutes another zone of deformation known as the secondary deformation zone, Figure 7 [17].

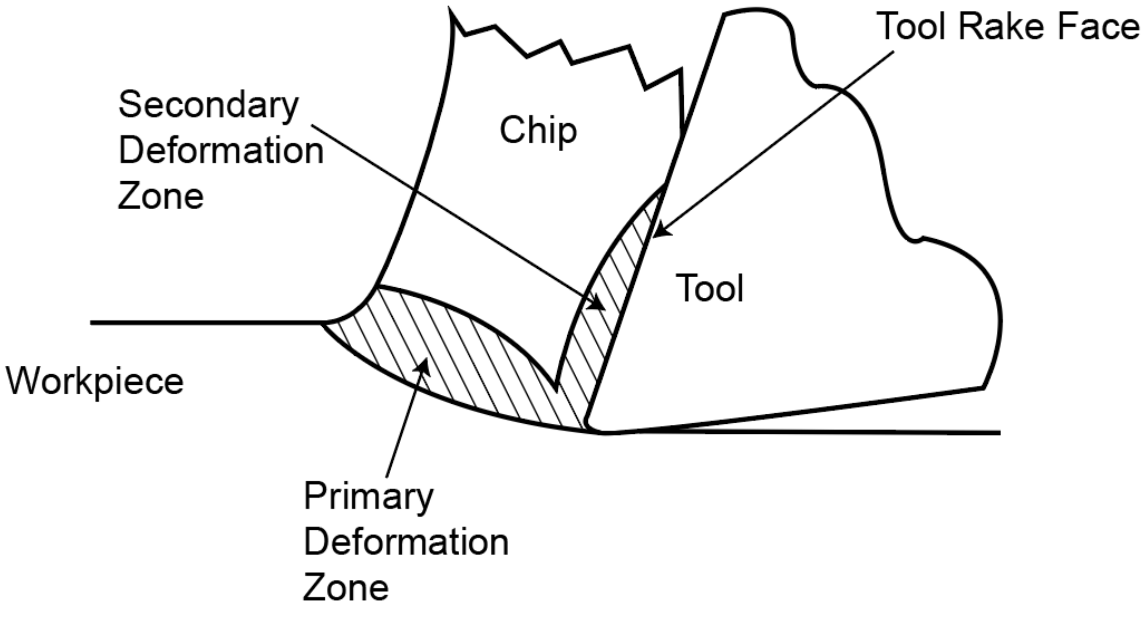

Figure 7: Deformation zones in metal cutting.

2.2.1. Machining Forces

The importance of cutting force measurements during the machining process was first brought up by Merchant in 1945 [11]. The presented model considers an orthogonal cutting model where a wedge-shaped tool is positioned perpendicular to the workpiece. The chip forms along the shear plane and is oriented at an angle φ in relation to the surface of the workpiece. This model is depicted in the Figure 8. It can be used to calculate forces in conjunction with the force measurements taken by a dynamometer [11].

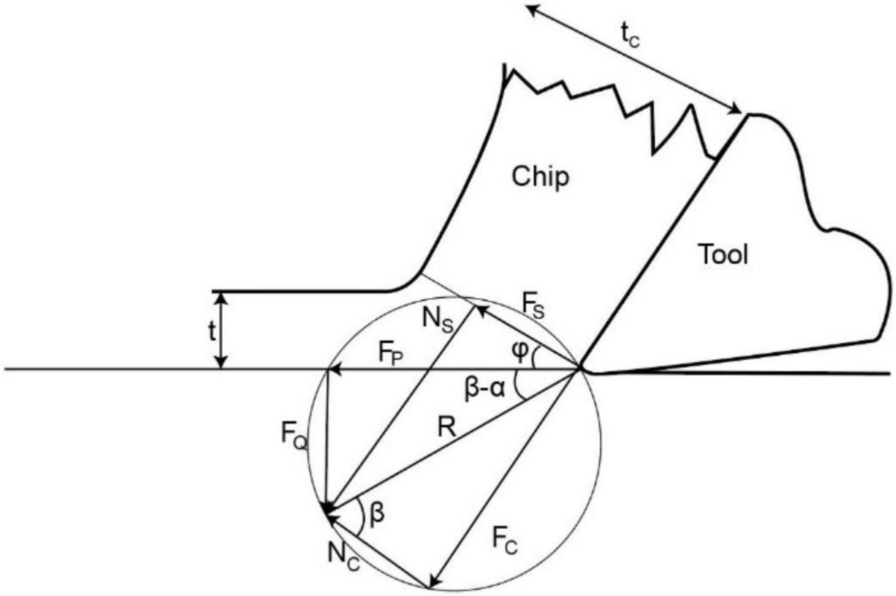

Figure 8: Merchant model of forces in machining [11].

The composition of the forces were assessed (Figure 9) in the following way: the force components acting in the shear plane of the workpiece material (F_s and N_S), the force components measured by the dynamometer (F_P and F_Q), and the resultant force R’. In the right diagram of Figure 9, the forces F_C and N_C are tangential and normal to the rake face of the tool respectively and R is the resultant force.

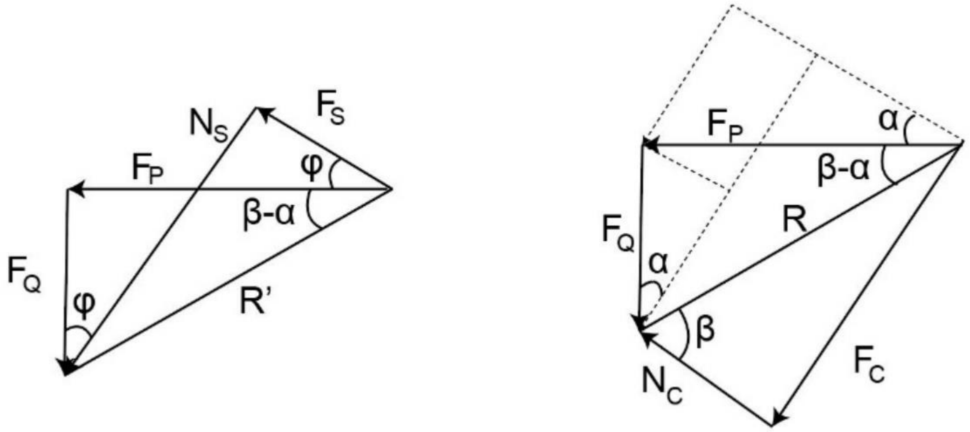

Figure 9: Diagram of forces in machining.

Where:

- φ is the shear angle
- α is rake face angle
- β is the friction angle.
- F_P and F_Q are the cutting forces measured experimentally on the tool.
- F_s and N_S are the tangential and normal forces located within the shear plane
- F_C and N_C are the forces tangential and normal to the chip
- R and R’ are the resultant forces

Based on the previous considerations, the shearing forces can be described in terms of the following expressions derived from Figure 9:

$$F_S = F_P \cos\varphi - F_Q \sin\varphi \qquad \text{Equation 2-8}$$

$$N_S = F_Q \cos\varphi - F_P \sin\varphi = F_S \tan(\varphi + \beta - \alpha) \qquad \text{Equation 2-9}$$

The forces acting on the rake face of the tool can be evaluated as follows:

$$F_C = F_C \sin\alpha + F_Q \cos\alpha \qquad \text{Equation 2-10}$$

$$N_C = F_P \sin\varphi - F_Q \cos\varphi \qquad \text{Equation 2-11}$$

The coefficient of friction can be obtained from the ratio of tangential and normal forces acting on the rake face of the tool:

$$\mu = \tan\beta = \frac{F_C}{N_C} = \frac{F_P \sin\alpha + F_Q \cos\alpha}{F_P \cos\alpha + F_Q \sin\alpha} \qquad \text{Equation 2-12}$$

Assuming mass and chip volume remain constant, the cutting process and the density of the material do not affect the equations.

$$tbl = t_c b_c l_c \qquad \text{Equation 2-13}$$

Where t is the uncut chip thickness; b is the cutting width and l length of the cut, and c refers to the dimensions of the cut and uncut chips. Rearranging the terms of this expression gives the chip thickness ratio r.

$$\frac{t}{t_c} = \frac{l_c}{l} = r \qquad \text{Equation 2-14}$$

The shear angle can then be calculated from the chip using the chip thickness ratio (r) and the rake angle α:

$$\tan\varphi = \frac{r\cos\alpha}{1 - r\sin\alpha}$$ Equation 2-15

Another useful parameter is chip velocity, described in Equation 2-16, where V_C is the chip velocity, V is the cutting velocity and r is the chip thickness ratio:

$$V_C = rV$$ Equation 2-17

2.2.2. Machining Stresses and Friction

Machining stresses tend to be high due the high loads and the relatively small area of the tool/chip contact surface on the rake face of the tool, which directly impacts tool life. Zorev, as described in [18], proposed a model that outlines the normal and shear stresses on the tool by dividing the tool into two regions according to the chip behavior: the sticking zone and the sliding zone.

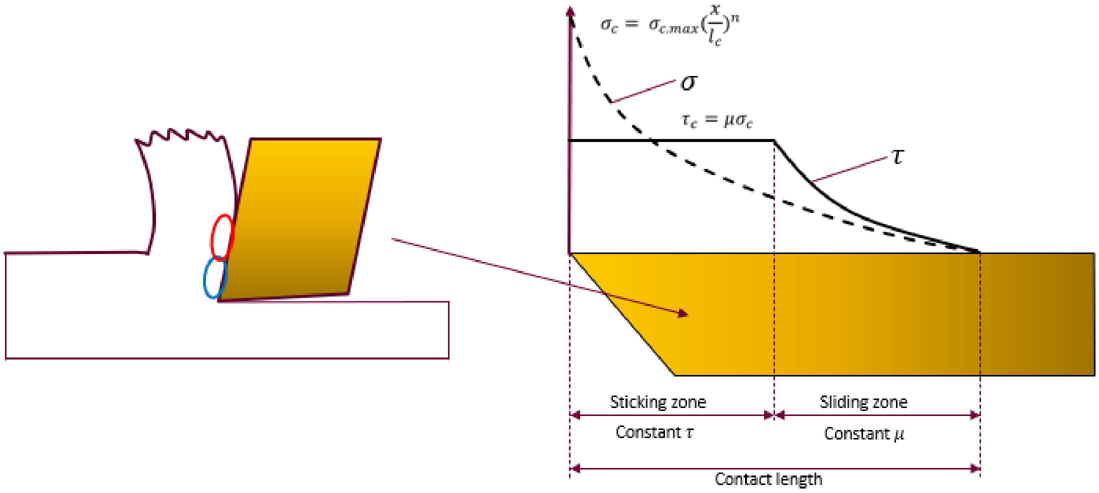

Figure 10: Left) sticking and sliding zone; Right) stresses in the rake face of the tool.

Figure 10 shows that stresses are highest at the tool tip, decrease along its length until the detachment of the chip from the rake face. The normal stresses along the tool length adhere to

Equation 2-18 where x is the distance from the tool tip, Lc is the chip contact length and n is an exponential parameter [18].

$$\sigma_C = \sigma_{C,max}(\frac{x}{l_C})^n \qquad \text{Equation 2-18}$$

The shear stress along the tool length is different in each of the two zones. In the first zone, known as the sticking zone, the chip has completely adhered to the surface of the tool. The bulk of the chip material shears off, creating a constant and maximum shear stress in this region. This corresponds to the shear stress resistance of the material being cut, as can be seen in Figure 10. Such sticking is mainly caused by high temperatures and normal loads within the first region of the tool. It was previously mentioned in this work as a seizure phenomenon.

Half of the contact length lies in the seizure zone and the other half lies in the sliding zone. [19][18]

Seizure occurs on the rake face of the tool in several stages. The first stage is the plastic deformation of asperities that breaks away the oxides or other films on the surface. The second stage is the nucleation of asperities from both materials in contact. At the same time, plastic deformation still continues, intensified by material flow. Finally, in the third stage, the asperities interlock to form strong intermolecular bonds, which are caused by the seizure on the surface. These points of plastic deformation on which interlocking and seizure occurs, are being repeatedly formed and broken during metal cutting [5].

In the second sliding zone, the normal load is below a certain limit sufficient to shear the chip from the bulk, which enables the chip material to slide over the rake face of the tool. In Zorev's model [11] the shear stresses present in this region follow the classical laws of friction given by the equation:

$$\tau_c = \mu \, \sigma_c \qquad \text{Equation 2-19}$$

Where, τ_c is the shear stress in the region, σ_c the normal stress, and μ the coefficient of friction.

2.2.3. Mechanism of Friction in Machining

It was demonstrated that adhesive bond strength provides the principal resistance to the motion of interacting bodies. Even though this accounts for more than 90% of the friction, the following additional factors need to be considered as well [5]:

Roughness due to asperities: The irregularities present on the surfaces of the interacting bodies both increase and decrease friction, depending on their relative motion. In general, the effect of surface roughness is largely minimal, contributing to no greater than 0.05% of overall friction in most cases.

Material removal: When a hard surface with sharp asperities slides over a softer one, the asperities tend to scratch the softer material. This can generate a certain amount of friction as noted by Halling and Rabinowicz [10] [20], but is mostly negligible, since in most cases, the asperities have a low inclination angle and the material removal rate can be comparable to that of adhesion.

Electrical component: When different materials come into contact, it is known that electrical charges are localized on the surfaces of the junctions. The separation of these junctions during motion generates an electrical charge which may increase the frictional force. The contribution of this to the overall friction is even lower than the previous two factors mentioned. Though these factors are considered in Equation 2-20, adhesion usually remains the dominant component of friction.

$$F_F = F_{adhesion} + F_{roughness} + F_{material\ removal} + F_{electrical} \qquad \text{Equation 2-20}$$

It should be mentioned that all the above statements are only valid for experiments performed under low loads.

2.2.4. Wear in Machining

The chief aim of machining is to perform a controlled metal cut that ensures high dimensional accuracy, surface quality and low residual stresses in the produced part.

However, the typical conditions associated with machining, such as high temperatures, high pressures and chemical interactions significantly contribute to tool wear. This leads to economic losses due to the constant changing of the tool, machining pauses, high energy consumption and poor quality of the machined parts. Therefore, the improvement of tool wear resistance provides a major economic goal for machining studies.

Although wear generally takes place in a combined form, there usually is a dominant aspect which limits the usage of parts. Due to the wide scope of this subject, this chapter will focus on the types of wear, specific for machining.

The most widespread tools used in machining are made from cemented carbides containing Tungsten Carbide (WC) held together with a Cobalt (Co) binder in proportions ranging from 3 to 12%. This has proven to be the material of choice in most machining applications (80 to 90%) due its hardness, toughness, chemical and thermal stability, and ability to be sintered into complex shapes cost effectively. But WC-Co itself is more appropriate for the machining of heat resistant super alloys (HRSA) or titanium alloys and the turning of hardened materials only at low speeds.

The carbide tools are usually coated with Chemical vapor deposition (CVD) or Physical Vapor Deposition (PVD) coatings that provide greater durability, depending on the workpiece material.

Types of tool wear

Plastic deformation:

Machining of hard materials under high operating temperatures can soften the tool material, especially its cutting edge and generate plastic deformation. The cutting edge typically has too low of a mass to withstand these intense stress/temperature conditions.

Diffusion wear:

Diffusion is the transfer of atoms due to a certain difference in the concentration of one material to another. The rate of this atomic transference is greatly increased at high temperatures due to atomic interdiffusion. This kind of wear is commonly observed at high speeds, temperatures and feeds, usually leading to crater formation on the rake of the tool. Crater wear often occurs during high speed machining due to the rubbing of newly formed chips along the rake surface within the sliding zone.

Adhesive wear

Adhesive wear is the most common form of wear experienced in engineering applications. As previously stated, adhesion happens due to strong bonds in the asperities between contacting materials that need to be broken to the continue the relative movement of the contacting bodies. The breakage of cold-welded asperities results in severe damage to the surface. This is especially a problem during the contact of similar materials, lack of proper lubrication, high temperatures and high slip velocity [10].

Bowden and Tabor [11] made experimental measurements of electrical conductivity. For most surfaces used in engineering, the Ar/Aa ratio varies from 10^{-2} to 10^{-5}. Even with small loads applied onto the contacts, these points of contact are small, causing the asperities to undergo total plastic deformation. The nature of the contact is more intense in material surfaces that are clean and free from oxides. Atomic attractions lead to the formation of strong adhesive bonds. If these surfaces are slipping relative to each other, the breakage of adhesive bonds occurs in either the original point of contact or in another location, depending on factors such as temperature distribution, work hardening, geometry, and stress distribution. If the interface attachments are broken in a different region from the original area of junction, transfer of small particles occurs within the surfaces, initiating the process of adhesion wear as is shown in Figure 11.

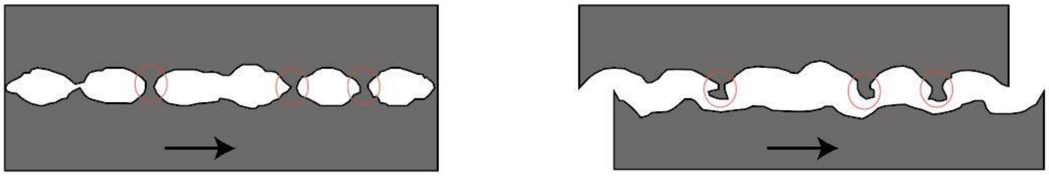

Figure 11: Left) Cold weld between asperities. Right) Adhesive wear.

The wear takes place in the following steps: First, as the surfaces are brought under load, the points of contact plastically deform, resulting in cold-welding between them. Then, a part of the interface breaks off without particle transfer, and finally, rupture of the interface occurs with particle transfer.

Further slipping can either dislocate a particle and release it to the interface or bind it to another surface. If the ensuing wear becomes severe with a significant volume of material transfer, this phenomenon is called *galling*. If galling continues when the interfaces are unable to move relative to each other, this is considered to be seizure.

Seizure usually occurs at low machining speeds. The formation of several layers of strain hardened workpiece material strongly adheres to the surface of the tool, forming a Build-up-edge (BUE). In this case the chip is not being formed from the cutting edge of the tool, but from a region of the strongly adhered material. In some cases, a BUE can actually aid in the preservation of the tool, although with likely dimensional errors in the parts.

The BUE is inherently unstable and can abruptly break away, causing severe roughness in the workpiece. In more severe cases, a strongly adherent BUE can break off a portion of the tool.

Abrasive wear:

This form of wear occurs when a rough and hard surface (or a soft surface with hard particles) slides over a softer surface, ploughing it. This wear usually leaves a scratch and carries away particles of the softer element.

The tool is usually harder than the workpiece material in most machining applications, but in some materials, hard inclusions such as sand particles from casting, carbide inclusions in steel and even BUE fragments can be present in the workpiece. In a hypothetical case scenario, if hard particles are spaced 100 microns apart from each other in the workpiece material, more than 60 million hard particles will be forced to slide over the cutting edge over the course of the usual tool life.

This leads to a *flank wear* where the wear volume is much higher than in adhesion wear.

Oxidation wear

This wear takes place in the peripheral regions of the tool/chip contact. Real area of contact in peripheral regions is much smaller than the apparent area due to the reduced normal contact stress. No seizure can take place there, only sliding or stick-slip behavior. It is easier for the surrounding atmosphere to enter into the contacts region near the free surface and cause chemical reactions within either surface, given the high temperature of machining.

This results in what is known as *depth-of-cut notch wear* which is localized at the region where there is no actual contact of the tool with the workpiece.

Previously, hardness of the cutting tool was believed to play the dominant role in tool-life improvement. Many efforts were made to develop high hardness tool coatings for improving tool life. However, this has proven to be not always the best approach. The literature shows that some coatings with hardness of around 25GPa have a better machining life, in some cases, than harder coatings that range at about 35GPa. It's clear that the complex mechanism of friction can not be brought under control solely by increasing the hardness of coatings [5]. Most of the commercially available coatings are based on Ti-N with a combination of other elements such as Al, Cr, C and several others, and are deposited by CVD or PVD.

Friction temperatures, especially in Heavy Loaded Tribosystems (HLTS) tend to be extremely high, which also affects the friction forces. A study conducted by Rabinovich [5] on AISI 1040 steel shows the influence of several WC tools on the friction force under several temperatures. The trends depicted in Figure 12 illustrate that the friction force can be considerably affected by the coatings at each temperature.

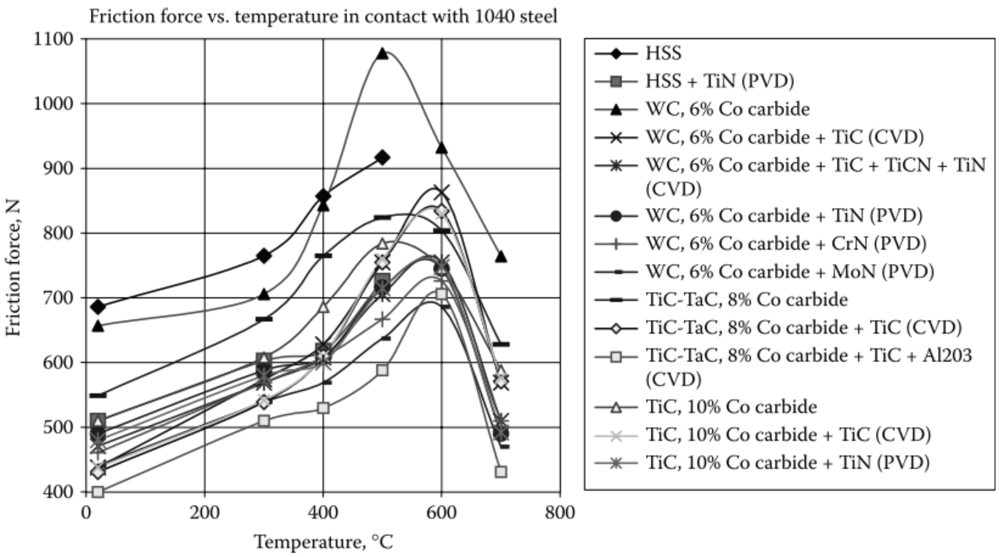

Figure 12: The friction forces of several coatings [5].

In general, the higher hardness of the coatings relative to the tool material did not describe the improvement in tool-life, but other properties were shown to be important such as a coating that provided temperature insulation due to its lower thermal conductivity compared to WC.

The main contribution of coatings are the thermal barrier/lubricious properties they can provide, which reduces the coefficient of friction and as a consequence, temperatures as well. These properties can be attributed to *tribofilm* production on the interface under high temperatures and loads, which provide better chemical stability and lubricity.

Tribofilms are a product of the chemical reactions on the tribological surfaces, that form as solid films during friction. They can reduce frictional forces and wear by supplying thermal protection and lubrication to the system [5], [21]. A practical example of this occurs during machining with a TiAlN coating that forms an aluminum oxide (Al_2O_3) tribofilm on the surface of the tool, which is a thermal protective component capable of reducing friction [5].

Machining temperature, as was already established, play a major role in tool wear. Heat generation during machining has been a subject of research since 1799, when Rumford as described in [11] studied the effect of water elevation on temperature during the manufacturing of a brass canon.

Ever since the first study by Taylor in 1907 [11] it has been known that when a metal goes into plastic deformation, almost all of the process's energy is converted into heat. The productivity of machining is directly associated with cutting temperature, which is proportional to the cutting speed. As a consequence, the temperature resistance of a tool's material is a major limiting factor of its performance. Researchers are constantly working to overcome this limitation.

Several techniques have been developed to measure temperature within the cutting zone, though accurate results are hard to obtain. According to Tay [22], drilling an indent in the chip or the tool to conceal a thermocouple to measure its temperature can by itself interfere with the final reading. To avoid this problem, analytical methods such as finite element modeling (FEM) have been used to indirectly assess the temperatures of machining.

During machining, heat is generated in the three zones depicted in Figure 13. The first zone is the Primary Shear deformation zone (PSDZ) due to the plastic deformation of the chip. Most of the heat is generated (almost 75%) in this location. The heat generated in this zone influences the flow stress of the workpiece material, chip formation and the cutting forces.

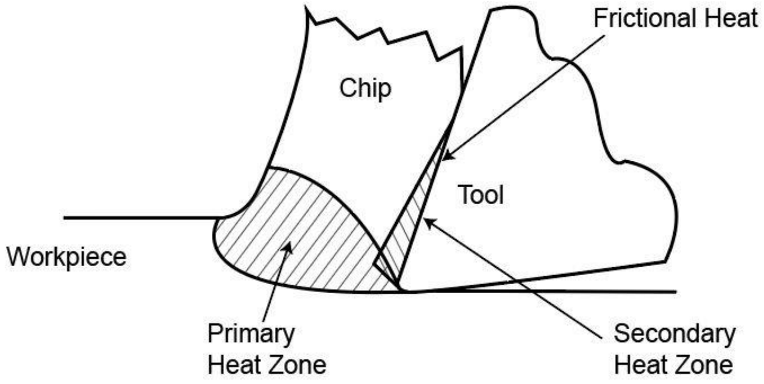

Figure 13: Zones of heat generation in machining.

Almost 25% of the heat is generated at the Secondary Shear Deformation Zone (SSDZ) as a result of friction. This affects the tool-chip interface temperature and is directly associated with the intensity of crater wear. The third zone is the area of the tool flank surface/workpiece interface. It is known that wear on the tool's flank face determines the quality of the newly formed machined surface. It worth noting that the greater portion of the heat generated in these zones is taken away by the chip, while the rest is absorbed by convection into the tool. If no coolant is used, the amount of heat lost to the surrounding environment is negligible [11],[22].

Many methods of calculating temperatures in machining are used in practice, such as: the moving heat source method; method of image sources; finite difference method; semi analytical method and the finite element method. This work will not address the methodologies used but will focus on the results of their studies instead.

A result of a study conducted by Tay 1974 [23] depicted in Figure 14 shows the temperature distribution during machining steel at Vc=155.4 m/min and t=0.24mm/rev using a carbide tool.

The maximum temperature (1016 ^{o}C) was found to occur just beyond the midpoint of the tool-chip contact length [11].

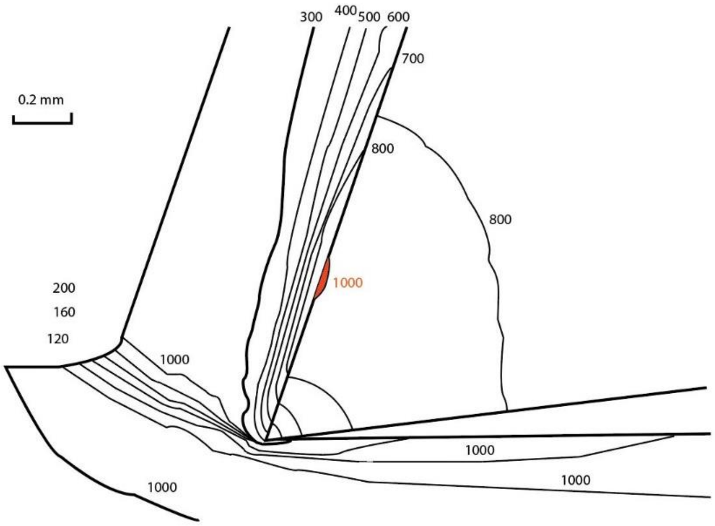

Figure 14: Temperature distribution by Tay 1974. Adapted from [11]

This experiment shows maximum temperature aligns with the region of crater wear and is consistent with the results of other researchers [11], [22], [24] that highlight the trend of maximum temperature formation on the rake face under multiple methods and materials.

In general, the COF depends on the temperature as can be seen in Figure 15. Bailey relates this effect to thermal softening of the workpiece material [17]. The work of Zorev [18] also agrees with the aforementioned trend.

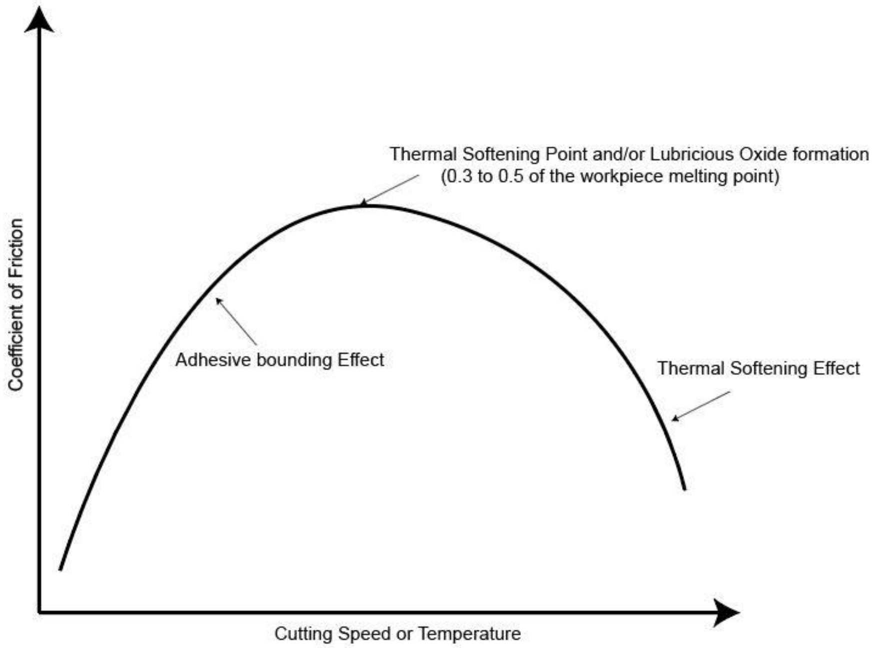

Figure 15: Coefficient of friction influence according to temperature.

The reason why COF depends on temperature is that as adhesion intensifies, temperature increases up to a maximum point at which the shear strength, reduced by thermal softening, starts to overcome the effect of adhesion. Using carbide and steel at high pressures and temperatures, this limiting peak occurs at 0.3 to 0.5 of the temperature required for the workpiece to reach its melting point [25].

Although a major aim of designing a tool coating for machining is to reduce friction while supporting a high temperature in the cutting zone subject to temperature reaching a point where is causes excessive crater wear.

CHAPTER 3. DEVELOPMENT OF THE TRIBOMETER DESIGN

Increasing the productivity of machining would require the development of an accurate simulation of the machining process in order to identify the optimal cutting parameters. Such parameters include tool material, geometry and coatings. However, as discussed earlier, processes that develop within the cutting zone present a challenge to accurately model.

The Coloumb model of classical friction is typically used to model friction during machining. It is based on the assumption that the coefficient of friction is constant along the entire contact length of the tool independently of the temperature and pressure. According to Trent [26], sliding speeds in the cutting zone are not constant and vary along its length due to adhesion within the sticking zone. Moreover, Zorev's equations show that pressure also changes along the length of the tool/chip contact area during cutting. All these instabilities greatly affect the value of the coefficient of friction and as such, the Coloumb model of friction is inapplicable in this scenario.

According to [7], [15] purely analytical methods for obtaining the coefficient of friction values are insufficient. Thus, the accurate measurement of COF requires an empirical approach.

3.1. COEFFICIENT OF FRICTION'S TESTS

There exist two types of experimental setups: the machining process itself and tribological laboratory tests. Machining experiments are usually performed through the turning of a tube of workpiece material to simulate orthogonal cutting. Forces and temperatures are measured during the experiment, followed by a further analysis of the chips, tool surface and workpiece surface. Unfortunately, it is impossible to obtain detailed information about the localized pressures and temperatures in the contact zone which occur during the machining process.

Special instruments, known as tribometers are used to measure friction in tests. Tribometers are used to assess the following characteristics of the friction process: friction force, coefficient of friction and wear volume. The main advantage of the laboratory test is that it allows certain process variables to be distinguished and excluded from measurement. The most common type of testing apparatus used to obtain the coefficient of friction is the pin-on-disk tribometer described in ASTM G99.

The pin on disk test can be used to obtain wear rates and COF values. It usually consists of a stationary pin made from a harder material brought into contact with a rotating disk made of a softer material, as shown in Figure 16. The load applied onto the pin leaves a wear track on the disk. The frictional force is then measured in its relation to the normal applied load from which the coefficient of friction could then be derived.

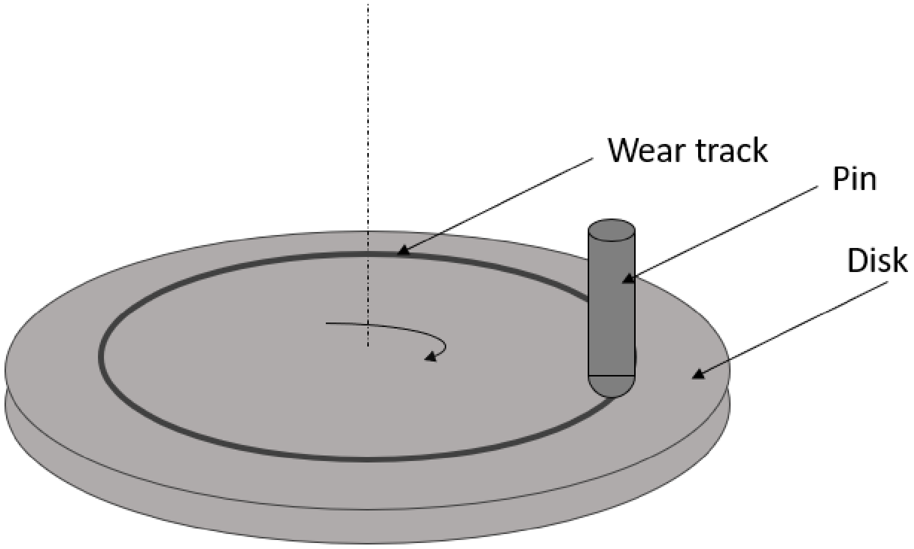

Figure 16: Pin-on-disk tribometer

However, such tests fail to account for the specific conditions that are present during actual machining. Pin-on-disk tests are limited by a maximum pressure of 1GPa, they are difficult to operate under a high temperature and it is difficult to maintain a freshly generated, chemically reactive surface in contact with the pin.

3.1.1. Overview of Machining Tribometers

These limitations are well known in the machining field. Several studies proposed solutions to them in the form of controllable machining conditions in the experimental setup. Some of these solutions will be outlined below.

Hedenqvist [27] created an experiment which consisted of a spirally rotated cylinder in contact with a tube that was being turned in a machine lathe. This setup features a sliding velocity typical for a machining speed of 3m/s but the contact pressures are insufficient to mimic the actual pressures on the rake surface of the tool (~15MPa).

Grzesik [28] developed a device that measures the friction force of a round insert brought into contact with a rotating tube at a high speed of 3m/s. The pressure between the insert and the tube did not exceed 10MPa. In his experiment, just like in a pin-on-disk tribometer the tool acted on the same track and the surfaces were never renewed [29].

To overcome this problem, Olsson [30] measured the friction force of a pin placed just after a cutting tool removed a layer of material, thus renewing the surface of a tube. The speeds and temperatures were similar to those of actual machining, but this setup can only function up to a pressure of 15 MPa.

Based on Olsson’s experiments Zemzemi [29] attempted to resolve the lack of rigidity in this system. He managed to increase the operating pressure up to 3GPa under similar experimental conditions and obtain velocities of up to 16m/s. He measured the temperatures with a thermocouple connected to the pin holder to quantify the heat flux passing through the pin.

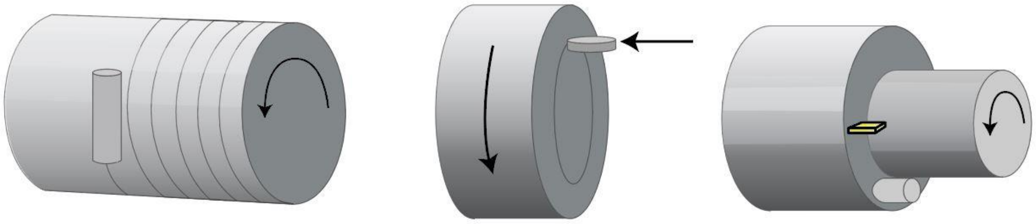

Figure 17: Machining tribometers: Left) Hedenqvist [27], Centre) Grzesik [28], Right) Olsson [30], adapted from [29].

Puls, a researcher from Aachen University in Germany, developed a tribometer which used a vertical broaching machine [31] . A conventional C-type turning insert was used in this design, whose rake surface had a negative angle that slid over the surface of several workpiece materials. The temperature was measured by a two-color fiber pyrometer and this experimental setup managed to achieve a velocity of 100m/min and pressure of 2GPa.

However, a significant issue with the above tribometer designs was brought up by Lyapin [16]. The presence of volumetric deformation affects the measurements of the adhesive bound's shearing loads. Careful analysis in [16] was made to eliminate the influence of volumetric deformation in the material. An accurate measurement of the adhesive bonds could be achieved by a spherical indenter being rotated at a constant speed between two flat samples brought under a load. This simulates the adhesive interaction of a single asperity in the contact, as described in Figure 18.

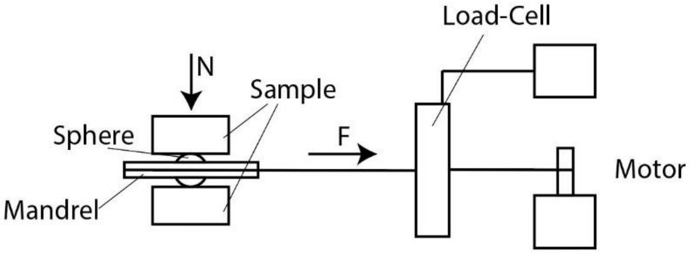

Figure 18: Lyapin’s tribometer components schematics [16].

In Lyapin’s setup, a spherical ball was pressed into a special mandrel that has a circular groove for a wire to be rolled over it. A drive unit pulls the wire and rotates the ball. The force F necessary to rotate the indented sphere on its own axis is measured. Two samples press the sphere under a normal load N applied in the axis perpendicular to the direction of rotation. After the test, the measured imprints could be used to calculate the stresses and the COF.

On the basis of Lyapin’s tribometer design, Shuster 1999 [15], attempted to formulate a more accurate simulation of real machining conditions. This updated method consisted of two flat samples being pressed against an indenter to isolate the adhesive component of friction, but instead of a ball, Shuster used a pin with two hemispherical ends.

Shuster also incorporated a heating feature in his tribometer design, in which the interface was heated by two electrodes attached to the base of the samples. Temperature was increased gradually to prevent localized overheating that could result in the formation of thermal stress. This tribometer design was reported to have achieve a similarly high temperature gradient to that of the tool-chip interface during real machining.

Based on the design of both Shuster and Lyapin’s tribometers, Biksa 2010 (a former MMRI student) modified a pin-on-disk tribometer from Nanovea® to imitate high-temperatures (up to 1000°C) and high-loads (3GPa). The main difference was the method of heating (inductance); only one side of the hemispherical pin in contact with the sample was heated. The other end was securely fitted into the rotational station [3].

Boyd [2], had used the same tribometer in his tests, but improved its GUI – Graphical User interface for ease of use and better adaptation of the resistance heating method. He found that inductance heating was softening the bulk of workpiece material, which would yield temperature gradients not found in actual machining.

Khoei [1] used the same tribometer as Boyd 2012 to perform the tests. He made use of several coatings and workpiece materials, in addition to varying the pin's radius. He found it difficult to reliably align the pin with the torque sensor and reported other issues with the test that could potentially compromise the repeatability of its results.

Since this work is based on the modifications of the same tribometer design, the next section will provide a more detailed description of its operation.

3.2. MMRI TRIBOMETER

3.2.1. Overview of the Existing MMRI Tribometer.

As previously mentioned, the MMRI Heavy-Load and High-Temperature tribometer is a modification of the Nanovea pin-on-disk tribometer based on the designs of Lyapin and Shuster. The main purpose of this device is to perform measurements of the COF under conditions approaching those of an actual machining process.

In this tribometer, developed by Biksa (Figure 19), a 3 mm diameter pin, made from the tool material is placed in a mandrel aligned to a precise Kistler reaction torque sensor (Kistler Model 9329A). A flat sample made from the workpiece material is placed on a rotational stage and rotated on the same axis.

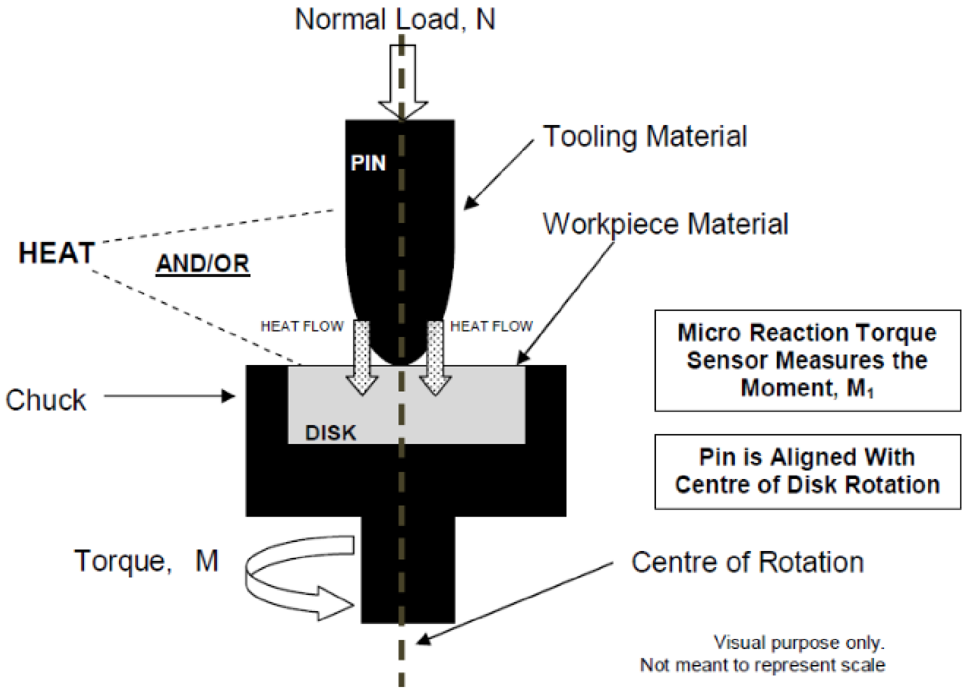

Figure 19: MMRI tribometer schematics [3].

The normal load is produced by a pair of ball screws that move the aluminum support bar which is regulated by a PID controller. A load cell (0 to 3000 N) is connected by one end to the support bar. The other end is fitted, via screws, to a splined shaft guided through the support bar that only allows axial movement.

Heat is provided by a welder (Miller MaxStar 200) with a 200 Amp current supply. One of its ends is connected to a copper plate located at the bottom by a graphite ring contact which allows the plate to rotate. The other end is connected to a mandrel at the top holding the pin which completes the circuit.

This way, the top part connects the pin that applies the normal load to the sample. The bottom part holds the sample secure and provides rotational torque. Heat is generated by the resistance heating method at the points in the circuit where electrical resistance is higher, which in this case is the point of contact between the pin and the sample.

The temperature attained on the contact is measured by a two-colour Optris CTlaser pyrometer (LT-CF2) emitting two beams that converge at a single location 150 mm away from the pyrometer and 1 mm above the point of contact. The pyrometer measures temperatures within a range of -40 to 975°C to an accuracy of 0.1°C.

The tests needed to be performed according to the following conditions [1]:

- Samples have been ground and polished.
- Surfaces of the samples need to be parallel.
- The mandrel containing the pin should be aligned within 20 microns to the center of the sample's rotation.
- The sample should be rotated at a constant RPM.
- The temperatures must be constant prior to rotation.

3.2.2. Problems with the MMRI Tribometer

The main problem reported by Khoei [1] was the difficulty of pin alignment. The pin was fixed within a mandrel which was intended to tilt the axis of the pin into the desired position. The cylindrical mandrel was then secured to the top plate guided by two pins which positioned it concentrically to the torque sensor. Fixing the mandrel in the concentric position and adjusting the tilt of the pin was a time-consuming task aggravated by the extremely sensitive torque sensor that could overloaded and permanently damaged by out-of-alignment issues.

The system's parts, displayed in Figure 20, consist of a rotational base, sample, pin, mandrel, guided top-electrode, insulation polymer, torque sensor, and top stage.

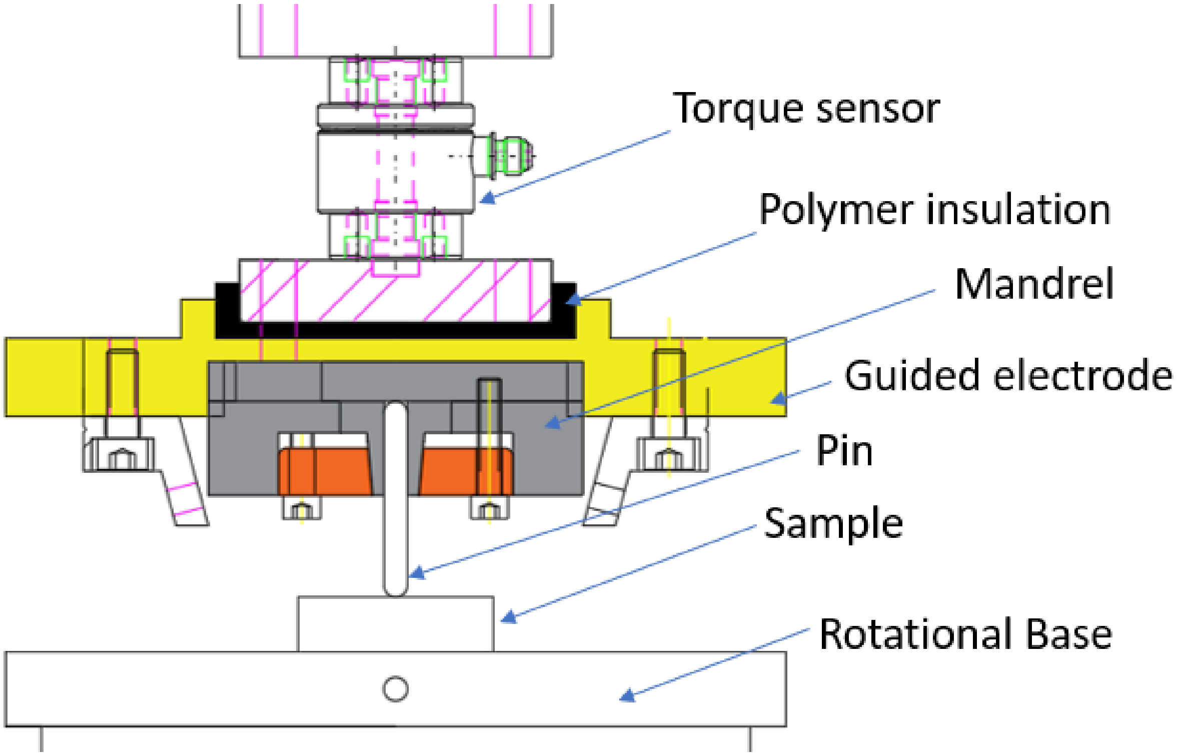

Figure 20: Current tribometer components alignment setting.

For tests to be performed consistently, the top stage needs to be axially aligned with the rotational bottom stage within a tight tolerance. Achieving an alignment precision of below 20 microns presented a major challenge due to the following factors:

1. The rotational stage must be parallel to the top plate during all stages of rotation.
2. The sample must be parallel on both sides to prevent the slipping of the pin.
3. The pin must be axially aligned with the torque sensor and with the rotational stage.

4. The mandrel should allow fine adjustments to be made to the pin tilt without applying too much torque to the screws that hold the pin in place and also to the ones that hold the mandrel in place to avoid torque overload.
5. The polymer insulation was prone to aggravate the alignment problems once the normal load had been applied. Only a small disparity in the alignment of the tilt was enough to compromise the alignment. Due to repeated heating and cooling of this insulation, this part could undergo unexpected dimensional changes over time.

In summary, an experienced operator would require ten to twenty minutes to align the system. Even after calibration, issues with alignment can still arise after the load is applied. The precision of pin alignment is assessed at the end of the entire assembly by a dial indicator connected to the rotational stage and the top of the pin. If the tolerance is found to be in excess of 20 microns, the alignment has to be performed again.

Due the inconvenience of alignment for each test, a simpler design based on the older approaches of Lyapin and Shuster was proposed and implemented together with several other changes to the testing conditions used, which will be described in the next section.

3.3. MODIFICATIONS TO THE MMRI TRIBOMETER

3.3.1. Double-Sided Pin Approach

To overcome some of the previously addressed limitations, the double-sided pin may present an interesting option due its design simplicity and ability to mitigate misalignment errors.

The double-sided pin set-up consists of a two-sided pin with hemispherical ends made from a tribo-system’s harder material, which are sandwiched between two flat and parallel samples made from the tribo-pair softer material. Both samples and the pin are then placed in a press and compressed, after which the pin is rotated around its axis, perpendicular to the sample faces. The rotational force is then measured and the coefficient of friction is calculated.

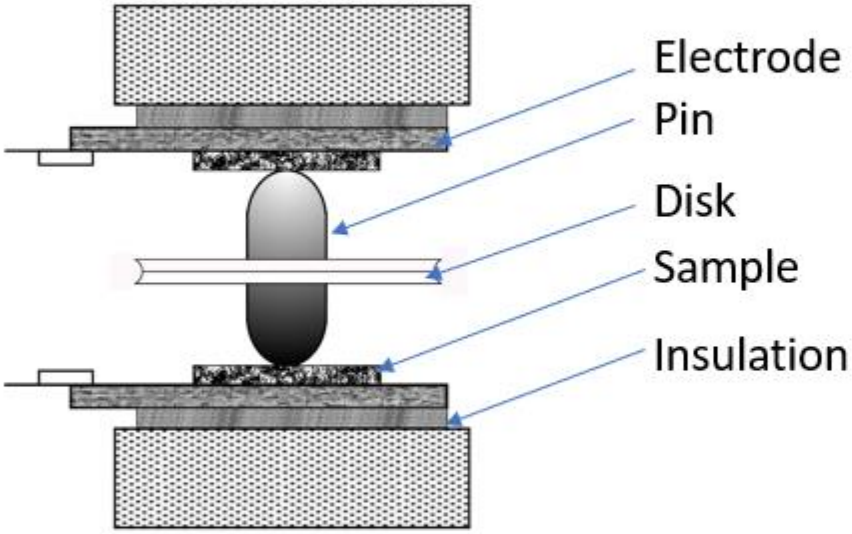

Figure 21: Double-sided pin experiment schematics

A stage is needed to rotate the pin. This is done by pulling on a wire wrapped around an attached pulley disk. To extend the pin's size without making it unnecessarily large, the pulley is designed to accommodate its dimensions as well as that of the wire. To adjust the sensitivity of the tension needed to pull the pulley, different pulley sizes could be attached to the pin, since the force needed to unroll the pulley adheres to the following Equation 3-1.

$$Torque = Tension \times Radius \qquad \text{Equation 3-1}$$

Since the torque lies in a certain pre-determined range, it is possible to adjust the radius necessary for the pulley to accommodate the tension measured by the load cell.

Using the bottom plate as a reference, is possible to guarantee the perpendicularity of the pin by placing precision ground parallel parts to lay the pulley over it. Since the pulley centre hole is machined perpendicular to the bottom face of the pulley, the parallels parts are used as an extended reference of the bottom plate.

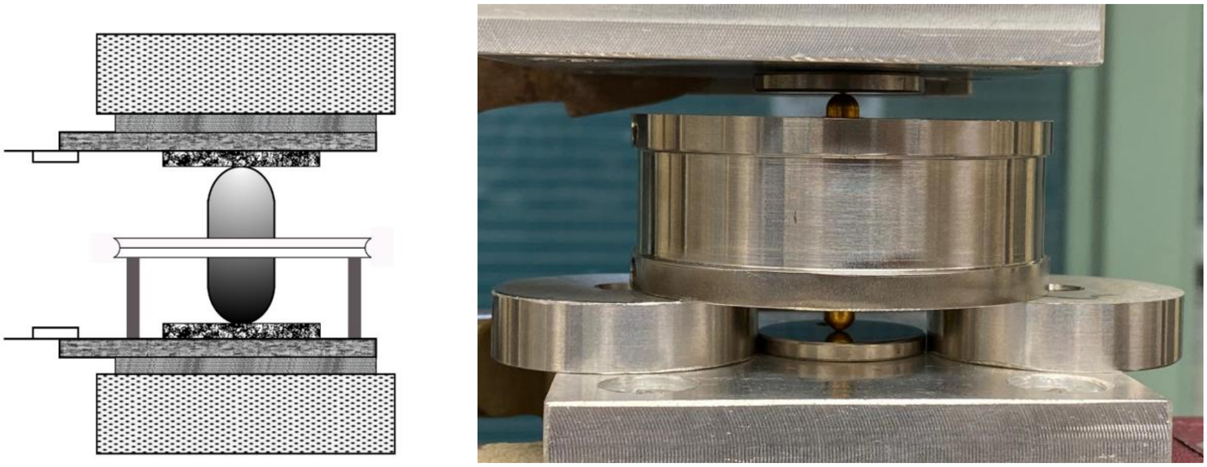

Figure 22: Parallels aligning the pin and pulley.

Another benefit of this approach is that even if a small misalignment occurs, the errors in the torque measurement will end up being negligible, since the shape of the imprint will still remain hemispherical and provide a counterbalance between the top and the bottom imprint, resulting in only a minor deviation of the normal load. Although, it is expected that the better the alignment is the better the results obtained will be.

The time needed for proper pin alignment has been thus reduced from 10-20 minutes, to just under 4 minutes.

The double-sided pin approach may also offer several other benefits compared with the single-sided approach. These benefits will be listed at the end of this section.

3.3.2. Temperature Requirements

Temperatures within the cutting region can reach above 1000°C during machining [23][12]. It is not only important to record the machining temperature but also to maintain a proper temperature gradient to prevent premature seizure of the material sublayers due to thermal softening.

To mimic the conditions of a real metal cutting process, the pin needs to provide enough pressure to leave an indent in the softer material.

To reach the temperatures in the cutting zone, the contact area needs to be heated by electrical resistance welding. A 200A welder is attached by its terminals to the plates that hold the softer samples. The pin and the disk are part of an electrical circuit which generates heat according to the equation.

$$Q = I^2 R\ t$$

Equation 3-2

Where Q (Joules) is the heat generation, I (amperes) is the current provided by the welding machine and R (ohms) is the electrical resistance of the system and t (seconds) is the time for which the current is applied.

The contact electrical resistance R is the most important parameter of resistance heating. It decreases with the increase of the real area of contact. The contact electrical resistance is the resistance of the current passing through the asperities in contact as shown in Figure 23. The greater the amount of asperities in contact, the more freely the current passes through and the lower its R value. Since the number of asperities in contact is a function of the applied load and roughness of the contacting bodies, it is worth noting that it would be difficult to reach a high temperature in highly loaded contacts with a low surface roughness. It should also be mentioned that the contact electrical resistance depends on several factors such as: pressure applied to the electrodes, tip geometry as well as material.

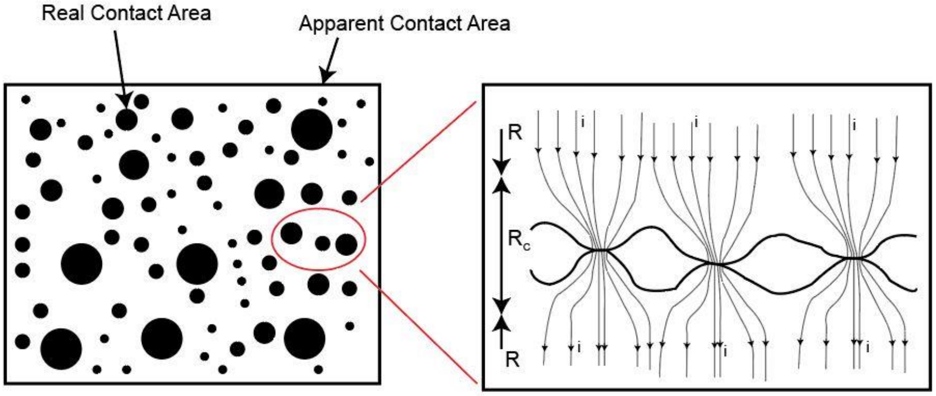

Figure 23: Influence of the real area of contact on electrical contact resistance. Left) Top view of surfaces in contact. Right) profile view from the contact points, adapted from [32]

One notable aspect of this kind of welding is the fluctuation of electrical resistance during heating. Electrical resistance is represented by a dynamic value due to changes in the material properties as well as the increases in the points of contact at the interface, which makes it difficult to entirely control and predict.

As previously noted, the current passes through the electrode terminals and heat is generated where the electrical resistance happens to be higher. The point of highest electrical resistance can be found right on the top and the bottom of the pin-disk interfaces, as shown in the Figure 24. The temperature gradient thus becomes comparable to that of the tool/chip interface. According to [15], this represents the proper condition for a friction test [7], [15], [16].

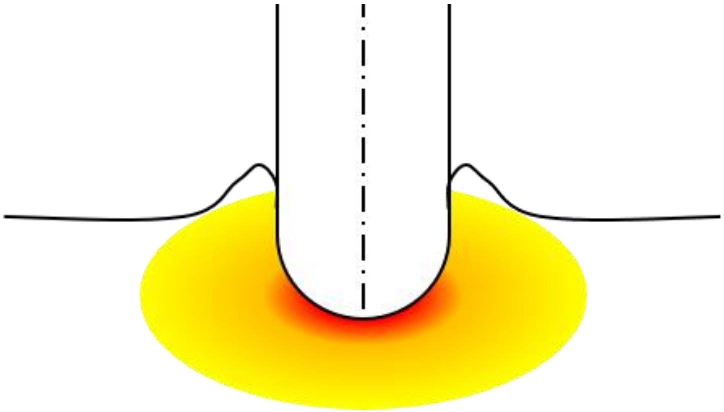

Figure 24: Resistance heating representation in the pin.

Since heating conditions depend on several difficult to manage variables of the system, temperature control will only be enacted by means of the normal load and current applied by the welder.

3.3.3. Normal Stress Requirements

As already mentioned in Chapter 1, an equal range of stresses need to be present on the rake face to suit the load requirements. The chip becomes plastically deformed during machining and slides over the rake face in two different regions.

In the first zone, known as the sticking zone, the workpiece material adheres to the tool surface due the high normal load causing seizure. Shearing stress at the rake face is highest and constant in this zone. It characterizes the failure of the chip material, which is flowing in a velocity pattern similar to a fluid.

Within the next zone, called the sliding zone, the material is sliding along the rake face of the tool under variable shear stress. In this region, the two-contacting materials experience shear stress (tool material and chip material) which is a characteristic of adhesive interaction.

The normal load in our experiments always depends on the indenter size and geometry. ASTM standards for Brinnel hardness provide a solid indication of the load needed to establish total plastic deformation within the zone of indentation.

The goal is to be within region two of the graph shown in Figure 6 of Chapter 1, under conditions above sliding yet below seizure, as shown in Figure 25.

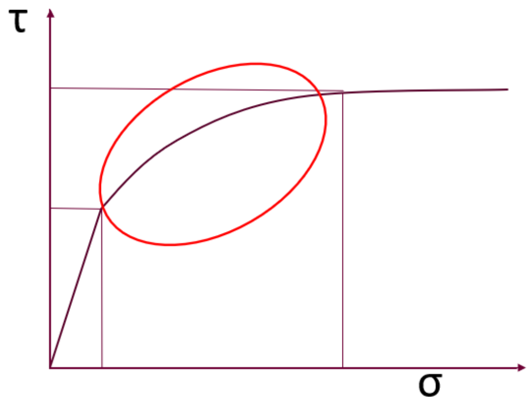

Figure 25: Shear Stress by Normal Stress showing the region of interest in sliding conditions.

To control the pressure applied to the pin/sample interface, it is necessary to measure the total load on the system. For this purpose, a Nanovea® load cell was applied with a specified range from 0 to 3000N. A software program controls the motors and ball screws that adjust the amount of load in a closed loop, since the material's resistance changes during the test due to the rise in temperature and strain hardening.

3.3.4. Shear Stress Requirements

To find the frictional shear stress of the rotating imprint, Lyapin and Shaw calculated the shear stress of an infinitesimal area of a hemispherical circle in spherical coordinates [16]. The sphere in Figure 26 is assumed to be in contact with the flat sample over the entire geometric surface of the impression.

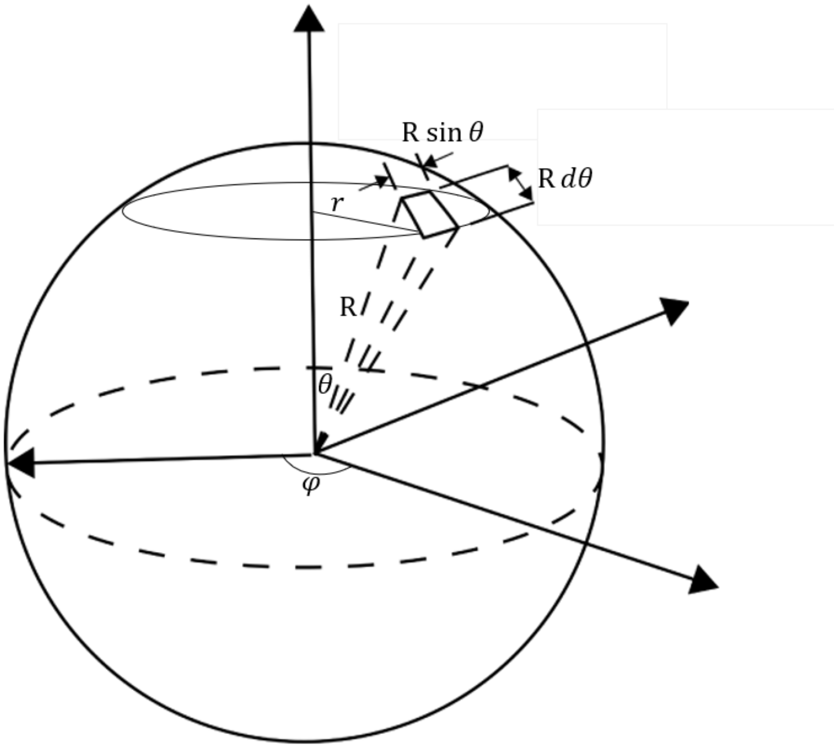

Figure 26: Spherical indenter in spherical coordinates.

Average shear stresses τ_n can be calculated from the moment M given by the equation:

$$M = 4\int_0^{\theta}\int_0^{\pi/2} \tau_n \cdot r \ \cdot R^2 \cdot \sin\theta \cdot d\theta \, d\varphi \qquad \text{Equation 3-3}$$

Where, r is the radius of the imprint and R is the radius of the sphere. Assuming that:

$$r = R \sin\theta \qquad \text{Equation 3-4}$$

Substituting Equation 3-4 into Equation 3-3 and integrating the resulting rotational moment of the sphere, yields the expression:

$$M = \frac{4}{3}\pi\,\tau_n r^3 \qquad \text{Equation 3-5}$$

The rotational moment of the pulley is given by:

$$M = F_{ex} \cdot R_{ex} \qquad \text{Equation 3-6}$$

Where the $F_{ex}$is the tangential force needed to rotate the pulley and R_{ex} is the radius of the pulley. Combining the two equations gives:

$$\tau_n = \frac{3}{4}\frac{F_{ex} \cdot R_{ex}}{\pi \cdot r^3} \qquad \text{Equation 3-7}$$

The normal load of a spherical indenter is provided in Equation 3-8:

$$\sigma = \frac{P}{\pi r^2} \qquad \text{Equation 3-8}$$

Where P is the normal load. The coefficient of friction can be obtained from shear stress divided by the normal load:

$$COF = \frac{\tau_n}{\sigma} = \frac{F_{ex} \cdot R_{ex}}{r \cdot P} \qquad \text{Equation 3-9}$$

The COF can thus be expressed in terms of the three measured parameters. Two of the parameters can be directly obtained from the tribometer's measurements (normal load and tangential load) and the last one is yielded by dimensional measurements made on the imprint.

3.4. SYSTEM AND COMPONENT DESIGN

The new setup of the MMRI high load high temperature tribometer can be subdivided into groups, each of which perform a different function in the system, as depicted in Figure 27.

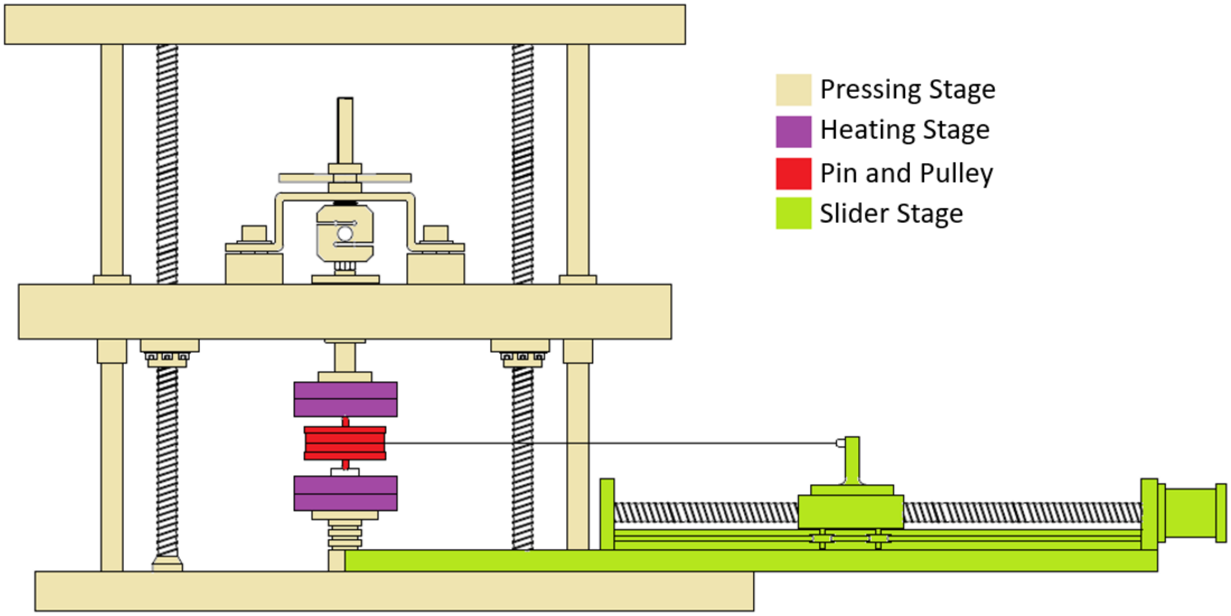

Figure 27: New Design group schematics

The first group is the pressing stage that supplies the system with normal stresses and load measurements. The second group is the heating stage which provides electrical and heating energy as well as their insulation. The third group is the pin and pulley that creates the tribo-contact and the fourth is the slider stage which carries out rotation and torque measurement.

3.4.1. Pressing Stage

The pressing stage provides normal force to the experiment. A motor generates torque by means of a timing belt and pulleys to a pair of ball-screws that move the crosshead up and down. The crosshead is made out of stainless steel to avoid vibration interference during the tests [3].

A THK® 16mm model LT16 rotating splined shaft is located perpendicular to the centre of the crosshead.

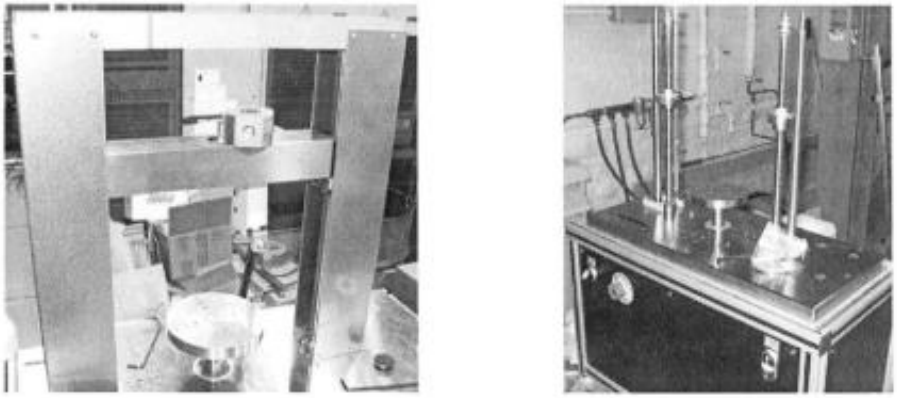

Figure 28: MMRI tribometer structure assembly [3].

The upper end of the shaft is attached to a Nanovea® load cell with a range of 0 to 3000N by a compliance mechanism that fixes the load cell to the upper part of the crosshead. The load cell is used to capture load data from the pressing of the pin and to control the motor rotating the ball-screws. Two parallel linear guide shafts and brass bearings ensure the crosshead always moves parallel to the base.

The bottom part of the pressing unit consists of a rotating column attached to the base. The rotating column is used to withstand the pressure coming from the top splined shaft, which is there to ensure the pin does not rotate when the plate below rotates.

3.4.2. Heating System

The heating systems are based on the electrical resistance heating principle, which states that the heating of an electric circuit is directly proportional to its electrical resistance points. In the setup, the electric resistance of each material is much smaller than the electrical resistance of the contacts. As a consequence, more heat will be produced in the junction. Supplying current to the system transforms it into a circuit, which heats the parts in accordance with their electrical resistance. A model of the heating electrical circuit is depicted in Figure 29.

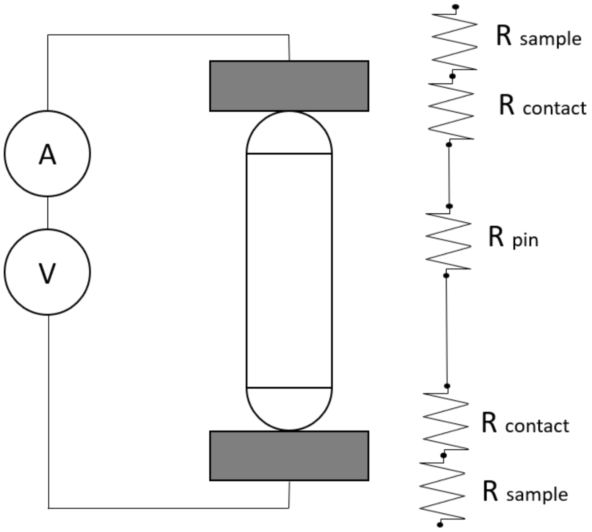

Figure 29: Simplified electrical circuit of the tribometer.

In every circuit in the tribometer, each resistance point draws some voltage from the source. The drop of voltage in the first resistance point can reduce the voltage that reaches the second contact. A further study of this will be provided in the next section.

A 200A electrical circuit is provided by a Miller model MaxStar 200 welder machine and two thick gauge cables connected directly to the upper and bottom electrode plates made from aluminum.

These plates are large enough to support the samples being pressed in several positions and possess enough mass to absorb heat, thereby creating an appropriate temperature gradient on the samples' interfaces.

The electrode plates must be electronically insulated from the rest of the assembly, otherwise high electrical current from the welder will damage all the tribometer's electronic components.

To ensure these components are insulated, a ceramic plate was placed between the top pressing column and the top electrode and another plate between the bottom rotating column and the bottom electrode. The ceramic material of choice is commercially known as MACOR. This material has a number of unique properties desirable for this application, such as high compressive strength at high temperatures (345MPa up to 900Mpa of strength in conditions up to 800^{o}C) and a coefficient of thermal expansion matching most metals (81-123 x 10-7 /°C), which helps prevent stress in the entire assembly. Unlike most ceramics MACOR is extremely machinable which facilitates fabrication.

3.4.3. Pin

The pin used in the test is made of tungsten carbide WC6%Co and has a 2.5mm radius hemispherical end on both sides, in accordance with ASTM Brinell test standards (E10). The length of the pin is 35mm, which helps avoid buckling at high temperatures. The spherical ends follow the technical standard laid out in ISO 3290:2014 GRADE 40. The dimensions and tolerances are described in Figure 30.

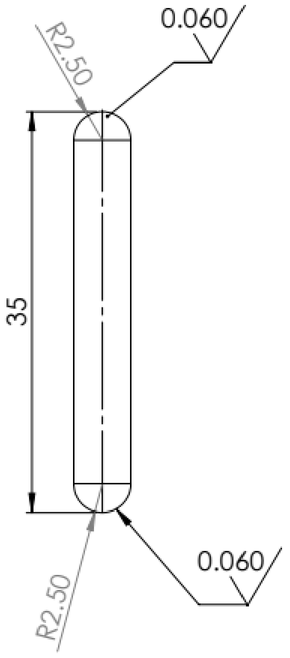

Figure 30: Pin dimensions and tolerances

The mean surface roughness of the pin tip should not exceed Ra = 0.00005 mm, otherwise the data will be saturated with irrelevant physical and mechanical phenomena. However, the effect of roughness will be assessed in the next chapter due the high cost of achieving this level of finish.

Increasing the size of pin curvature from 3 mm to 5 mm, reduces the parallelism errors by as much as 4x, according to ASTM E10 standards for Brinell hardness tests. Tests were conducted by 5mm indenters on a Ti64 sample prior to altering the setup to assess the plastic deformation taking place within the imprints.

3.4.4. Pulley

In order to provide more torque to the rotational movement of the pin, a special pulley was designed to securely hold the pin inside the bore hole during the test. The pulley is made from AISI 316 Stainless Steel and has a 5mm h7 precision reamed bore hole along its axis for fixing the pin in same place for each test. An outer groove of 30 mm radius was machined concentrically with the bored hole. The dimensions and specifications of the pulley are described in Figure 31.

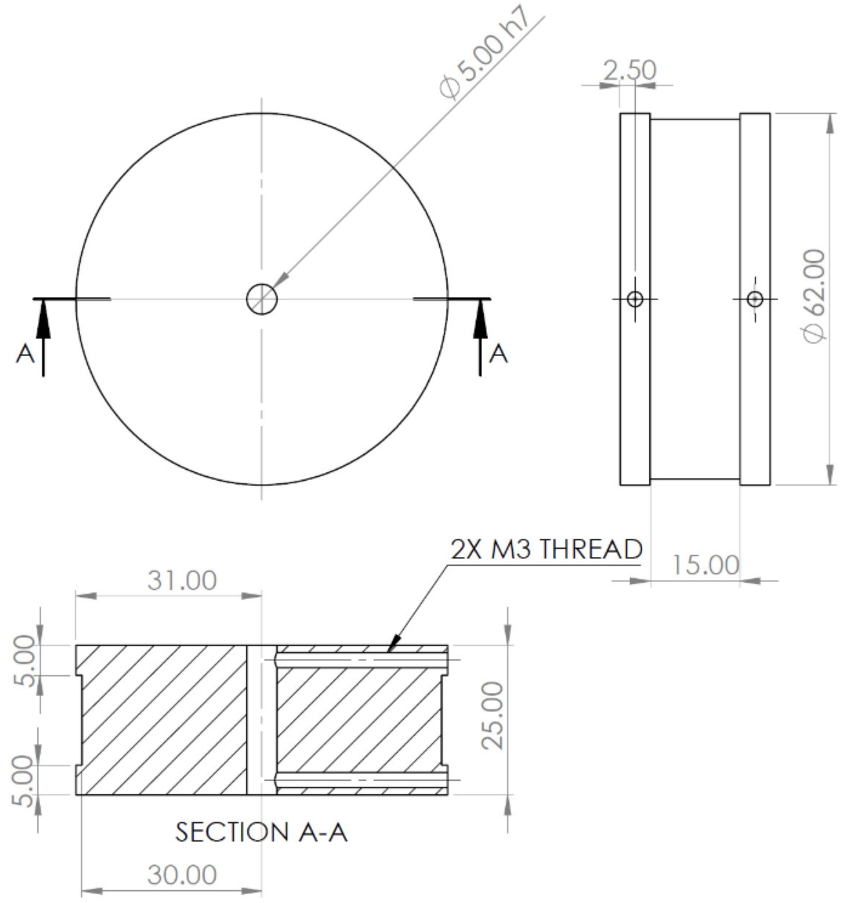

Figure 31: Special pulley technical drawing.

To prevent the pin from slipping due to increasing torque, a pair of screws are drilled into the side of the pulley to securely hold it in place.

3.4.5. Slider Stage

A separate stage was created to generate and measure the pin's torque. This stage enables the test to be performed using the previous setup without the time-consuming reassembly of several components.

To provide torque to the pulley, a very thin wire was rolled through one of its ends, with the other being fixed in a load cell. The model SEN-13329 parallel beam load cell ranged from 0 to 10 (±0.05%) kgf and was fixed and pulled by a linear guide block. The range of this load cell was chosen for its ability to measure torques of up to 3N.m in combination with the 30mm radius pulley. The load cell was connected to a HBM AE301 amplifier linked to the LabView system and calibrated by applying known weights.

The 400 mm linear guide rail is attached to the base of the tribometer, allowing the slider block to travel along its length, as shown in Figure 32. The setup consisting of the guide block and the load cell is put in motion by a step-motor and ball-screw. The linear guide produces horizontal loads of up to 150N at a speed ranging from 1 to 50mm/s, which is enough to pull the wire.

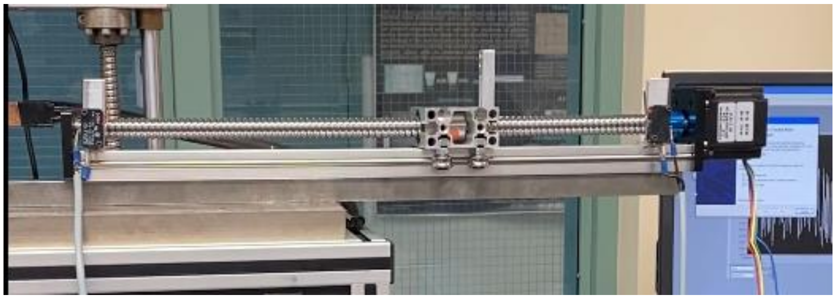

Figure 32: Linear guide

The stepper motor with 1N.m torque is connected to the other SainSmart ST-M5045 4.5 amp stepper motor drive. The stage is secured by two end keys at the end of each linear guide rail that define the end of travel.

The schematics of the electronic arrangements are shown in Figure 33. All electronic components were welded to the board and a custom program was created for their control.

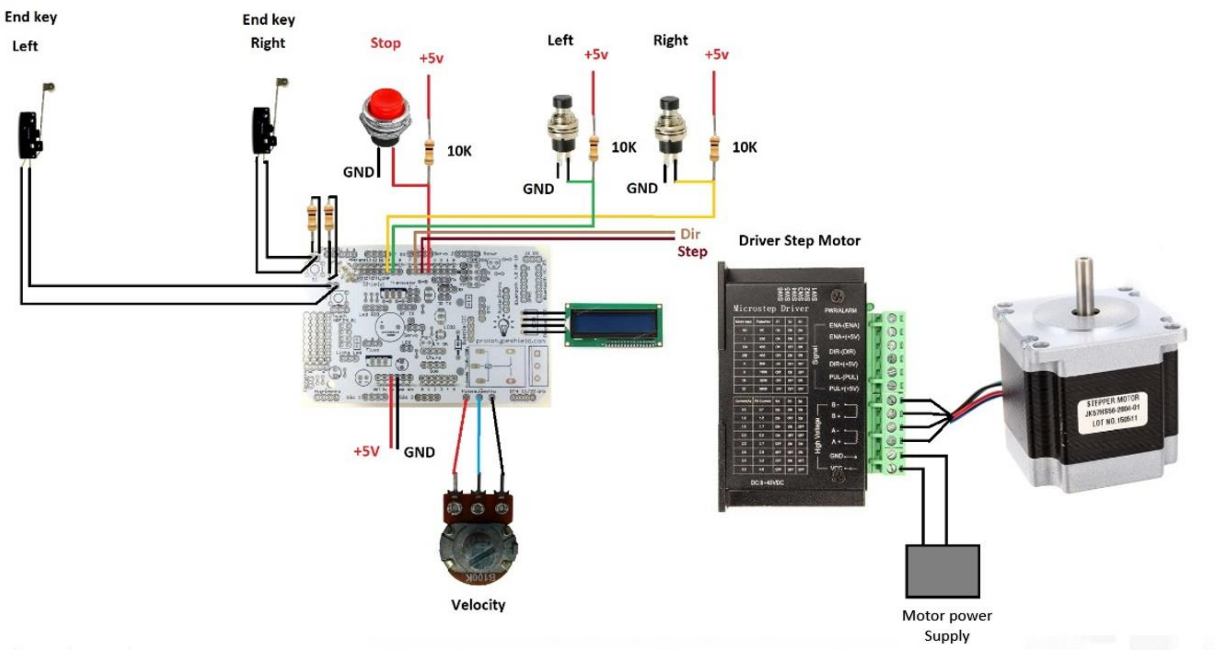

Figure 33: Electronic schematics of the slider.

Since the wire is directly in contact with the energized pulley, an insulated wire holder made from a PLA is attached on the end of the load cell. In order to be aligned with the tangent of the pulley, the load cell is securely fitted in the slider block by an adjustable holder l, as shown in Figure 34.

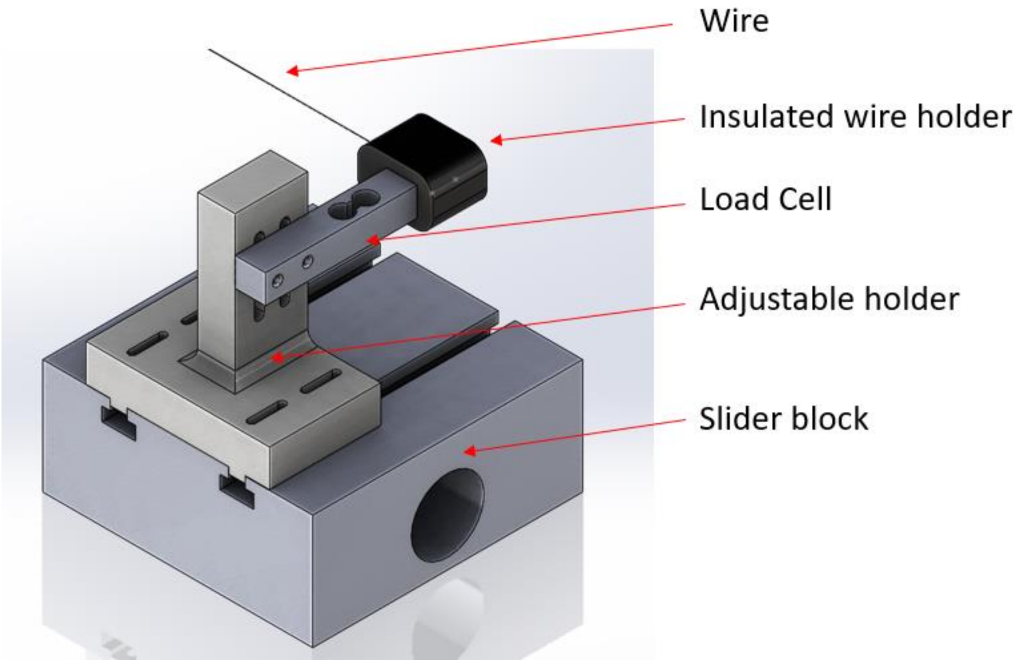

Figure 34: Slider block components.

It is important to have a measurement of torque in the steady state. To achieve this, the pulley must be unrolled at a constant velocity since any variation in speed could cause a spike in the measured forces due to acceleration. However, experiments carried out using this setup have shown that the slider’s speed remains constant throughout the entire duration of the test.

The 400mm length of the slider was selected so that the pin could undergo two complete rotations in one test cycle. Torque measurements were shown to have reached the steady state prior to the first rotation of the pin.

3.4.6. Temperature Measurement and Control

It is impossible to obtain a temperature reading directly at the interface between the disk and the pin without affecting the test or the temperature reading. Therefore, a non-contact pyrometer test method was performed using an infrared Optris Ctlaser pyrometer sensor model LT-CF2 with its specifications listed in Table 1. This pyrometer emits two beams converging to one point 150 mm from the sensor.

Table 1: Pyrometer Optris Ctlaser LT-CF2 specifications:

Range	-40 to 975 ˚C
Accuracy	+/-1 ˚C
Resolution	0.1 ˚C

The measurement distance from the pin tip is further explained in the calibration part of this thesis. In experiments where the sample was heated up to a specific point, the temperature at which phase change had occurred converged to the temperature measured 1.5 mm below the pin tip. It should be mentioned that this is only valid for the 2.5mm diameter pins.

In the case of the 5mm pins, the pyrometer's measured temperature diverges from the temperatures obtained by other methods such as thermocouples. The reasons behind this will be discussed in the next section of this thesis.

3.5. SUMMARY OF PROS AND CONS ASSOCIATED WITH EACH SETUP

The Table 2 provides an overview of the pros and cons of each equipment design.

Table 2: Summary of pros and cons for each setup.

	PROS	CONS
Torque measurement using the Kistler model in the same axis of rotation. (one sided approach)	-High sensitivity and reliability of calibration. -Solution is already implemented in the system.	-Hard to set up experiments without overloading it. -Cable movement from the sensor significantly alters the measurements of torque -Highly dependent on good alignment (Ensuring proper alignment of each axis between the pin and the sensor is difficult and time consuming). -Temperature sensitive.
Pulley torque measurement (two-sided approach)	-High tolerance of misalignment errors -Redundant measurement of torque due to twin sided measurement. -Low cost -Fast experiment setup -Easy setup training.	-The misalignment could pass unnoticed during tests and alter the results. -Needs an entire system to pull the sensor with controlled velocity and minimal alignment.
Ceramical insulation	-Thermal stability -High mechanical resistance	-Hard to machine and make parts from it. -Expensive
Plastic insulation	-Easily found -Easy machinability of parts	-Low thermal stability at temperatures above 100°C

		-Misalignment becomes worse due to low rigidity.
2.5mm diameter pins	-Economically more viable -Less load is needed to apply high pressures.	-Prone to alignment issues that severely interfere with torque measurements. -Buckle at high temperatures.
5 mm diameter pin	-Allows more parallelism tolerance between the sample and the test. -Greater area of interaction with the appropriate friction mechanisms without the interference of undesirable frictional components.	-Requires greater load from the machine to achieve higher pressures. -Temperature measurements with the pyrometer could be affected due heat distribution being further from the contact spot. -Expensive pins.
Controlled roughness of the pin	-Reduces the interference of abrasive wear with the test caused by the interlocking and shearing of asperities, thus isolating the adhesive component of friction	-Expensive and time consuming -Hard to assess roughness quality at this scale by rapid means. -Lowers electrical contact resistance

CHAPTER 4. CALIBRATIONS AND EXPERIMENTAL PROCEDURE

4.1. SENSOR CALIBRATION

A custom LabView program developed by [2], [3] collects data from the tribometer's sensors, which include the load-cell for the normal load, a beam load-cell for the friction force and the pyrometer for temperature measurement.

4.1.1. Load Cell Calibration for Normal Loads

A Kistler dynamometer model 9129AA was connected to the pressing stage at a programmed load range of 50 to 2400N. A PDI controller was used to adjust the loads by rotating the ball-screws in the pressing stage. This procedure is shown in Figure 35: Load-cell setup calibration. and results are given in Table 3.

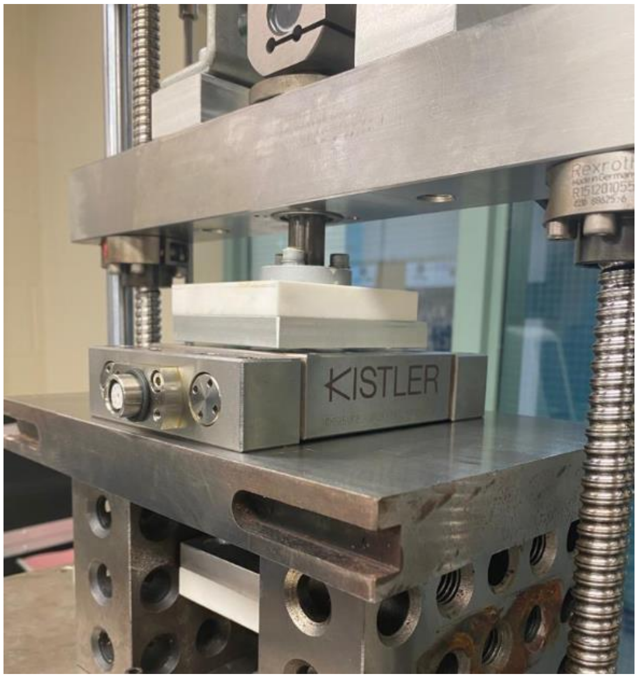

Figure 35: Load-cell setup calibration.

Table 3: Differences in load measurements

Inputted load [N]	Kistler dynamometer load [N]	Error [%]
50	39	22
100	89.5	10.5
200	190	5
600	587.4	2.1
1000	987	1.3
1500	1485	1
2000	1983	0.85
2400	2380	0.83

A safe range of test loads can be established from a graph of load errors. Measurement errors are quite considerable at low normal loads, but after 400N the errors approach the range reported for the equipment error (2%).

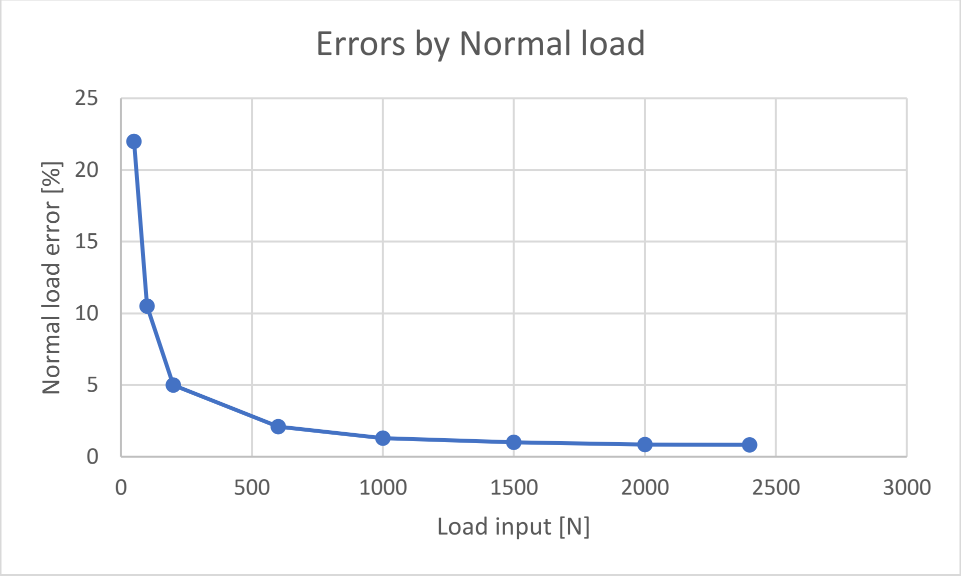

Figure 36: Errors in normal load.

Due the high influence of normal load in the calculation of the coefficient of friction, an error above 5% is not acceptable. To ensure consistency of measurements, all tests in this work were carried out under loads greater than 300N.

4.1.2. Friction Force Calibration

The small beam load-cell with a range of 0 to 100N needed to be adjusted. This load-cell featured small extensometers that altered their electrical resistance when the load was applied to the instrument. A Wheatstone bridge was used to transform the small changes in resistance into voltage signals that could then be acquired by the data acquisition system. A HBM AE301 amplifier was used for this task.

The load cell was aligned using calibrated weights and the tribometer was laid sideways for gravity to act upon. The results of these calibrations are displayed in Figure 37. A line of best fit denotes the trend between the voltage from the applied load and the measured offset voltage.

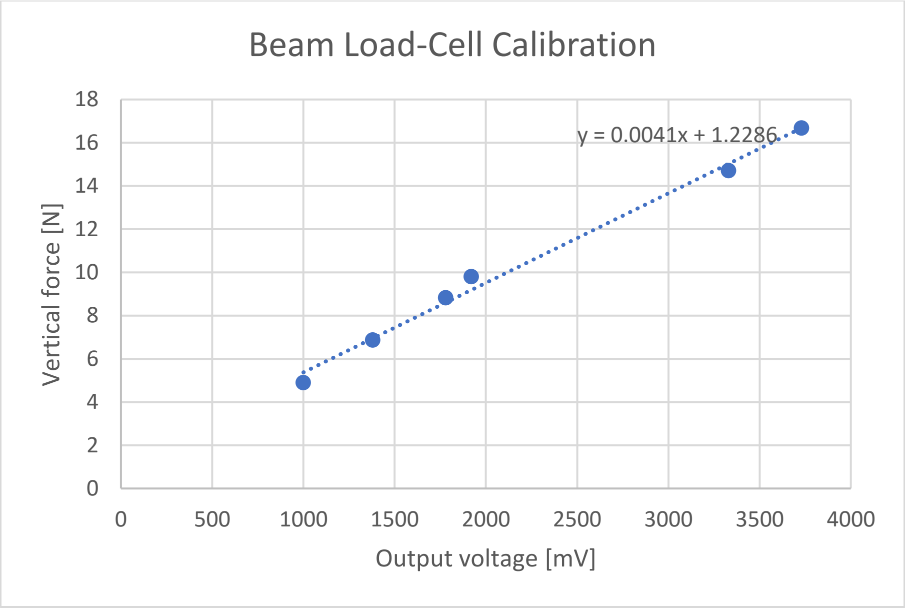

Figure 37: Beam load-cell calibration.

By taking the average of static load values, it is possible to set the average error to ±0.1N in each measurement. Under normal loads below 500N, the error in average force readings can vary as much as 20-40%. Therefore, the loads applied on the tribometer setup need to be greater than 500N to guarantee the precision of measurements.

4.2. EXPERIMENTAL PROCEDURE

4.2.1. Sample and Pins Preparation

The pin is made from tungsten carbide with 6% cobalt acting as a binder. The pins have a diameter of 5mm and a spherical end radius of 2.5mm. The surface roughness of the different pins as well as its effect on the tests were evaluated.

The workpiece samples are prepared in 25.4mm diameter disks with a minimum thickness of 6 mm. Both sides were milled to ensure parallelism between them. One of the sides was then ground and polished to 1μm. The materials chosen in this work were AISI 1045 Steel and ASTM B265 Ti-6Al-4V, whose compositions and properties are listed in Table 4 and Table 5.

Table 4: Material properties of Ti-6Al-4V

Element	Al	V	N	C	H	F	O	Tensile Strength	Yield Strength
Weight max [%]	5.5-6.75	3.4-4.5	0.05	0.08	0.015	0.4	0.2	895 MPa	828 MPa

Table 5: Material properties of AISI 1045 Steel

Element	C	Fe	Mn	P	S	Tensile Strength	Yield Strength
Weight max [%]	0.420 - 0.50	98.51-98.98	0.60 - 0.90	≤0.040	≤0.050	565 MPa	310 MPa

4.2.2. Experimental Procedure

Both samples and pins were cleaned using alcohol and acetone to remove any lubricants or other contaminants that could interfere with the measurement of friction.

One of the samples was placed in the bottom plate, which was located at the centre of the aluminum electrode. The pin was put into the pulley and the sample was positioned in between the two grounded parallels parts. The pulley was placed over both parallels to ensure that the pin was perpendicular to the plate. The pin was then adjusted to touch the bottom sample. The top sample was positioned between the top plate and the top end of the pin. A small pre-load was applied to fix the top sample in place.

The pre-load also pressed at both pin ends, axially locking the pin in place. A stainless-steel wire was passed through the groove and the pulley was rotated twice to make sure that no tangling took place.

To pulley was checked again to certify that it is properly positioned. The parallels are then removed, and the set screws of the pulley tightened to hold the pin in place. A good practice before the procedure was performed was to cut a small slot at the side of the pin to prevent its motion relative to the pulley.

The slider stage was directed to its initial position and the wire was locked into the load-cell holder. Following these steps, the normal load was raised in increments by the force controls of the pressing stage.

The control program was used to select the final load and electric current. The load can be constantly controlled throughout the entire test. The welder will provide a current to the system in increments to prevent localized overheating that could cause thermal stress formation. The selected current must be estimated prior to the test since the process temperature may be altered by material type, roughness, pin size and other parameters.

Once the test was started and the temperature reached steady state, the slider stage was activated and the wire pulled to turn the disk. While this was being done the load required to rotate the disk was measured. All data are recorded in LabView. As soon the slider stage reached its final position, the test was stopped, and the acquired data was then analyzed.

The most important data acquired from the test was the force in the strong associated with the friction torque, the normal load, and temperature. The imprints formed in the samples during the tests were then measured using a microscope by different methods which will be addressed further in this work.

The coefficient of friction can be derived from Equation 3-9 described in the last chapter:

$$COF = \frac{F_{ex} \cdot R_{ex}}{r \cdot P}$$

Where, F_{ex} is the average friction force captured by the beam load-cell, R_{ex} is the radius of the pulley, r is the radius of the imprint and P is the applied normal load .

It is also possible to calculate the normal stress and the shear stress using Equation 3-7 and Equation 3-8 given in the last chapter.

CHAPTER 5. STUDIES

5.1. RESISTANCE HEATING STUDIES

Three different pin sizes were tested to assess the effects of high temperatures on the tribometer system. The limitations of this measurement method will be further discussed in this section.

These tests had the following aims:

- To observe the temperature difference between the two contact areas in the double-sided pin system.
- To record the difference between pyrometer and thermocouple measurements.
- To evaluate the influence of tip radius on the temperature in the contact zone.

The tests were performed under a 1000N load to ensure that plastic deformation occurred in all setups. The two tungsten carbide uncoated pins in the double-sided pin system had a respective radius of 1.5 and 2.5mm, whereas the single sided pin had a radius of 2.5mm. The current was supplied in increments of 20 amperes from 20 to 200 amperes (limit of the welder).

The temperature of the double-sided pin contacts was measured as close as possible to the contact zone, using a thermocouple type E with a probe diameter of 0.5mm, under different currents provided by the welder. The pyrometer measurement was taken 2.5 mm above the contact zone. A current was provided until a steady temperature was reached (approximately three minutes). Figure 38 depicts the points of measurement.

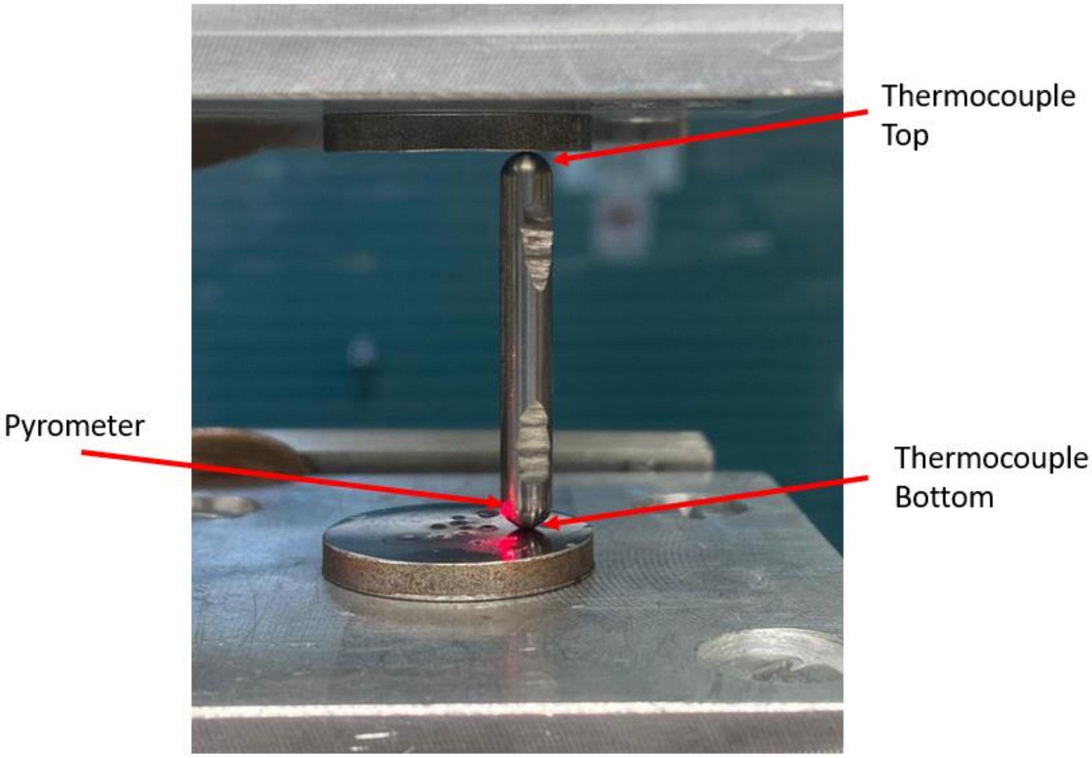

Figure 38: Measurement spots.

The results of the double-sided 1.5mm pin test are shown in the Figure 39.

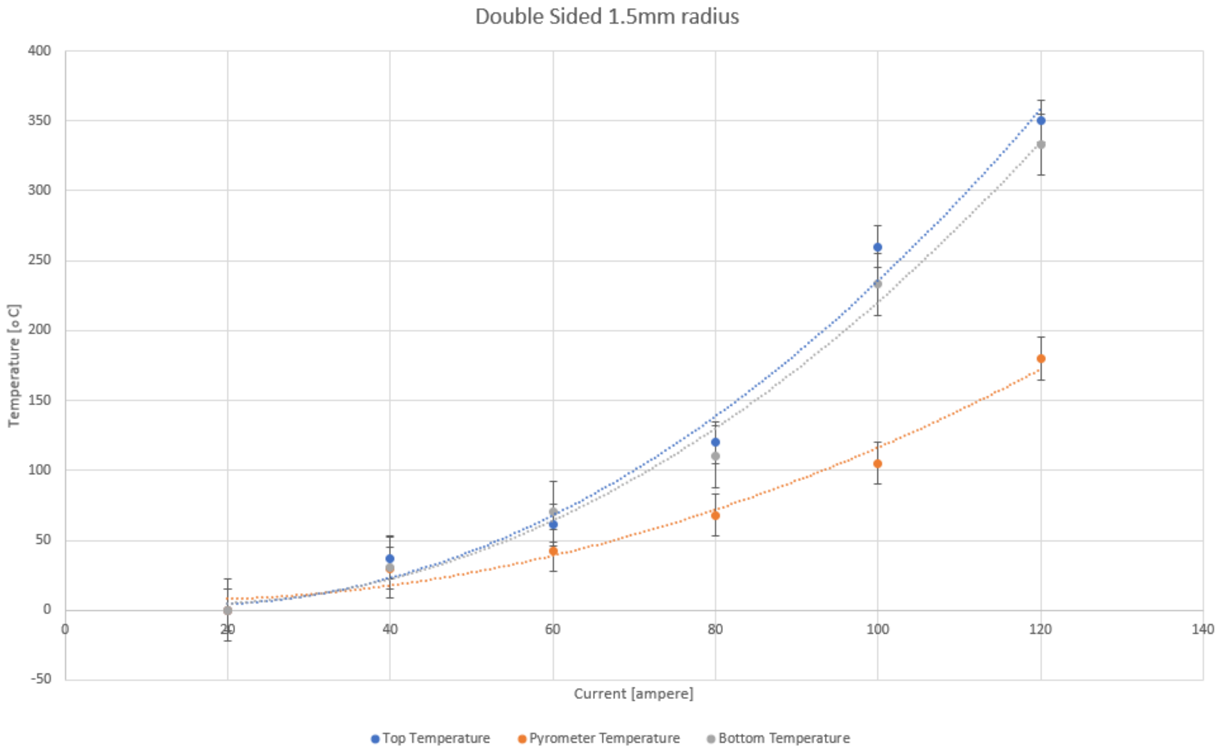

Figure 39: Double-sided 1.5mm radii temperatures.

The difference in the temperatures measured by the 1.5mm pin double sided pin and the pyrometer increases along with growing current - the highest difference was 150°C at 120 A.

The temperature increased consistently at a rate of the square of the current's magnitude, in a quadratic fashion, enabling extrapolation if necessary.

Once the current had reached 140A, the temperature drastically increased to over 850°C. This caused the pin to buckle, requiring the test to be ended to prevent the pyrometer from being overloaded. The temperature measurements of the double-sided 2.5mm radius pins are shown in Figure 40.

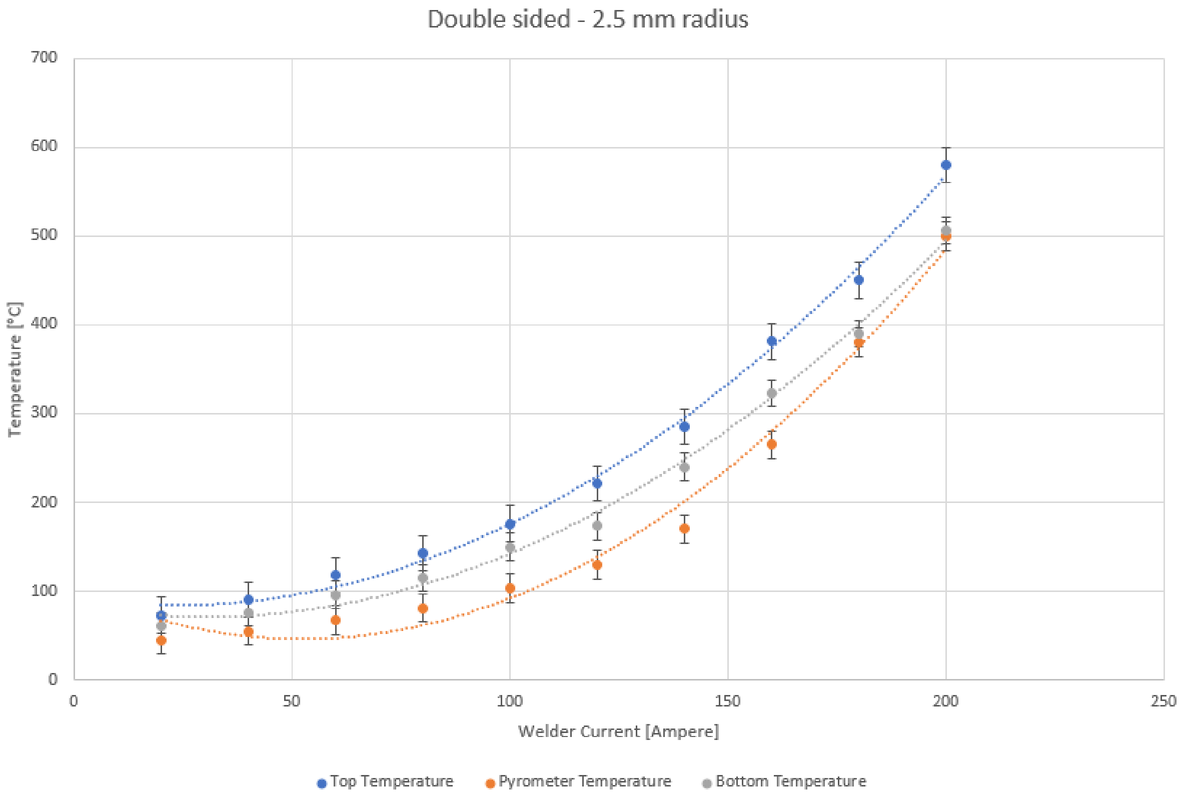

Figure 40: Temperatures for the double-sided 2.5mm radius.

At high currents, the difference between the temperatures at the contact points of the top and bottom 2.5mm pins can be as high as 70°C, which should be taken into account in further COF calculations.

Since the electrical contact resistance of both sides should be equal (normal load and current), this temperature difference could be caused by a drop in voltage between the contact and the power source. In previous experiments in [2] using 1.5mm radius pins it was noticed the presence of a voltage difference in measurements using a multi-tester with ends connected to the sample and the pin. That means that some of the voltage was being consumed by the contacts in the heating process. This could explain the observed difference in temperature between the top contact and the bottom contact, but further investigations are necessary to better understand how to keep the temperature the same in both top and bottom.

As heat transfer was intensified, the temperature difference between the bottom pin and pyrometer measurements becomes lower.

Temperatures of the single-sided 2.5 mm radius pin are reported in Figure 41 below.

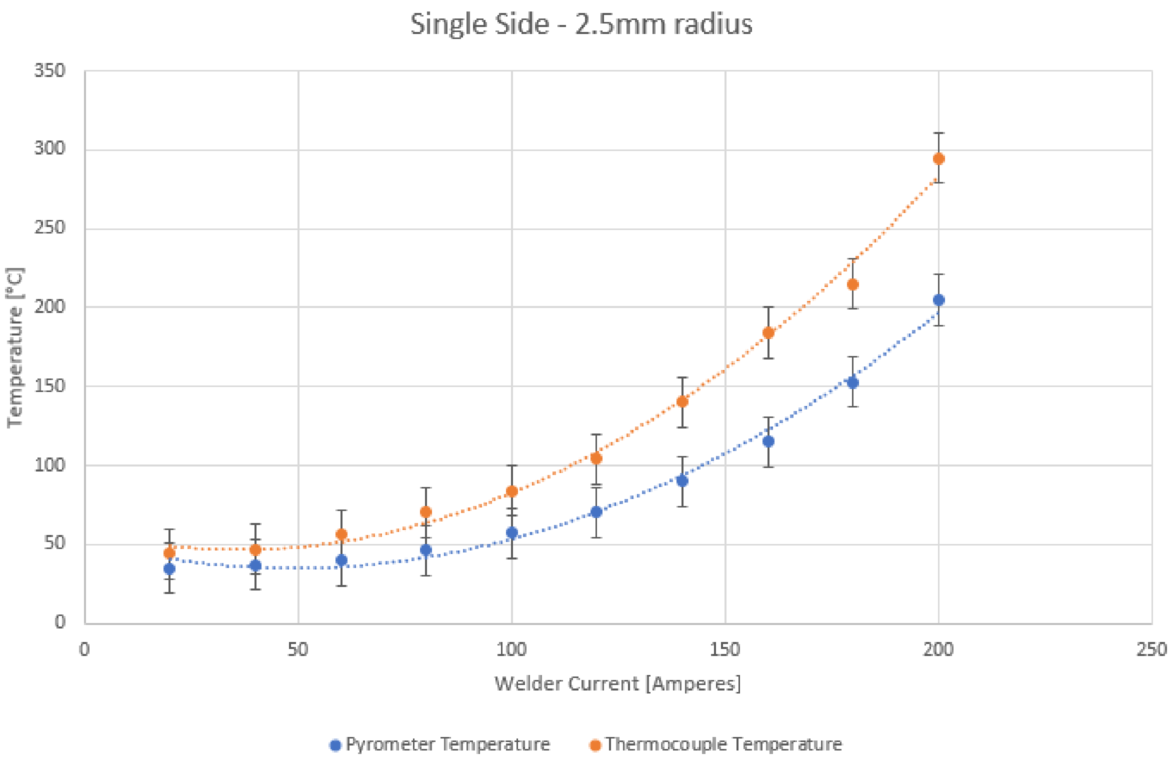

Figure 41: Temperatures of the 2.5 mm single-sided pin.

The difference in measured temperatures between the single sided 2.5mm pin and the pyrometer largely followed the same trend as in the double-sided 2.5mm pin. However, since the welder was limited to 200A, it was unclear if this difference could be reduced at higher temperatures.

Figure 42 provides a comparison between the temperatures of each pin setup, using the average of the temperatures from the bottom and top thermocouples as reference.

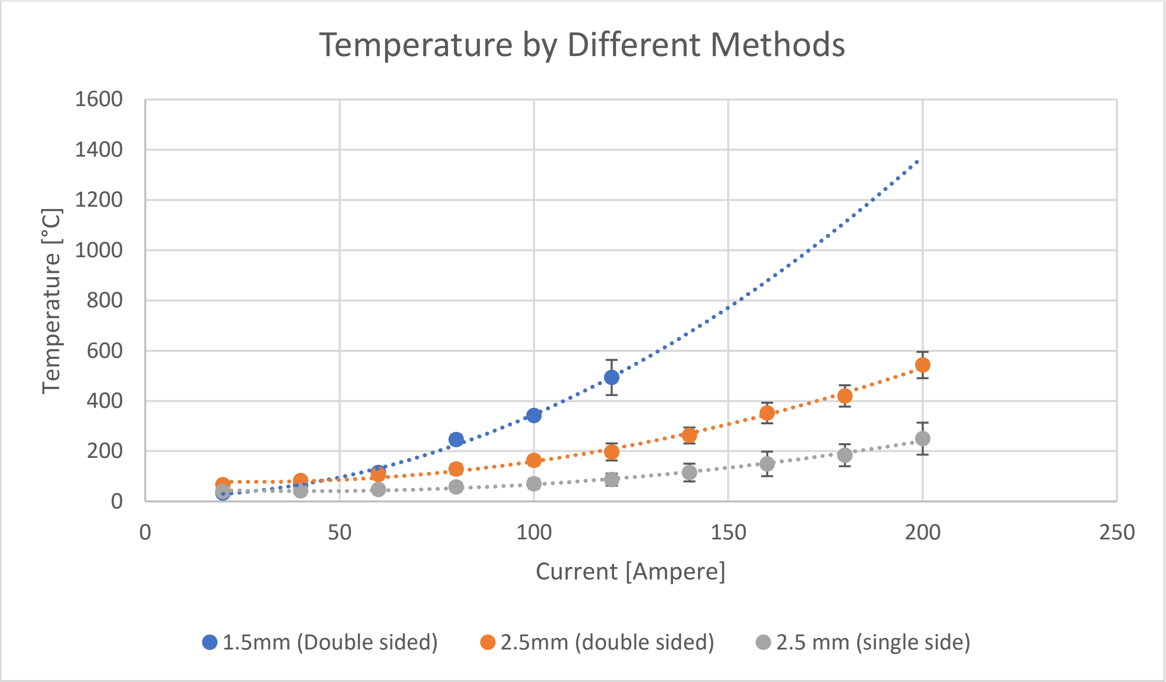

Figure 42: Temperature by different methods.

Some observations can be made from this graph. A smaller pin tip radius generated higher temperatures, as do double-sided pins compared to single sided ones.

The pin radius influenced the measurement of temperature in the contact zone and actually led to a decrease in temperature at the zone of contact.

Heat generation is directly related to electrical contact resistance. According to [33], this property depends on several contact factors, the most important of which are the loads, surface roughness and contact area. The electrons can freely pass if a metal-to-metal bond is made between the contacts.

Interactions at the pin/disk interface produced numerous material junctions. As the load was elevated, these junctions grew in size and number, facilitating electron travel and decreasing electrical resistance, which in turn, reduced the temperature at the contact zone.

A larger pin size radius also increased the number of junctions, which explains why the 2.5mm pin experienced much less heat generation. Figure 43 depicts the differences in size of both imprints at an equal load of 1000N. The area of the 1.5 mm pin imprint is 0.48mm^2 and that of the 2.5mm pin is 0.78mm^2.

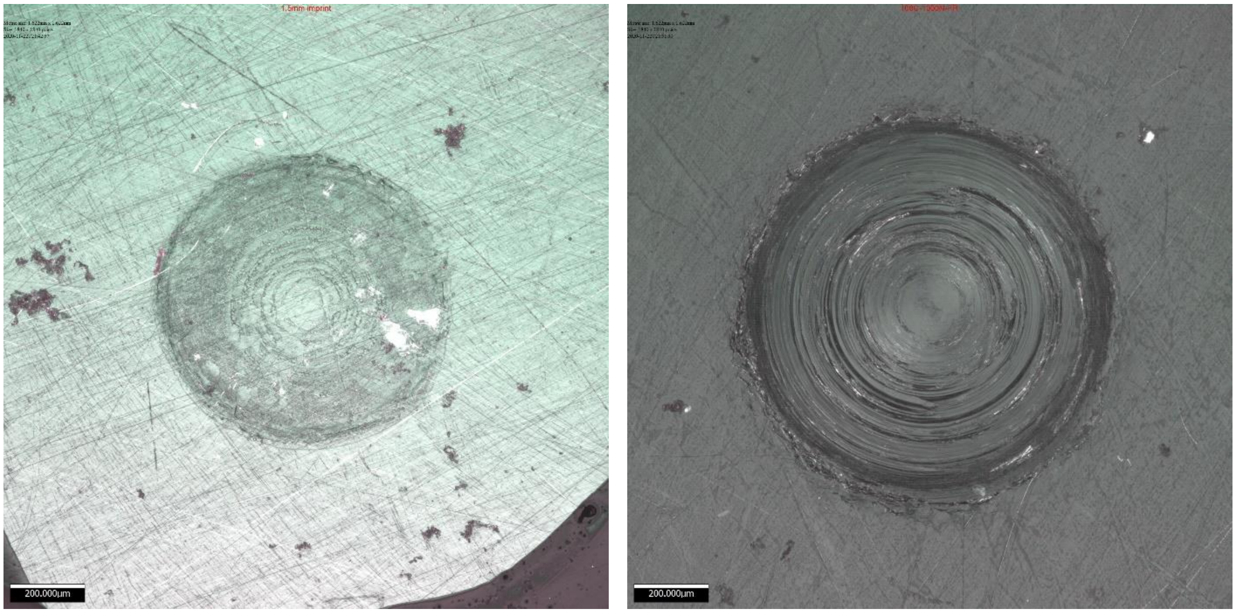

Figure 43: Difference in imprint size for 1000N of normal load. Left) 1.5mm pin radius. Right) 2.5mm pin radius.

Other factors can affect electrical resistance at the contact point as well, such as the oxide layer being sheared off by the pin’s rotation. The degree of pin surface roughness also determines the area of metal contact through which the current can freely pass.

A smoother pin surface was also found to be useful for isolating the measurements of adhesive bond shearing in the tribometer. However, as the disk was rotated, the metallic junctions increased in number, causing a corresponding decrease in the temperature. A source of greater current would then be needed to continue improving the precision of the results using higher quality pins with a greater radius.

5.1.1. Influence of Temperature in the Double-Sided Pin Setup

The contact areas of the double-sided pin are far too small for the heat to be dissipated in the sample. Heat instead accumulates at the middle of the pin, as confirmed in [2]. This effect can be seen in Figure 44 depicting the 1.5 mm pin in which the temperature has surpassed the Draper point (visible radiation above 525°C).

Figure 44: 1.5 mm pin radius glowing.

Additional experiments were performed on the thicker 2.5mm radius pin using the torque pulley system.

A comparison of temperature measurements with and without the pulley are shown in Figure 45 below.

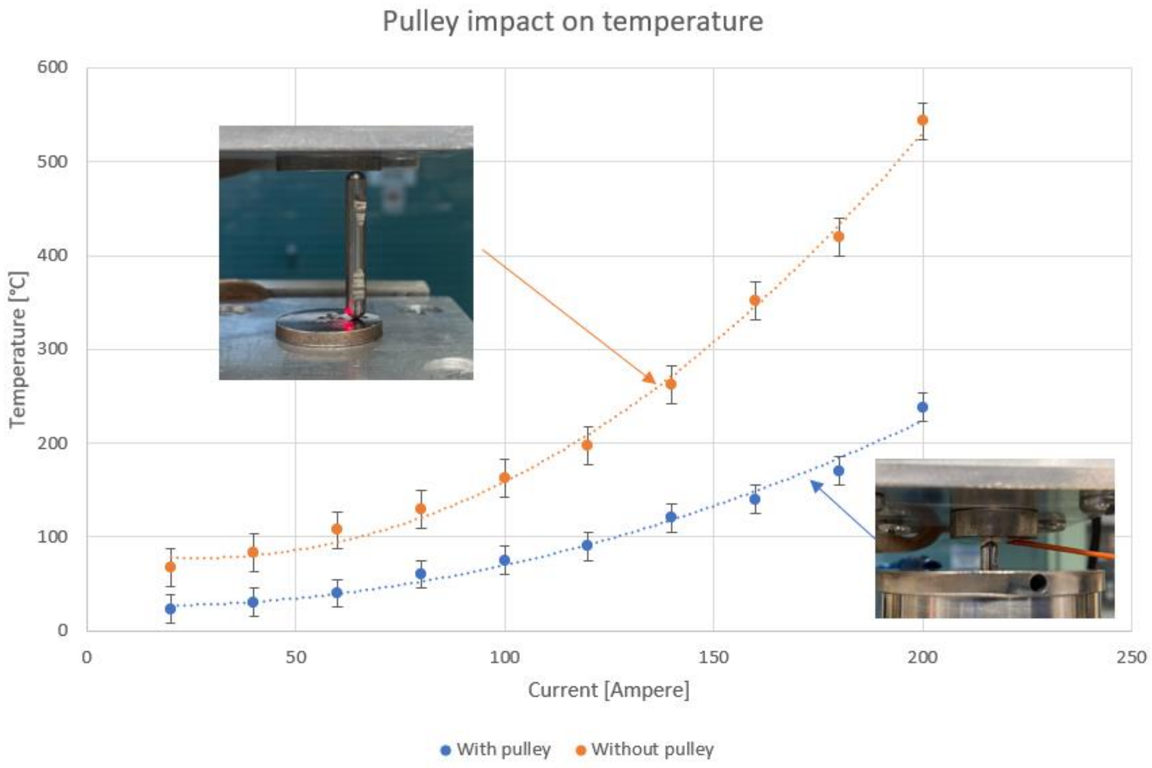

Figure 45: Effect of the pulley on measured temperature.

Temperature increased along with the current in both experiments. The nature of heat transfer in the system accounts for the higher temperature measurements without the pulley. Heat flows from the contact points in two directions. The first is through the sample as well as the electrodes and the second is into the body of the pulley. The mass and shape of the pulley helps dissipate heat into the air, by means of its increased surface area. A diagram of this process is depicted in Figure 46.

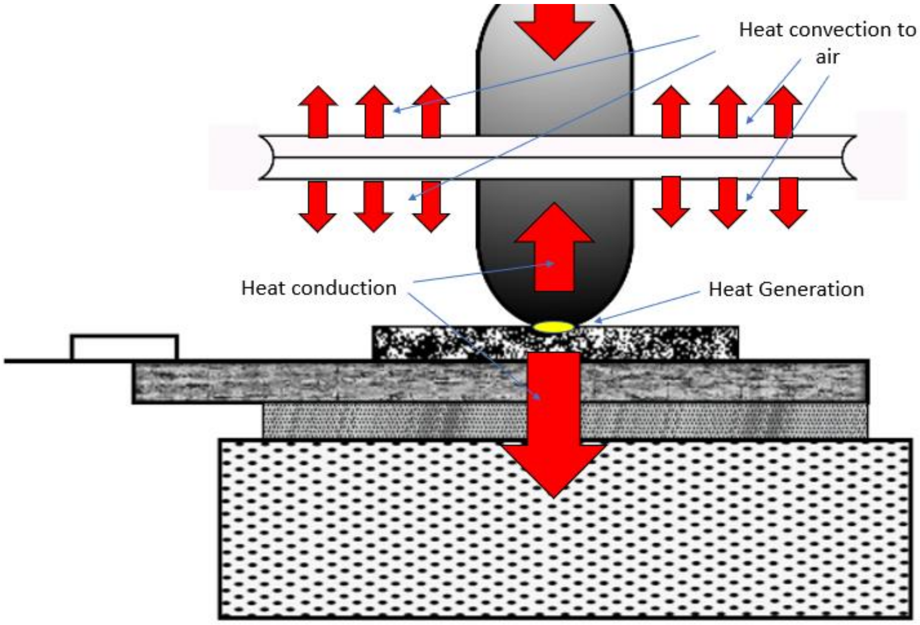

Figure 46: Heat dissipation schematics.

A small portion of the heat generated at the contact points was dissipated into the air. According to the laws of heat transfer, the larger portion of heat will flow through the solid body of the sample before dissipating in the environment. The experiment was run until the temperature reached a steady point and did not increase with time, which confirmed that the surface of the pulley was successfully dissipating the heat.

To avoid this issue and reach temperatures indicative of real machining, a ceramic pulley was machined by MACOR with a thermal conductivity of 1.46 W/m°C. The ceramic pulley design failed during the first set of friction experiments due the pulley's brittleness and susceptibility to thermal stress. The results of this attempt can be seen in Figure 47.

Figure 47: Ceramic pulley attempt.

It is worth mentioning that further improvements of this setup could be achieved if the welder current was increased to a minimum of 300A (extrapolating from the graph in Figure 42) and if the surface between the pin and the pulley could be thermally insulated to concentrate the temperature on the pin.

At this stage obtaining an accurate measurement of the temperature in the contact zone still presented a major challenge. A protrusion formed on the surface of the sample when the heated 2.5mm TiN coated pin in contact with the AISI 1045 disk was placed under a 500N load. Figure 48 indicates that the protrusion has formed due to the plastic deformation of the imprint. It can be assumed that the Draper point (525°C) was reached. The measurements taken by the thermocouple showed a value of 238°C. This does not guarantee that the temperature at the contact point will stay at a high value, since the protrusions have a lower heat dissipation than the rest of the contact area. This demonstrates how a variation in the test input parameters could completely alter the performance of the system.

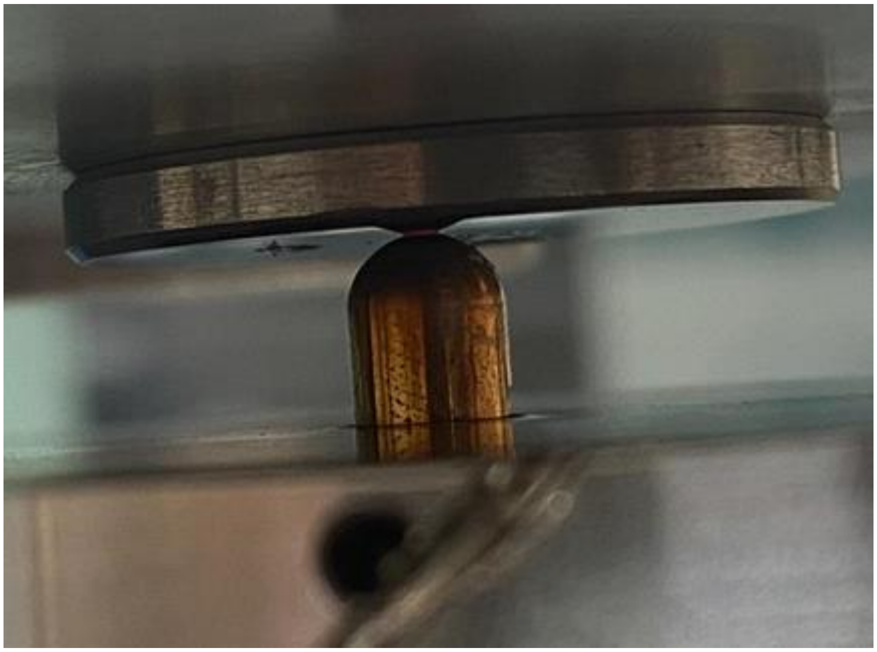

Figure 48: 2.5mm pin at the at the Draper point.

In general, further studies need to be conducted on the temperature measurements in this area. Computer models of the heat distribution for this specific test have been shown to be ineffective due the excessive number of controlled variables. Heat generation seems to be stochastic thus an accurate assessment of the temperature in the contact zone would require empirical methods of measurement.

5.2. INFLUENCE OF PIN ROUGHNESS ON FRICTION

To evaluate the impact of pin roughness on the coefficient of friction, tests were performed on two different sets of WC 6%Co pins in an AISI 1045 sample. The first pin had a radius of 2.5mm and 0.045±0.012 Ra. The second pin had the same radius, but its roughness was much higher, 0.492± 0.13 Ra. Roughness measurements were taken in several directions using an Alicona 3D microscope. The results are depicted in Figure 49 and Figure 50 where the red lines represent the measurement length.

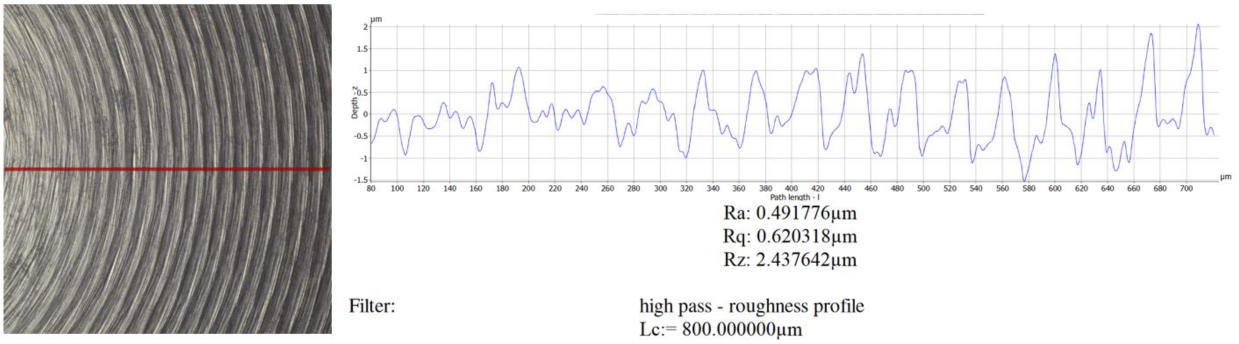

Ra: 0.491776µm
Rq: 0.620318µm
Rz: 2.437642µm

Filter: high pass - roughness profile
Lc:= 800.000000µm

Figure 49: Pin roughness measurement (poor finish).

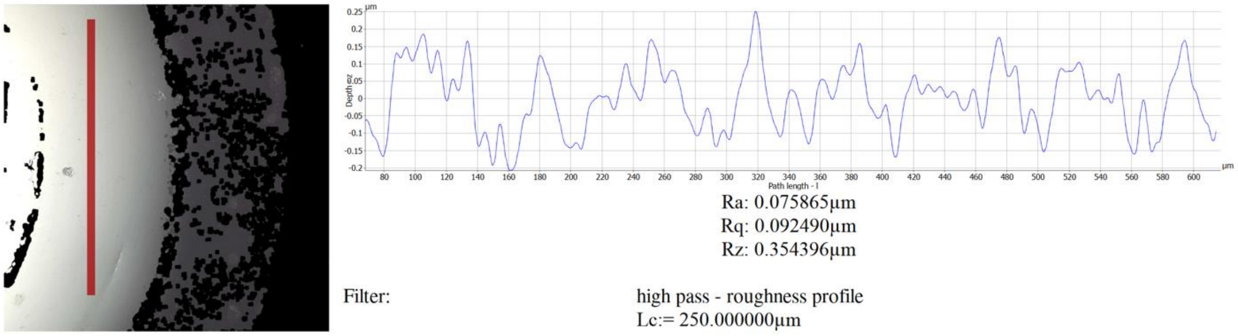

Ra: 0.075865µm
Rq: 0.092490µm
Rz: 0.354396µm

Filter: high pass - roughness profile
Lc:= 250.000000µm

Figure 50: Pin roughness measurement (high quality finish).

Tests were done in increments of 300N from 300 to 2400N (limit of the pressing stage). The imprints were measured by a microscope in two different directions, with the average being taken. The results are presented in Figure 51.

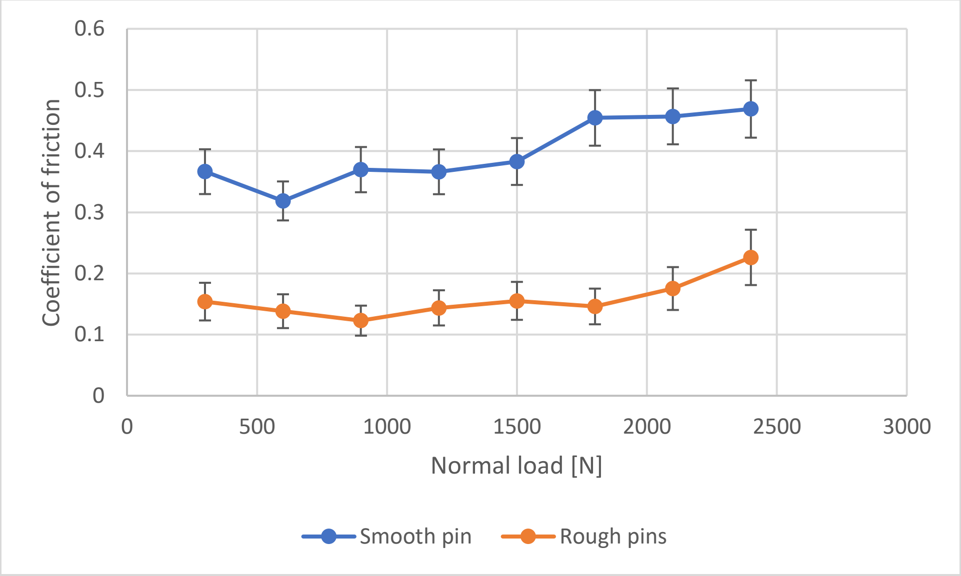

Figure 51: Coefficient of friction for WC uncoated pins in 1045 samples.

The considerable impact of roughness can be seen in these measurements. Variation of the coefficient of friction in the smoother pins is lower. According to [34] the estimated coefficient of friction of AISI 1045 in contact with WC 6% Co, at low temperatures and loads greater than 1800 N, should be between 0.4 and 0.5. This value must represent the minimum load to ensure plastic deformation of the asperities, which is approximately 0.46. The rougher pin featured considerably lower values, which can not be corresponded with any literature data. A deeper analysis of the imprint will be conducted in the next section.

5.2.1. Limitations Related to Pin Roughness

To better understand the effect of pin roughness during the tests, 3D scan images of the resulting imprints were taken by a scanning 3D microscope at a load of 2100N in Figure 52

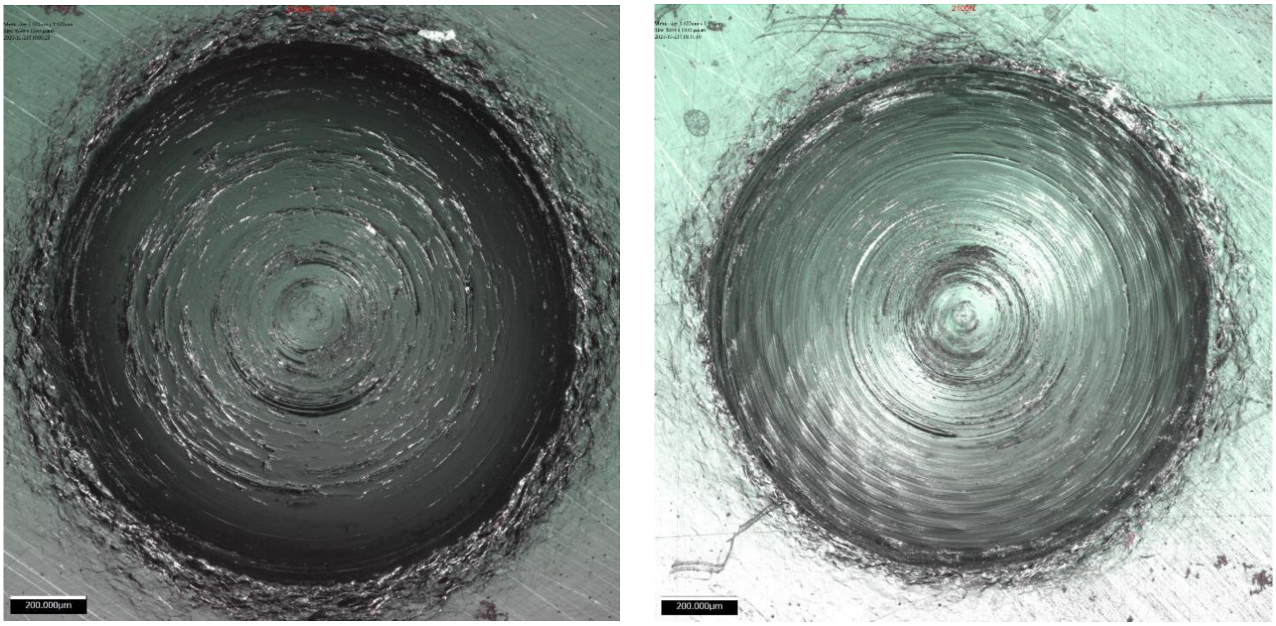

Smooth pin imprint d=1424.5±19 µm

Rough pin imprint d=1344±21 µm

Figure 52: Difference in the diameters of rough and smooth imprints. Left) Imprint using smooth pins. Right) Imprint using rough pins.

The difference in the imprint diameter of the two pins is recorded in the above figure. Since this test is based on a modified Brinnel hardness test, a hardness comparison was made using both diameters and Equation 5-1.

$$HB = 0.102\,\frac{2 \cdot F}{\pi D(D - \sqrt[2]{D^2 - d^2})} \qquad \text{Equation 5-1}$$

Where HB is the hardness value; F is the applied load; D is the diameter of the indenter and d is the imprint diameter.

Using the aforementioned equation for calculating the hardness for each imprint, the hardness value of the smooth pin was measured to be 138.56 HB and the rough pin was 152.39 HB. These values were used to distinguish the imprints under equal loads and the same material.

Based on the previous observation, it can be concluded that the penetration depth of the rough pin was not as high as that of the smooth pin. Figure 53 reports the calculated Brinnel hardness for more imprints and loads. The hardness measurement of the rough pin (Figure 53) features considerable inconsistency. This indicates the difficulty of estimating the normal pressure applied to the pin, which affects the distribution of load throughout the imprint and the resulting coefficient of friction values.

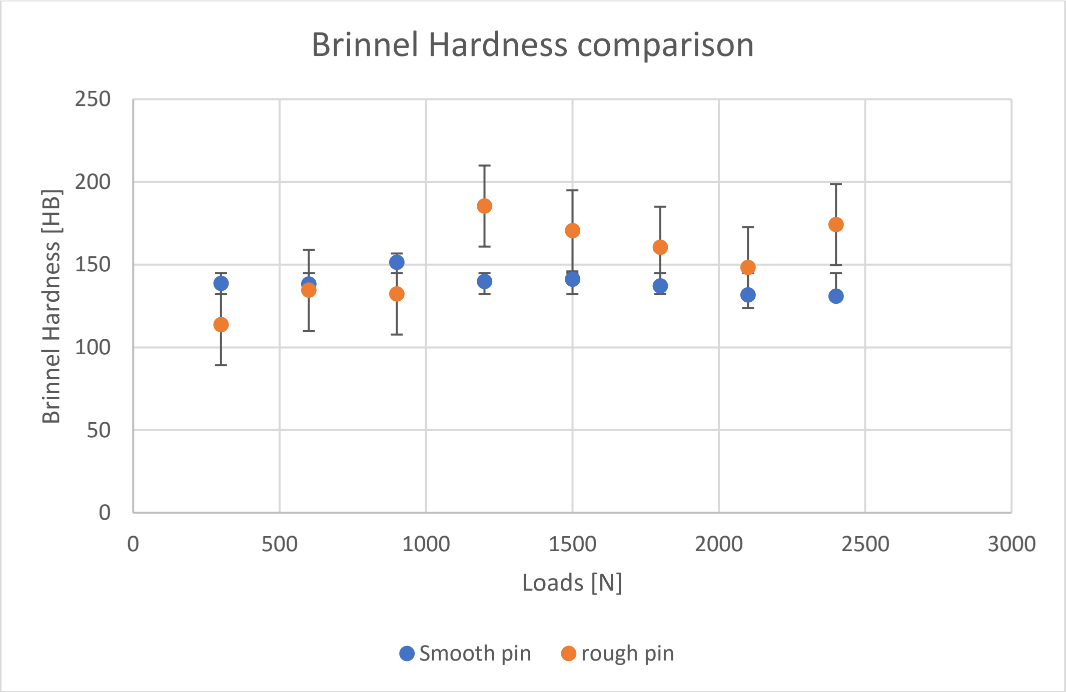

Figure 53: Brinnel hardness comparison.

The influence of roughness on the size of the imprint can be attributed to the interlocking of asperities during the penetration phase of the test.

The difference in the scale of peaks can be seen in the Figure 54. The rough pin imprint has several 3 µm peaks and the average size of the valleys in the smooth imprint was 1.5 µm. This roughness profile does not represent the whole area of the imprint, but rather gives an indication of what occurred in this area.

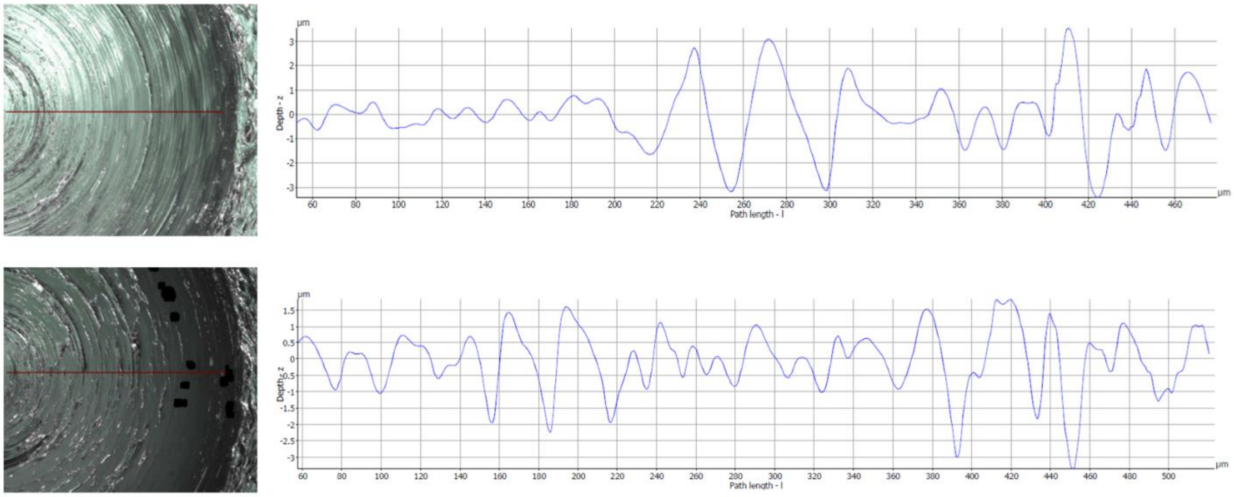

Figure 54: Difference between the roughness of imprints. Top) Using rough pins. Bottom) Using smooth pins.

Pin roughness directly affected the coefficient of friction value. Figure 55 and Figure 56 show the difference in the friction force signals for the smooth and rough pins.

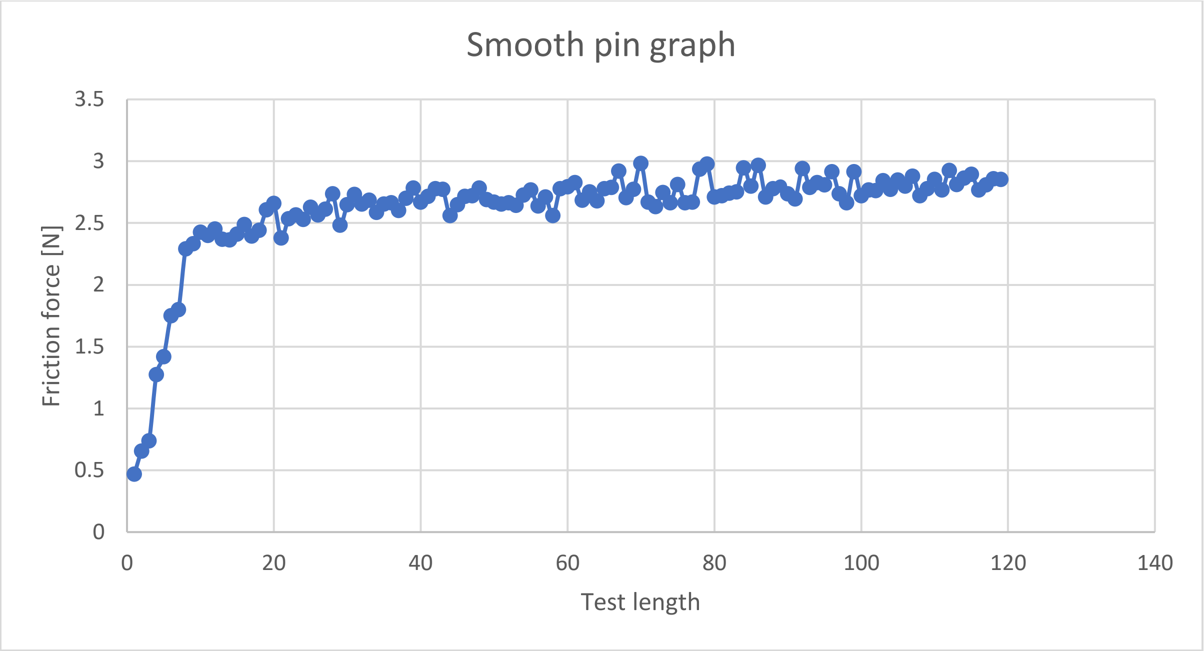

Figure 55: The friction forces of smooth pins.

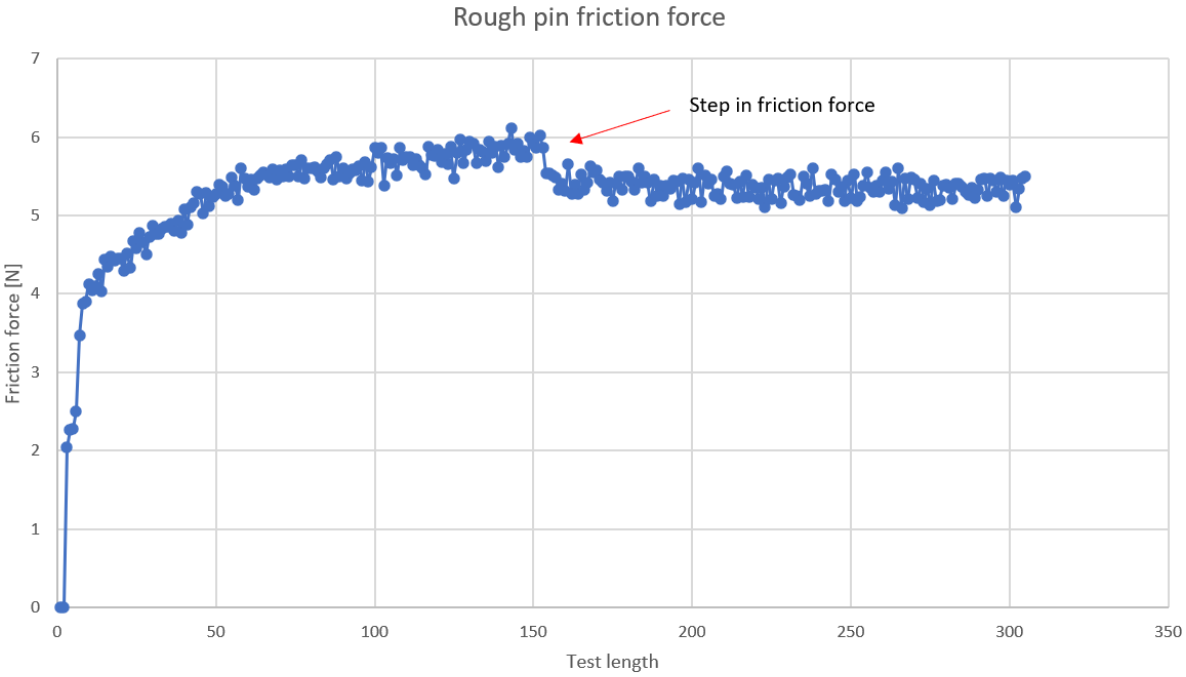

Figure 56: The friction forces of rough pins

The friction force graphs from the load cell illustrate several issues that can crop up during the tests. In Figure 55, the friction force transferred to the steady state at the beginning of the pin's rotation, making it easy to obtain an average value for use in COF calculations. In Figure 56, the graph tends to move towards a steady state before abruptly dropping to a step below in the friction force. This outcome was often observed when rough pins were used, and it may be caused by some sudden change occurring on the contact zone.

Another possible explanation can be found in the imprints' failure conditions. Figure 57 shows a colored height image of an imprint on a Ti64 alloy with a TiAlN coating deposited on the rough pins. It can be seen in this 3D image that a small Ti64 particle of 19 µm height had become dislocated from its place under high pressure and was cold-welded back to the workpiece. This kind of wear was characterized by severe adhesion and aggravated by ploughing.

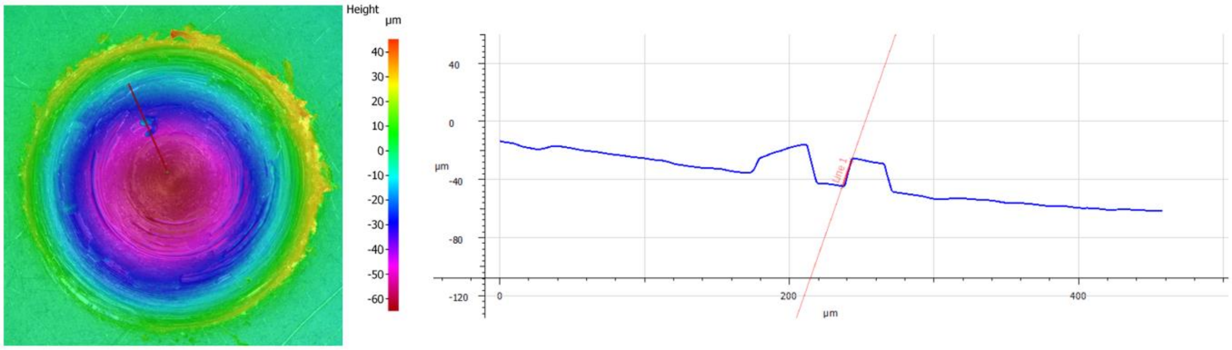

Figure 57: Decentralized rotation due wear on imprint.

The result of this test was also shown in the red area (depth region) of Figure 57. The imprint was found to have shifted from its equilibrium state. Further evidence of this can be found on the microscope pin image in Figure 58. Two Ti64 imprint circles had adhered material on the pin tip and separate particles became detached from the workpiece.

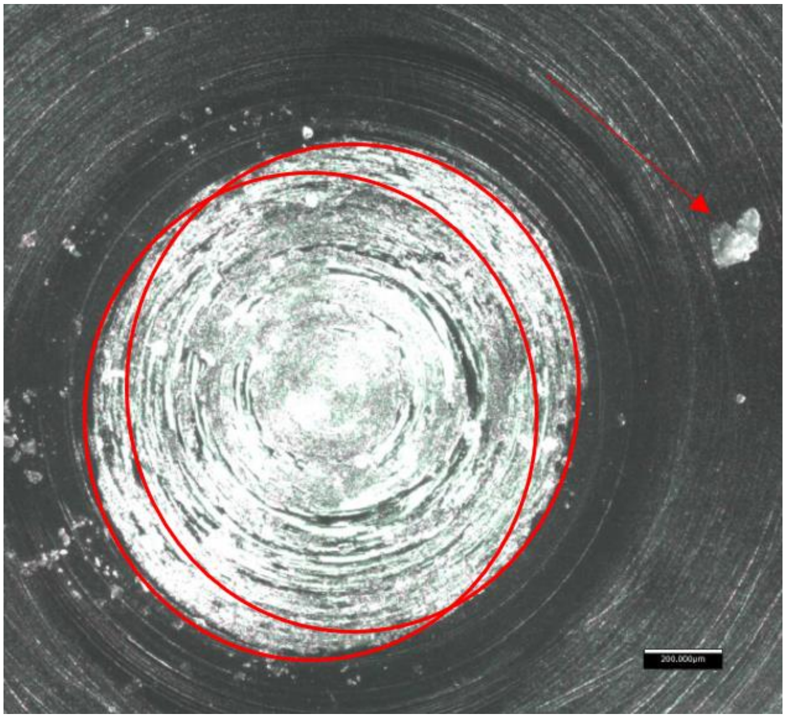

Figure 58: TiAlN coated pin with Ti64 adhered to it.

Other aspects can be noted during COF measurements using rough pins. The next set of Figures 59-62 presents side by side images of imprints created by rough and smooth pins for AISI 1045. It is possible to observe a grooved pattern formed by small planes in all sections of the rough pins, in addition to several concentric rings which indicate the presence of workpiece abrasion in this region.

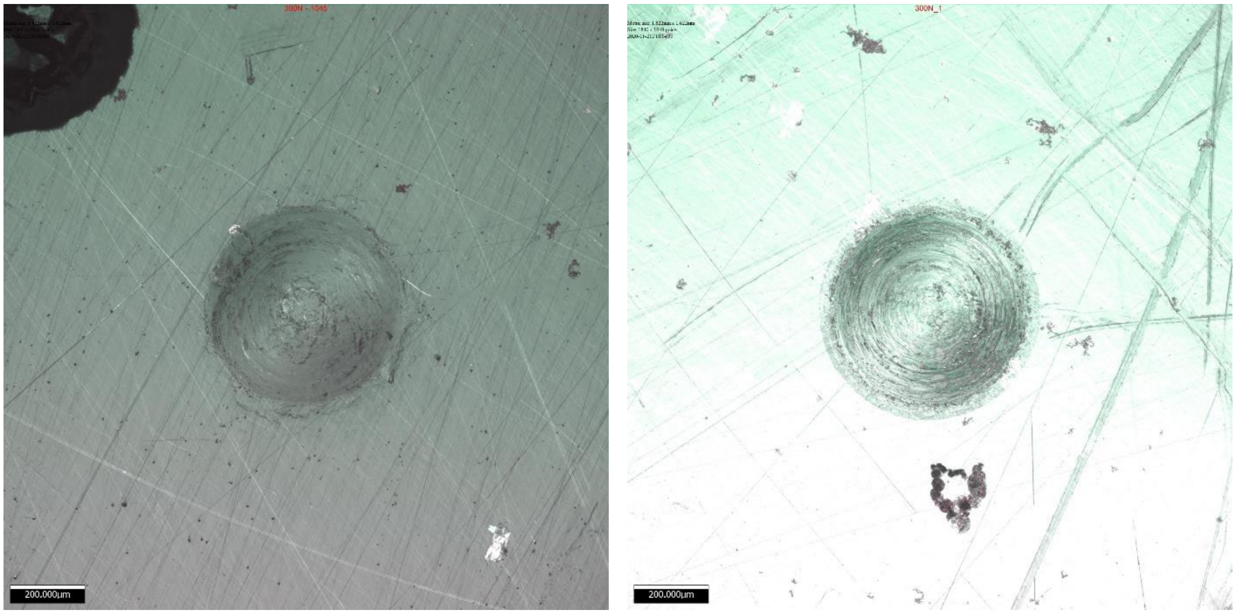

Figure 59: Imprint of AISI 1045 with 300N of normal load. Left) Using smooth pins. Right) Using rough pins.

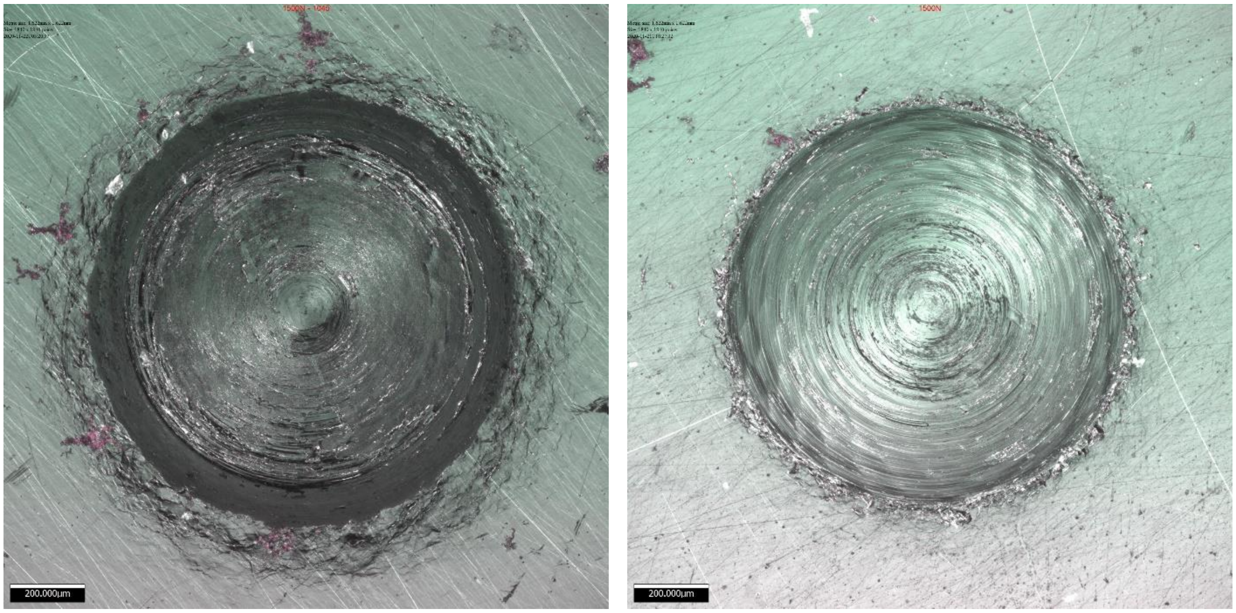

Figure 60: Imprint of AISI 1045 for 1500N of normal load. Left) Using smooth pins. Right) Using rough pins.

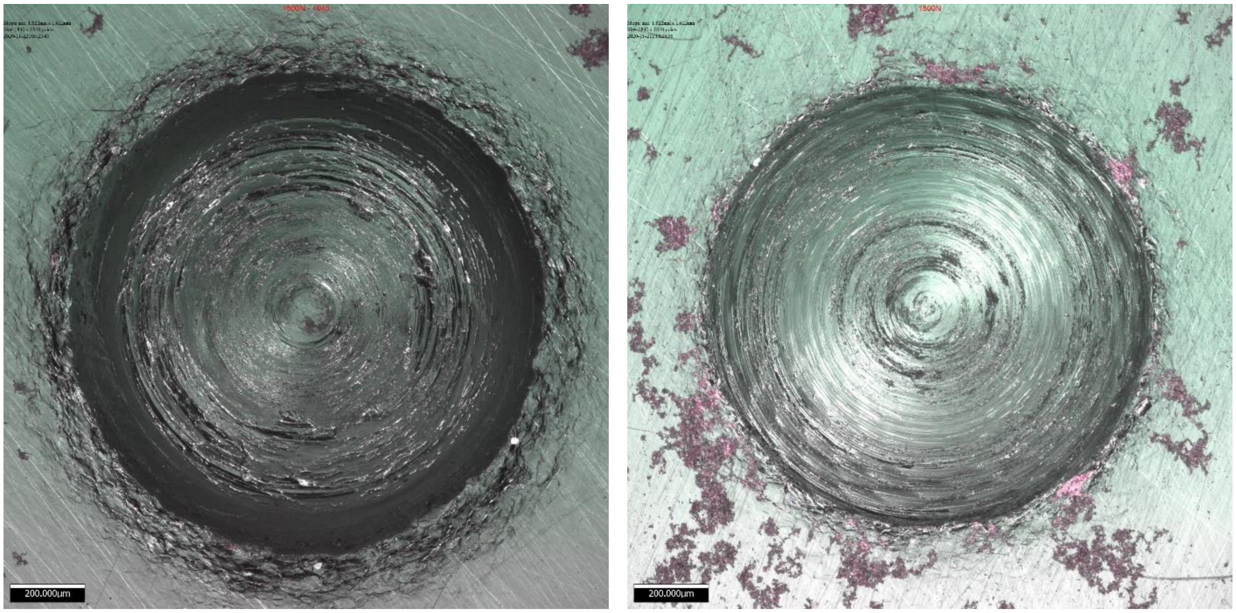

Figure 62: Imprint of AISI 1045 for 1800N of normal load. Left) Using smooth pins. Right) Using rough pins.

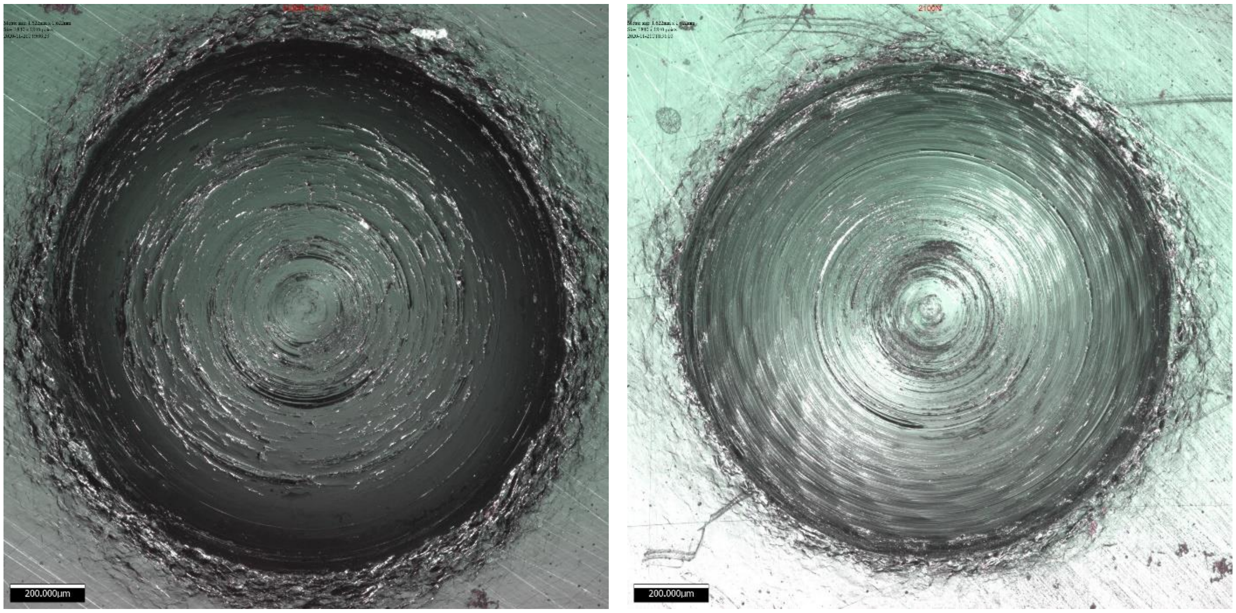

Figure 63: Imprint of AISI 1045 for 2100N of normal load. Left) Using smooth pins. Right) Using rough pins.

The formation of groove plane patterns in the imprints could have also contributed to the low coefficient of friction found during rough pin tests. The grooves act as ramps for the pin to climb over during the course of rotation, decreasing the adhesive force between the surfaces.

The results presented in this section are consistent with the recommendations given by Shuster and Lyapin for the use of pins with surface roughness between 0.06 and 0.16 Ra [15], [16].

5.3. IMPRINT MEASUREMENT ANALYSIS

The coefficient of friction measurements were strongly affected by the measurements made on the imprints. Very similar experiments [14]–[16] measured the imprints in two dimensions. Meanwhile, the latest version of this tribometer used another approach to measure the imprints [1]–[3]. In this case a 3D Alicona microscope was used to demonstrate that the diameter measured without the material pushed to the side of the imprint is more indicative of the actual contact area of the pin and disk than a value representing the peak to peak value. Figure 64 presents a 3D cross-section scan of an imprint.

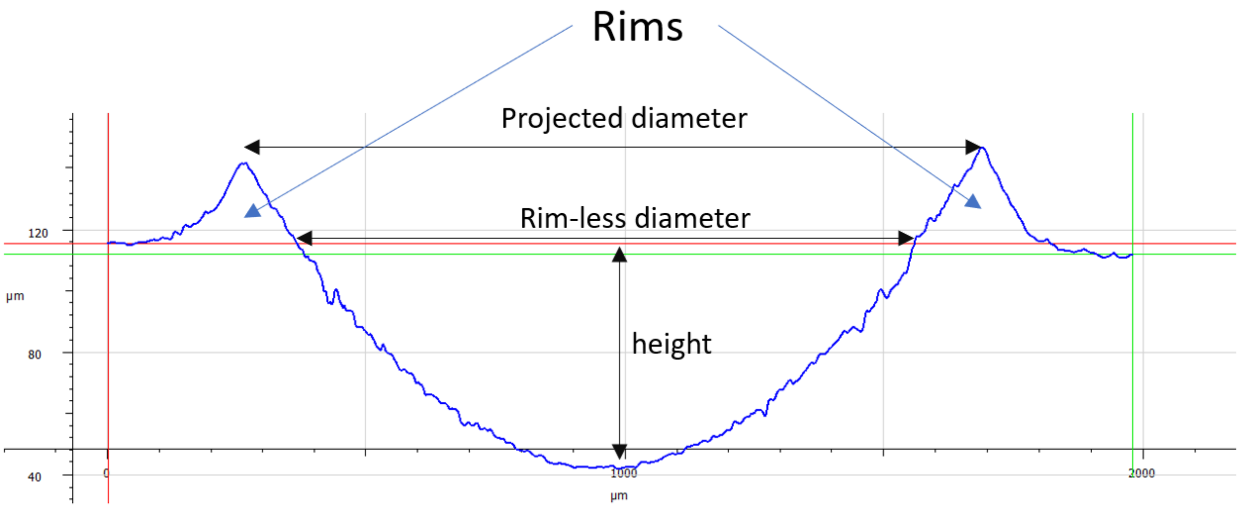

Figure 64: Methods of imprints measuring.

Since this work chiefly investigates the differences between pin radii of 1.5mm and 2.5mm, it is necessary to draw a comparison between the methods of measuring each imprint. One such experimental method is the measurement of the adhesion radius at the tip of the pin in two different directions, as shown in Figure 65.

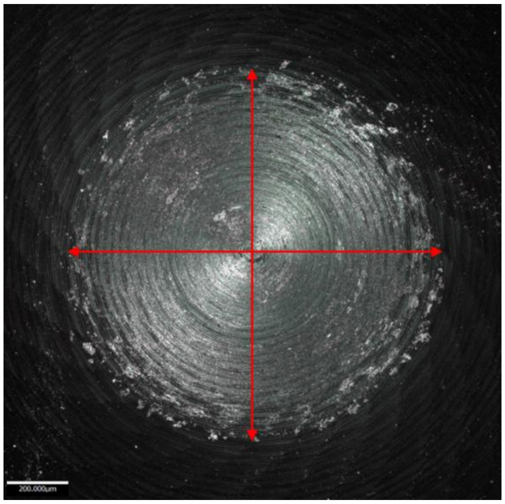

Figure 65: Projected measurement method.

The experimental results are recorded in Figure 66 in increments of 100N from 400 to 2400N using a Ti64sample in contact with a TiAlCrN coated pin.

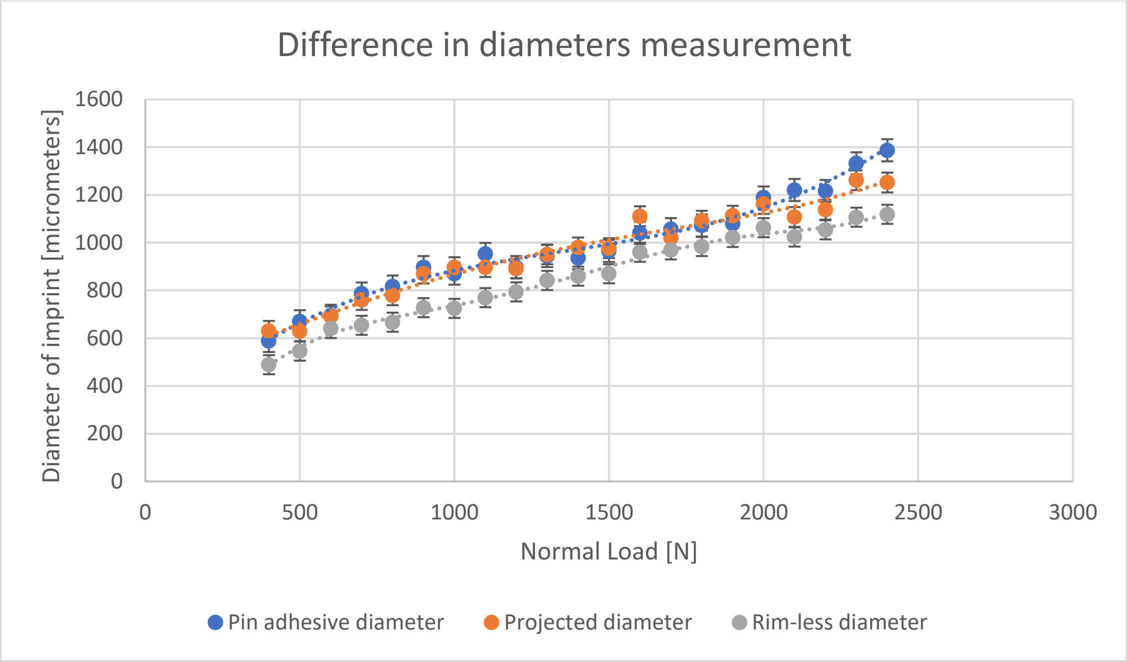

Figure 66: Difference in the measurement methods.

It is possible to see an approximation in the graph between the projected diameter and the pin adhesive diameter at loads lower than 2000N. At loads greater than 2000N, the pin adhesive diameter began to diverge from that of the imprints. This can be attributed to the growth of the imprint's edge rim. The pressure along the edges was not the same as throughout the imprint, which also means that there was less adhesion on the periphery of the imprint.

The influence of diameter measurement on the coefficient of friction is shown in Figure 67.

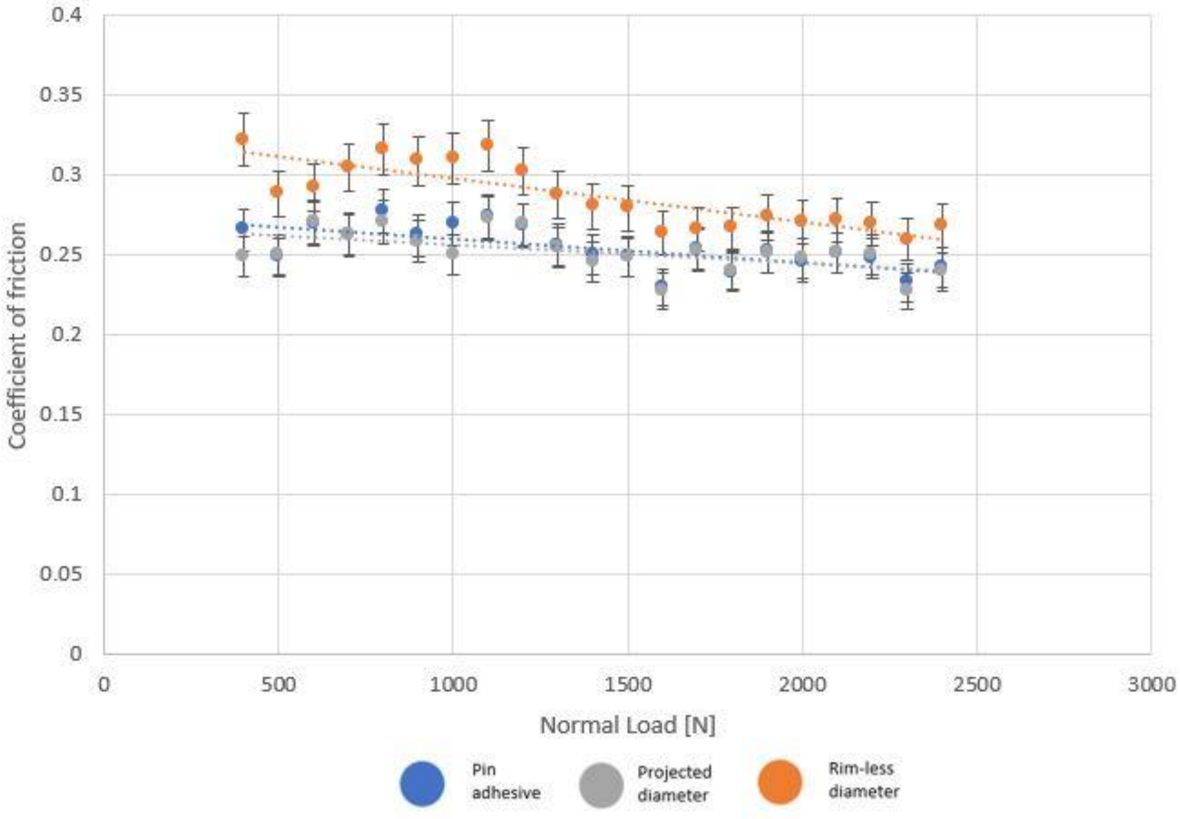

Figure 67: Impact of measurements on coefficient of friction results.

As expected, the results from the rimless method were higher due the smaller size of the imprint. As a consequence, the coefficient of friction was 16% higher at smaller loads and 6% higher at higher loads. The COF results under high loads are given in Table 6

Table 6: Table of coefficient of friction differences.

Method of imprint measurement	Coefficient of friction
Pin adhesion	0.25±0.01
Rim-less	0.29±0.02
Projected	0.25±0.01

The measurements suggest that higher loads tend to improve the quality of the data outputs. Larger imprints and friction forces tend to reduce systematic errors from the equipment, improving the result repeatability.

The results from the pin adhesion method match closely with the projected method and do not significantly interfere with the coefficient of friction calculation. It is worth mentioning that with some material combinations, adhesive traces of the workpiece were not very visible on the images of the pin. The pin adhesion method should be preferably used for material combinations that feature strong adhesion.

Overall, this method was observed to not be particularly reliable. In some cases, parts of the workpiece can become attached to the edge of the imprint and become difficult to distinguish from it.

5.3.1. COEFFICIENT OF FRICTION AND SEIZURE IN SEVERAL MATERIALS

In this section, additional coefficient of friction tests on different tribo-systems were performed using 2.5mm radius double-sided coated pins with a roughness of 0.19 Ra. The test sets are described below:

- Uncoated Tungsten Carbide pins with a 6% Cobalt binder in contact with a Ti-6Al-4V sample.
- TiAlN coated Tungsten Carbide pins with a 6% Cobalt binder in contact with a Ti-6Al-4V sample.
- TiAlCrN coated Tungsten Carbide pins with a 6% Cobalt binder in contact with a Ti-6Al-4V sample.

This selection of materials was chosen based on its widespread use in industry. The significance of these experiments relates to how equipment changes can affect the coefficient of friction measurements.

These studies were performed at room temperature, due to the previously encountered difficulties with achieving high temperatures using 2.5mm radius pins. Figure 68, Figure 69 and Figure 70, depict the normal and shear stresses of each load in relation to the coefficient of friction. The normal loads were raised in increments of 100N from 400 to 2400N.

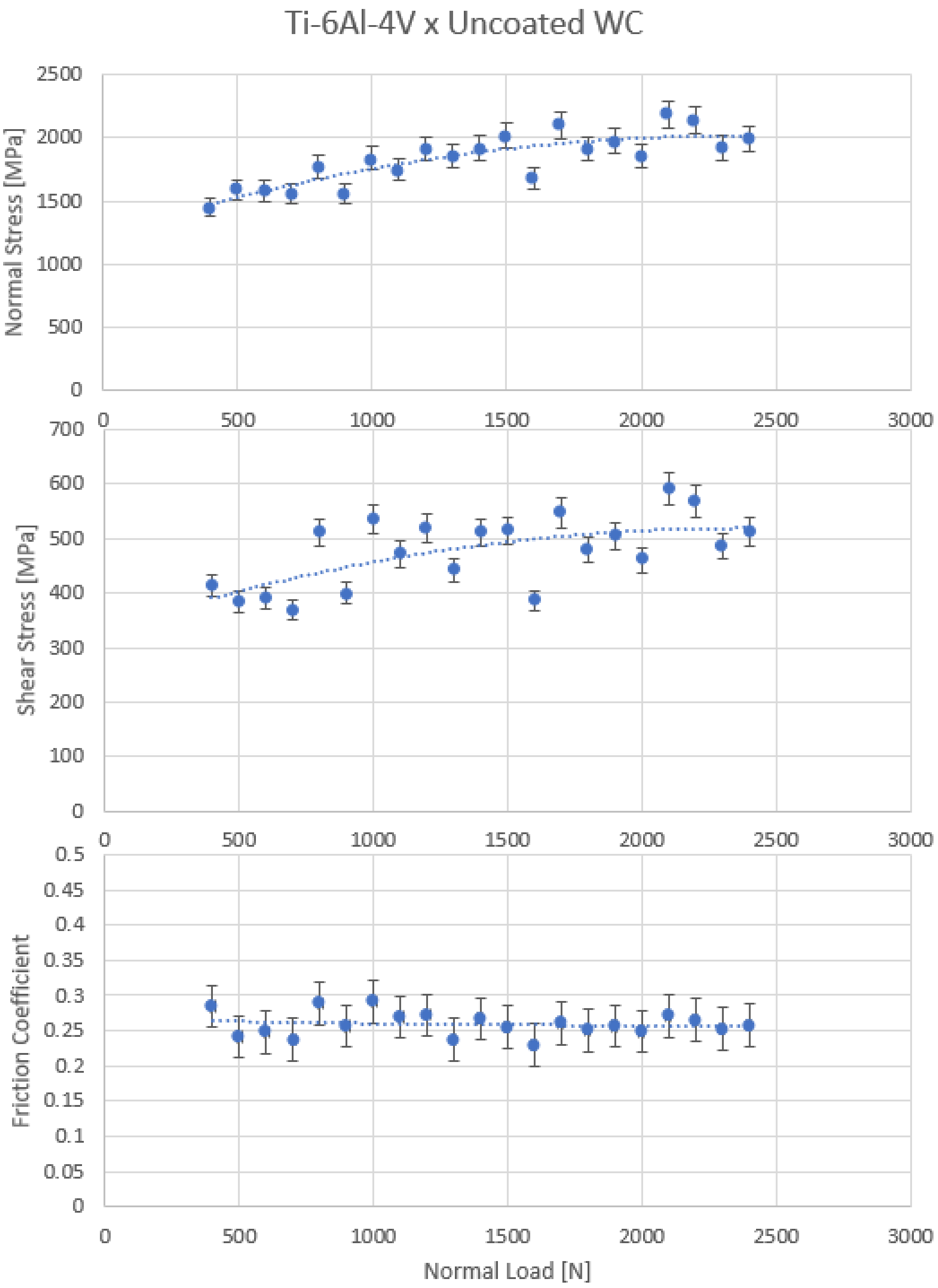

Figure 68: Coefficient of friction and stresses of uncoated WC pins in contact with Ti64.

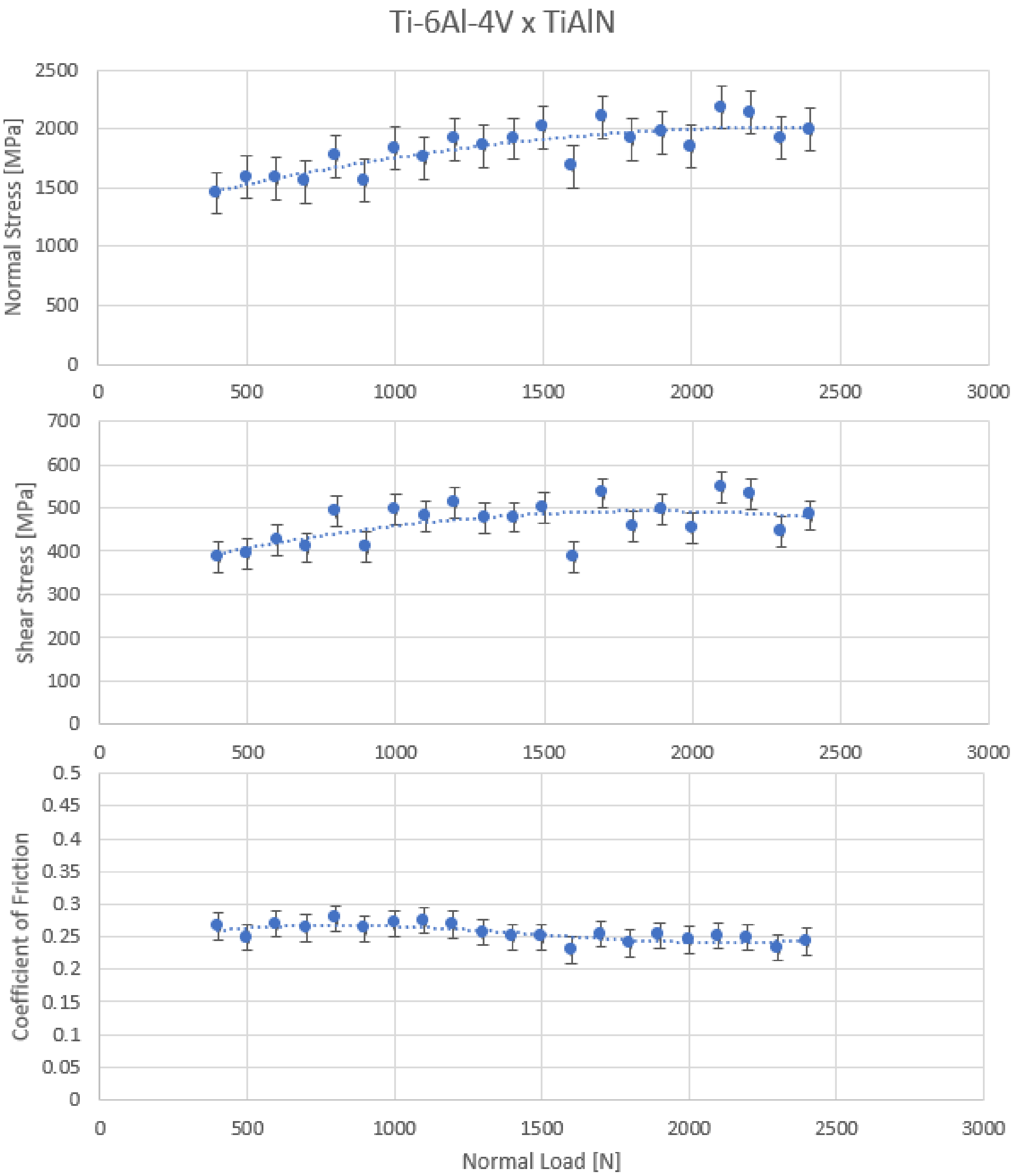

Figure 69: Coefficient of friction and stresses in the Ti64 sample in contact with a TiAlN coated pins.

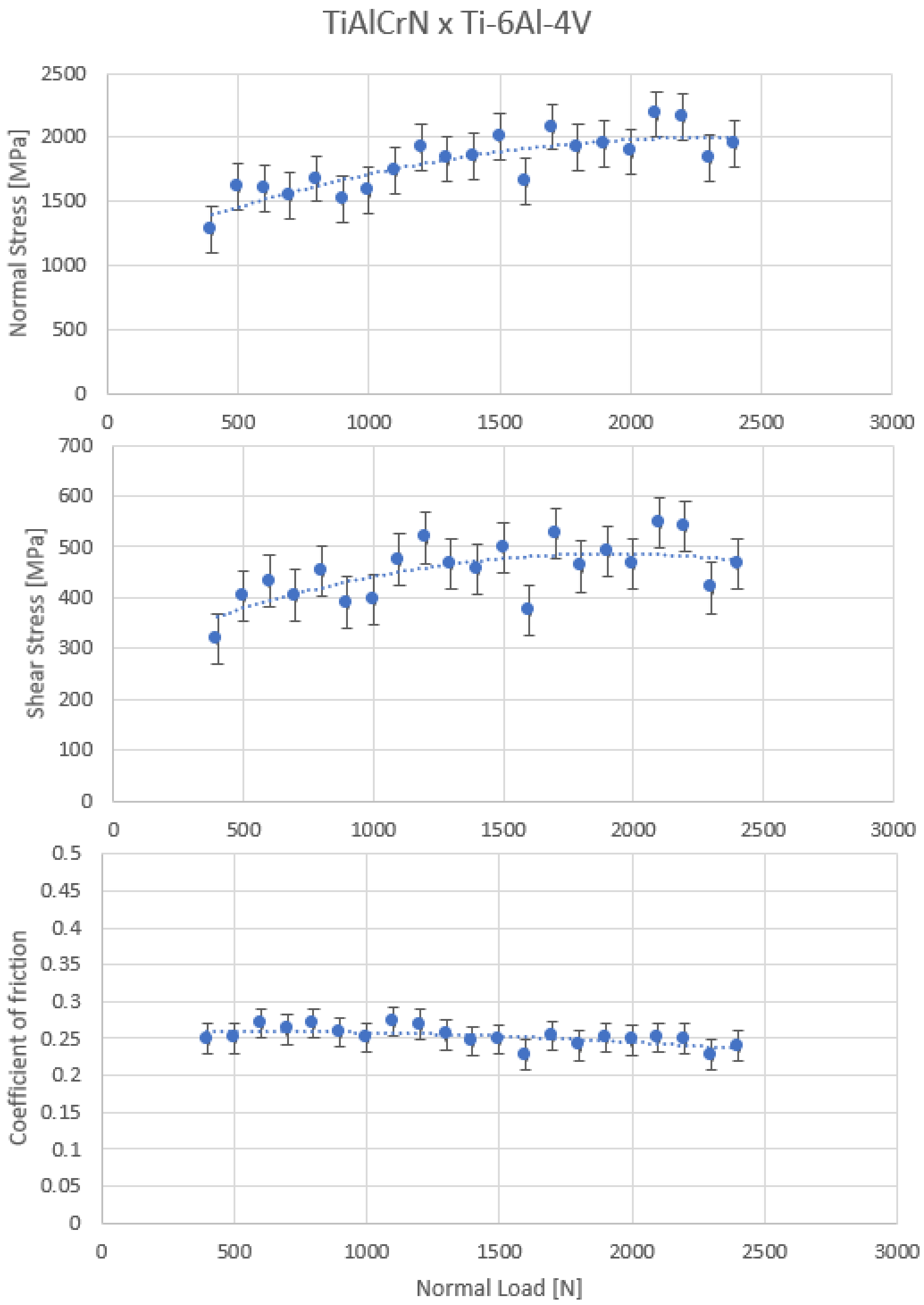

Figure 70: Coefficient of friction and stresses in the Ti64 sample in contact with a TiAlCrN coated pin.

It is possible to notice a trend in all the graphs depicted in Figure 68, Figure 69 and Figure 70. As the normal loads were gradually increased, the coefficient of friction remained constant. The coatings did not perform much better than the uncoated pin, most likely due to the absence of their lubricious properties at this temperature range.[5]. Table 7 reports the results of the above coefficient of friction test.

Table 7: Coefficient of friction for several coatings in Ti-6Al-4V.

Pin surface	Coefficient of friction
Uncoated WC6%Co	0.26±0.02
TiAlN	0.25±0.01
TiAlCrN	0.25±0.01

The obtained values are within the range of previously reported data [1]. The referenced work used a single sided pin method and the same tribometer to test a set of TiAlN coated pins in contact with a Ti-6Al-4V disk. The results presented in Figure 71 show that at room temperature, the difference from the benchmark was found to be only 8%, (0.22 to 0.25). This stands in contrast with the results obtained from the old setup which featured an error of 26% (0.22 to 0.3).

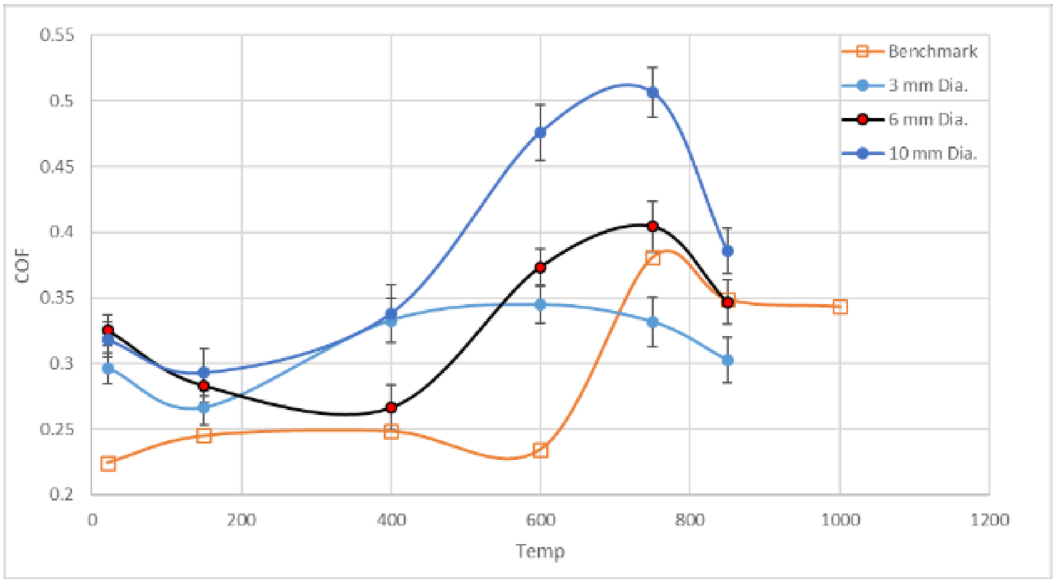

Figure 71: Results of the single-sided approach for different radii [1].

The coefficient of friction trend in the Ti-6Al-4V graph (Figure 71) clearly demonstrates that it is difficult to achieve high pressures in 5mm pins given the range of available loads for this equipment. A higher load would be needed to achieve the range of normal pressures typical of real machining (as stated in the first chapter). Estimation of the normal load seems to agree with the range of loads needed for the Brinnel hardness tests associated with each size of indenter specified in E10 [35].

These coefficient of friction results confirmed the limitations of the test performed under loads greater than 400N. The deviations recorded during the initial stages of the experiment present a good trend for further testing. Under a realistic range of pressures, higher coefficient of friction values were expected, similar to the ones recorded during the AISI 1045 Steel test displayed in Figure 72.

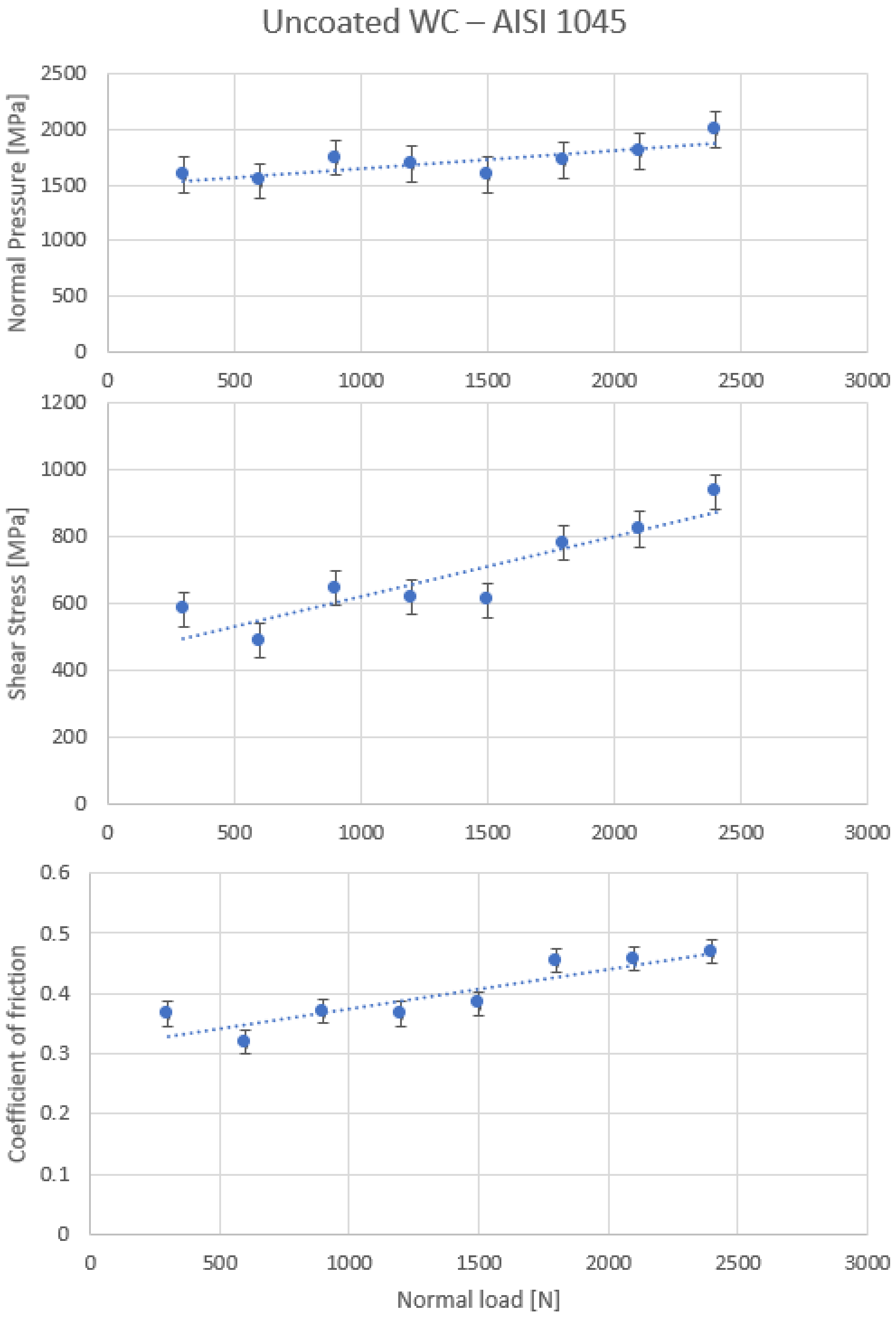

Figure 72: Coefficient of friction for uncoated WC pins in contact with AISI 1045

In contrast with Ti-6Al-4V, the graphs of AISI 1045 indicate a different outcome. The increase of normal pressures is not significant compared with the increase of the loads, although the shear stresses continue to grow. The ratio between their coefficients of friction constantly increases in the graph, indicating the desired region of loads at a range of up to 1800N. Seizure of the material commences once this load is surpassed, indicating high surface adhesion.

This can also be explained in terms of the seizure ratio described in [5], [7], [15]. This ratio delineates the coefficient of friction by analyzing the dimensions of the imprint and the value of coefficient of friction in Equation 2-7.Once the coefficient of friction passes this threshold, shearing of the bulk material begins to occur.

$$\gamma = \frac{h}{r} + \frac{\tau}{\sigma} < 0.5$$

A graph of the AISI 1045 imprint ratios in relation to the applied loads is presented in Figure 73

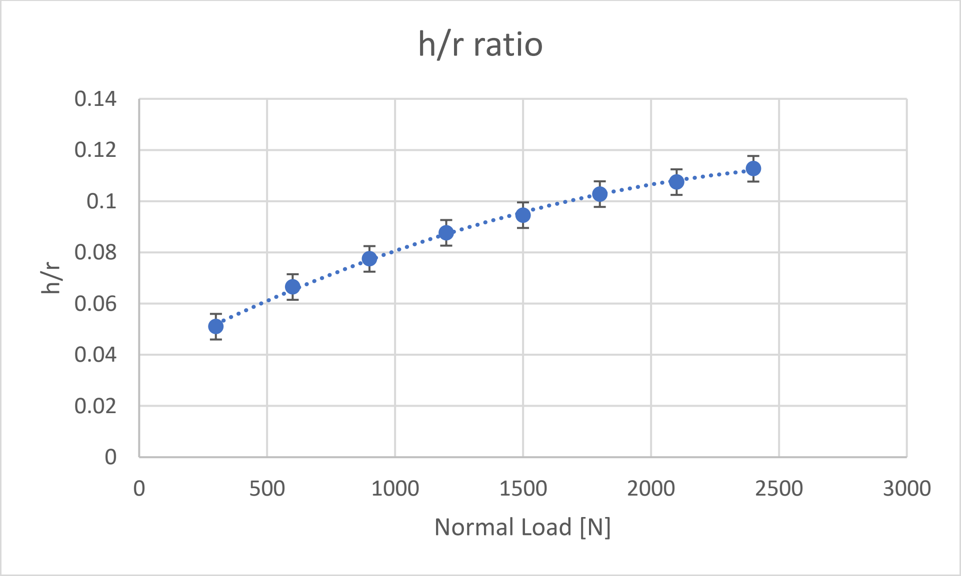

Figure 73: h/r ratios in relation to the load.

The above graph accords with literature data stating that the imprint ratio is between 0.03 and 0.15 in most materials [5]. In Figure 74, the values of γ represent the applied normal load. The red line threshold indicates that after 1500N, the material begins to undergo seizure and the coefficient of friction becomes a representation of the shearing of the sample's subsurface layers.

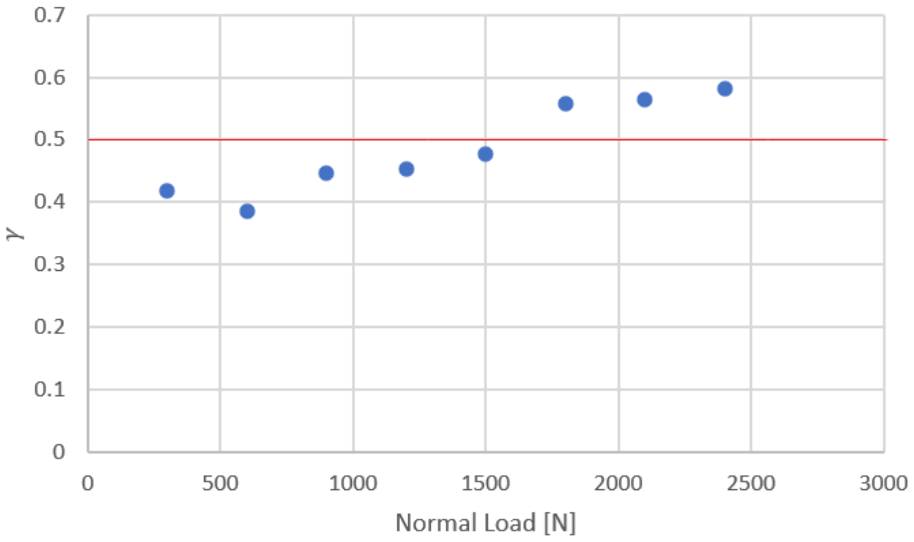

Figure 74: Values of γ vs. the normal load.

These values confirm that adhesive formation and breakage of asperities occurs at a load of 1500N when using 5mm pins on AISI 1045. This can also be observed in the imprint images,

.

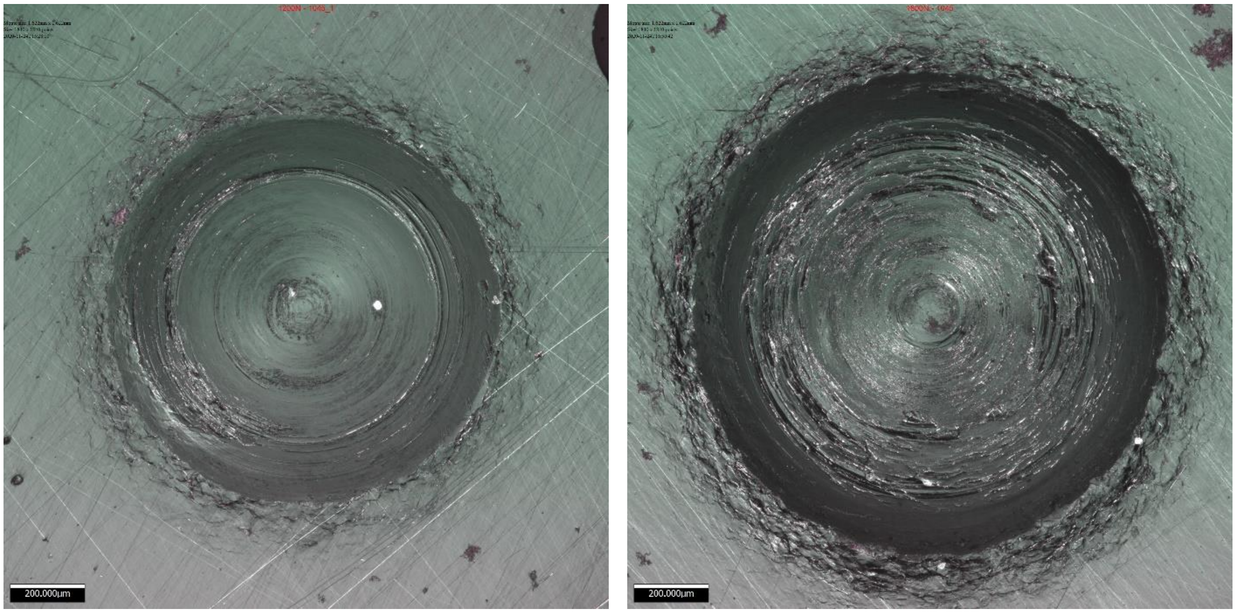

Figure 75: Image of the imprints. Left) Using 1200N Right) Using 1800N

The 1200N load imprint (Figure 76 Left) exhibits a smooth surface with low wear tracks, indicating that only a part of the material had adhered to the surface of the pin. This signifies the slip-and-stick phenomenon commonly found at the contact between the chip and tool on the rake face. Conversely, (Figure 76 Right) clearly shows adhered material being sheared and sticking to other zones of the imprint with excessive signs of wear.

In summary, it is very important to observe the load conditions before conducting the temperature test, to ensure that the right amount of load is provided to the system without inducing seizure.

CHAPTER 6. CONCLUSIONS AND RECOMMENDATIONS FOR FUTURE WORK

This work investigated the implementation of a double-sided pin temperature measuring method to the MMRI High-Load High-Temperature tribometer. A new stage and control mechanism for measuring friction forces was developed and implemented on the tribometer system, demonstrating considerable result repeatability of approximately 8% under several different loads.

Coefficient of friction data for Ti64 and AISI 1045 Steel was gathered at room temperature. Better test results could be achieved if limitations inherent to the equipment, such as calibration of the sensors and normal stress graphs were overcome. One of the major contributions of this work is the selection of an appropriate load for the tribometer system.

The imprint measurement method was evaluated in terms of its influence on the coefficient of friction calculations. A new method for measuring the contact area without the sample’s imprints was introduced, which demonstrated good agreement with the projected imprint measurements of the microscope.

Applying the concepts discussed in this study, the time needed for equipment calibration and pin alignment during each test was reduced from 20 to 4 minutes.

Modification of the setup was investigated as the diameter of the pin was varied from 3mm to 5 mm. An increase in the pin size affected the pressures measured by the equipment. In softer materials such as AISI 1045 seizure conditions could be avoided by using 5mm pins at an appropriate range of loads. However, in harder materials like Ti-6Al-4V, the equipment’s load limitation does not allow the use of a heavily loaded slider. Temperature at the contact zone was found to be significantly affected by the pin size. Pyrometer measurement proved to be an unreliable method for obtaining precise temperature data, especially with the increase of pin radius size.

Another factor limiting the maximum temperature achievable is the conductivity of the component materials, such as mandrels and pulleys to which the pin was attached. These components dissipated heat from the pins reducing the temperature in the contact zones, making it difficult to obtain a high temperature. The double-sided pin approach also revealed a difference in the temperatures present at both contact points. Further study of this difference is recommended since this interference could be caused by various influences coming from other parts of the equipment rather than the voltage drop for each contact point of the system.

Recommendations for further studies in this topic include:

- Adaptation of the pulley for 3mm diameter double-sided pins. This could improve the alignment and ease of use of this method and also provide higher stresses and temperatures.
- Improvement of the heating setup. Installing a cooler plate at the base of the electrodes could provide a valuable boundary condition for the estimation of temperature at the contact point.
- Organizing a table of different pin sizes for each material similar to the Brinnel hardness test. Although high pressures could be achieved at the lower range of loads on 3mm pins, the amount of equipment errors arising at low loads could negatively affect the pressure readings. Development of an in-house method for polishing the tips of the pins. Since pins with a polished surface are ten times as costly as unpolished ones, it would be desirable to develop a method of polishing them without ruining their sphericity.

- Development of a reliable method of experimentally measuring the temperature in the contact zone.
- Performing additional studies of the changes in temperature at the pin rotational stage.
- Improving the pressing stage to handle higher loads to better emulate the extreme pressures experienced when machining high-strength materials such as Inconel.

REFERENCES

[1] A. A. Khoei, "A Method for Assessing the Tribological Performance of Tool and Workpiece Interactions," (M.A.Sc. Thesis) McMaster University, Hamilton, ON, Canada, 2019.

[2] J. Boyd, "Tribometer-Based Quantifying of Friction in Metal Cutting," (M.A.Sc. Thesis) McMaster University, Hamilton, ON, Canada, 2012.

[3] A. Biksa, "Tribological Characterization of Surface Engineered Tooling for Metal Cutting Applications," (M.A.Sc. Thesis) McMaster University, Hamilton, ON, Canada, 2010.

[4] M. Mihranov and L. Shuster, "Tribotechnical Properties of Materials and Wear-Resistant Coatings with Ultra Shall-Grinned Structure," vol. 1. pp. 6–9, 2008.

[5] G. S. Fox-Rabinovich and G. E. Totten, *Self-Organization During Friction : Advanced Surface-Engineered Materials and Systems Design*, vol. 53, no. 9. 2013.

[6] V. I. Semenov, R. Rajendran, S. V Chertovskikh, and V. G. Shibakov, "Comparative Evaluation of the Tribological Properties of Low and Medium Carbon Steels After Heat Treatment and Severe Plastic Deformation," vol. 45, pp. 28–35, 2016.

[7] I. V. Krageski, M. N. Dobychin, and V. S. Kombalov, *Friction and Wear: Calculation Methods*. Pergamon Press, 1982.

[8] E. Popova and V. L. Popov, "The Research Works of Coulomb and Amontons and Generalized Laws of Friction," *Friction*, vol. 3, no. 2, pp. 183–190, 2015, doi: 10.1007/s40544-015-0074-6.

[9] F. P. Bowden and D. Tabor, "Mechanism of Metallic Friction," in *Nature*, 1942, doi:

10.1038/150197a0.

[10] E. Rabinowicz, *Friction and Wear of Materials*. Wiley, 1995.

[11] M. C. Shaw, *Metal Cutting Principles*, 2nd Edition., June. New York: Oxford University Press, Inc., 2005.

[12] F. P. Bowden, D. Tabor, and F. Palmer, “The Friction and Lubrication of Solids,” *Am. J. Phys.*, 1951, doi: 10.1119/1.1933017.

[13] F. P. Bowden and D. Tabor, “Mechanism of Metallic Friction,” in *Nature*, 1942, vol. 150, no. 3798, pp. 197–199, doi: 10.1038/150197a0.

[14] M. C. Shaw, A. Ber, and P. A. Mamin, “Friction Characteristics of Sliding Surfaces Undergoing Subsurface Plastic Flow,” *J. Basic Eng.*, vol. 82, no. 2, p. 342, 1960, doi: 10.1115/1.3662595.

[15] L. Shuster, *Adhesive Interaction in Metal Solids*. Moscow Printer House, 1999.

[16] N. M. Mikhin and K. S. Lyapin, “Influence of a Perpendicular Load and the Diameter of the Indentor on the Tangential Strength of the Adhesive Bond,” *Sov. Mater. Sci.*, vol. 7, no. 1, pp. 34–38, 1973, doi: 10.1007/BF00723009.

[17] J. A. Bailey, “Friction in Metal Machining-Mechanical Aspects,” *Wear*, vol. 31, no. 2, pp. 243–275, 1975, doi: 10.1016/0043-1648(75)90161-1.

[18] N. N. Zorev, *Metal Cutting Mechanics*. Pergamon Press, 1996.

[19] D. A. Stephenson and J. S. Agapiou, *Metal Cutting Theory and Practice, Third Edition*. 2016.

[20] J. Halling, *Principles of Tribology*. Macmillan, 1975.

[21] P. Kapsa and J. M. Martin, "Boundary Lubricant Films: A Review," *Tribol. Int.*, vol. 15, no. 1, pp. 37–42, 1982, doi: 10.1016/0301-679X(82)90110-4.

[22] A. O. Tay, "A Review of Methods of Calculating Machining Temperature," *J. Mater. Process. Tech.*, vol. 36, no. 3, pp. 225–257, 1993, doi: 10.1016/0924-0136(93)90033-3.

[23] A. O. Tay, M. G. Stevenson, and G. de Vahl Davis, "Using the Finite Element Method to Determine Temperature Distributions in Orthogonal Machining," *Inst Mech Eng Proc*, 1974, doi: 10.1243/pime_proc_1974_188_074_02.

[24] J. C. Garcia-Gonzalez, W. Moscoso-Kingsley, and V. Madhavan, "Tool Rake Face Temperature Distribution When Machining Ti6Al4V and Inconel 718," *Procedia Manuf.*, vol. 5, pp. 1369–1381, 2016, doi: 10.1016/j.promfg.2016.08.107.

[25] K. Iwata, J. Aihara, and K. Kurasaka, "The Adhesion of Carbide and Carbon Steels at High Pressures and Temperatures," *Wear*, 1971, doi: 10.1016/0043-1648(71)90163-3.

[26] E. M. Trent and P. K. Wright, *Metal Cutting*. Butterworth-Heinemann, 2000.

[27] P. Hedenqvist and M. Olsson, "Sliding Wear Testing of Coated Cutting Tool Materials," *Tribol. Int.*, 1991, doi: 10.1016/0301-679X(91)90020-A.

[28] W. Grzesik, Z. Zalisz, and P. Nieslony, "Friction and Wear Testing of Multilayer Coatings on Carbide Substrates for Dry Machining Applications," *Surf. Coatings Technol.*, 2002, doi: 10.1016/S0257-8972(02)00040-3.

[29] F. Zemzemi, W. Bensalem, J. Rech, A. Dogui, and P. Kapsa, "New Tribometer Designed for the Characterisation of the Friction Properties at the Tool/Chip/Workpiece Interfaces in

Machining," *Tribo Test*, 2008, doi: 10.1002/tt.50.

[30] M. Olsson, S. Söderberg, S. Jacobson, and S. Hogmark, "Simulation of Cutting Tool Wear by a Modified Pin-on-disc Test," *Int. J. Mach. Tools Manuf.*, 1989, doi: 10.1016/0890-6955(89)90007-2.

[31] H. Puls, F. Klocke, and D. Lung, "Experimental Investigation on Friction Under Metal Cutting Conditions," *Wear*, vol. 310, no. 1–2, pp. 63–71, 2014, doi: 10.1016/j.wear.2013.12.020.

[32] C. Weißenfels and P. Wriggers, "Numerical Modeling of Electrical Contacts," *Comput. Mech.*, vol. 46, no. 2, pp. 301–314, 2010, doi: 10.1007/s00466-009-0454-8.

[33] C. Zhai, D. Hanaor, G. Proust, L. Brassart, Y. Gan, "Interfacial Electro-Mechanical Behaviour at Rough Surfaces,", Elsevier, 2019.

[34] Kagnaya, Boher, Lambert, Lazard, and Cutard, "Friction at High Sliding Speed of WC-6Co Pin Versus Steel Disc AISI 1045: Estimation of the Contact Temperature," *Int. J. Multiphys.*, 2009, doi: 10.1260/175095409788837793.

[35] *ASTM E10-15: Standard Test Method for Brinell Hardness of Metallic Materials*. June. 2012.